

**Equatorwards-breaking
Rossby waves in the North
Atlantic storm track:
Forecast quality, predictability
and dynamics**

by

Lars Wiegand

Submitted in accordance with the requirements for the
degree of Doctor of Philosophy

University of Leeds

School of Earth and Environment

Institute for Climate and Atmospheric Science

July 2011

Declaration of Authorship

The candidate confirms that the work submitted is his own, except where work which has formed part of jointly-authored publications has been included. The contribution of the candidate and the other authors to this work has been explicitly indicated overleaf. The candidate confirms that appropriate credit has been given within the thesis where reference has been made to the work of others.

This copy has been supplied on the understanding that it is copyright material and that no quotation from the thesis may be published without proper acknowledgement.

The publication Wiegand et al. (2011), *Heavy precipitation at the Alpine south side and Saharan dust over central Europe: A predictability study using TIGGE*, Weather and Forecasting (**in press**), presented in the thesis was jointly-authored with Arwen Twitchett, Cornelia Schwierz and Peter Knippertz. This work forms the majority of Chapter 8. The text of the publication was written mainly by the candidate. The analysis of the data sets was also performed by the candidate, with guidance from the coauthors. The coauthors Twitchett and Schwierz contributed to the feature-based error and precipitation analysis sections. Peter Knippertz provided suggestions and advice during both the data analysis and writing stage of the publication.

Where data from or work by people other than the candidate are used in other chapters of the thesis, credit has been given in the Acknowledgements.

“The most reliable way to separate TV channels is still the weather forecast.”

Woody Allen

Acknowledgements

First and foremost, I would like to thank my supervisor, Peter Knippertz for the significant amount of time and effort he has put into supporting me throughout this project. Furthermore, I very enjoyed the experience of going abroad, which would have been possible only because of his move to Leeds. During the last years Peter became a friend and I have appreciated the scientific discussions on that friendly basis.

Thanks also goes to my research support group, Doug Parker and Steven Mobbs. I am grateful to Arwen Twitchett, Cornelia Schwierz and Peter Knippertz for their effort, suggestions and contributions to our cooperative paper published in *Weather and Forecasting*.

Funding for this research came from the 'Deutsche Forschungsgemeinschaft' (DFG, German Science Foundation) and I am grateful to them for making this project possible. In particular, I appreciated their willingness to fund the project in Mainz (GER) as well as in Leeds (UK) after my move to the University of Leeds.

I would like to thank the German Weather Service (DWD) and the UK Met Office (UKMO) for providing access to the ECMWF database. Furthermore I express my thanks to centres contributing to TIGGE for providing the forecast and analysis data. I would also like to acknowledge the E-OBS dataset from the EU-FP6 project ENSEMBLES (<http://ensembles-eu.metofce.com>) and the data providers in the ECA&D project (<http://eca.knmi.nl>).

I need to mention the IT support, namely Stephan Pfahl, Björn Brötz, Gregor Gläser and Richard Rigby at both institutes (IPA Mainz, ICAS Leeds) and thank them for their intriguing support. With their work and the IT structures they set up, the analyses I have undertaken became achievable.

Thanks also goes to the people, whom I was fortunate to share an office with in the last two years. The friendly and very social atmosphere at both institutes I have worked were very beneficial. Most of the people I got to know became friends. Their support was amazing and always welcome.

Many thanks for proof-reading, which increased the quality of the thesis, goes to Anja Schmidt, Ann-Kristin Köhler, Bastiaan Brak, Bradley Jemmett-Smith, Eimear Dunne, Kay Barbara, Luis Garcia-Carreras, Matthew Woodhouse and Nigel Richards. Furthermore, I would like to thank James Watson and Matthew Woodhouse for their help with LaTeX and image editing.

On a more personal note, I would like to thank my family, especially my parents for their great support throughout my whole time at university.

Last but not least I thank my lovely wife Carolin. Her support and encouragement as well as her love kept me going and will keep me going in the next years and decades.

Abstract

Upper-level disturbances (ULDs) penetrating from the extratropics into low latitudes are a frequent feature of the synoptic-scale circulation over the North Atlantic and can be involved in significant weather events such as heavy precipitation over the western and northern parts of Africa, or Saharan dust outbreaks. The present project is the first to systematically explore the huge dynamical information content of long-term data from the European Centre for Medium-Range Weather Forecasts operational ensemble prediction system (EPS) and from the recently established THORPEX Interactive Grand Global Ensemble (TIGGE) for that particular atmospheric feature. It investigates the dynamics, forecast quality and predictability of this atmospheric phenomenon exploring a wide range of verification and analysis tools based on potential vorticity (PV). The main conclusions from this work are: (i) The EPSs shows a generally underdispersive behaviour in the ULD region. (ii) Forecast errors are reduced by about 50% if each TIGGE centre's own analysis is used instead of the ECMWF analysis, particularly in regions of large PV gradients. (iii) There is a tendency of too weak Rossby wave breaking and therefore a northward shift of the PV streamers in the forecasts. (iv) Ensemble-mean multi-model forecasts of a four-day accumulated precipitation event appear accurate enough for a successful severe-weather warning in contrast to some single-model EPSs. (v) Diabatic processes upstream early in the forecasts appear to be more important than blocking downstream for strengthening the PV streamers in the medium range. The results and the analysis tools developed in this project have improved the understanding of such ULDs and their impacts and has advanced the verification of EPSs, which can both contribute to an improvement of numerical weather forecasting in the long term.

Blank Page

Contents

Declaration of Authorship	i
Acknowledgements	iii
Abstract	v
Contents	vii
Abbreviations	xi
1 Introduction	1
1.1 Motivation	1
1.2 Scientific background	3
1.2.1 Rossby waves	3
1.2.1.1 Observations and climatology	7
1.3 Probabilistic forecasting	9
1.4 Aims and objectives of this work	11
1.5 Structure of thesis	12

2	Data	15
2.1	Ensemble Prediction System at ECMWF	15
2.2	THORPEX Interactive Grand Global Ensemble	18
2.3	Limitations of ECMWF stored data	20
2.4	Analysis and observation data	21
2.4.1	Analysis and reanalysis data	21
2.4.2	Observational data	22
3	Methods	25
3.1	PV derived from limited archived model data	25
3.2	PV streamer identification	28
3.3	Determination of PV streamer episodes	30
3.4	Definition of verification areas	32
4	Example PV streamer cases	35
4.1	Rossby wave breaking in summer and autumn 2008 and its consequences	35
4.2	Precipitation pattern associated with PV streamer	36
4.3	PV streamer influenced by ET from hurricane <i>Ike</i> in September 2008	38
5	Statistical analysis	43
5.1	PV streamer climatology	43
5.2	Forecast performances	49
5.2.1	Dispersive behaviour of EPS	49
5.2.2	Forecast histograms	55
5.2.3	Displacement error	56

6	Ensemble correlation analysis	59
6.1	Introduction and method	59
6.2	Example case	61
6.3	Statistical analysis over all PV streamer	66
6.4	Correlation signals from hurricanes	70
7	Model versus initial conditions errors	75
7.1	Method	75
7.2	Results	78
8	High-impact weather event in May 2008 - A TIGGE case study	81
8.1	Introduction	82
8.2	Methods	83
8.3	Synoptic overview	85
8.4	Forecast performance of large-scale evolution	87
8.4.1	Area-mean error measures	88
8.4.2	Feature based error measures	93
8.5	High-impact weather	95
8.5.1	Dust mobilization	95
8.5.2	Ensemble correlation of dust and PV	98
8.5.3	Precipitation	102
8.5.4	Ensemble correlation of precipitation and PV	104
9	Conclusions	107
9.1	Summary	107
9.2	Discussion	111

9.3	Résumé	113
9.4	Outlook	114
	References	117
	List of Figures	129
	List of Tables	143
	A Supplementary Figures	145
	B Technical details	157

Abbreviations

AWB	Anticyclonic Wave Breaking
BoM	Australian Bureau of Meteorology
CMA	Chinese Meteorological Agency
CMC	Canadian Meteorological Centre
CPTEC	Brazilian Centre for Weather Prediction and Climate Studies
CWB	Cyclonic Wave Breaking
DRW	Diabatic Rossby Wave
ECMWF	European Centre for Medium-range Weather Forecasts
EPS	Ensemble Prediction System
ERA	ECMWF Re-Analysis
ET	Extratropical Transition
IMPETUS	An Integrated Approach to the Efficient Management of Scarce Water Resources in West Africa
IR	InfraRed
ITCZ	Inter-Tropical Convergence Zone
JMA	Japanese Meteorological Administration
KMA	Korean Meteorological Administration
LC	Life Cycle
MSG	Meteosat Second Generation
MSC	Meteorological Society of Canada
MSLP	Mean Sea-Level Pressure
NAO	North Atlantic Oscillation
NASA	National Aeronautics and Space Administration
NCAR	National Center for Atmospheric Research
NCEP	National Centers for Environmental Prediction
NHC	National Hurricane Center
NOAA	National Oceanic and Atmospheric Administration

NWP	Numerical Weather Prediction
OTI	Optimisation Time
PANDOWAE	Predictability ANd Dynamics Of Weather systems in the Atlantic-European sector
PDU	Potential Dust Uplift
PV	Potential Vorticity
RMSE	Root Mean Square Error
RWB	Rossby Wave Breaking
SEVIRI	Spinning Enhanced Visible and InfraRed Imager
SV	Singular Vector
THORPEX	THE Observing system Research and Predictability EXperiment
THE	Equivalent potential temperature
TIGGE	THORPEX Interactive Grand Global Ensemble
TRMM	Tropical Rainfall Measurement Mission
UKMO	UK Met Office
ULD	Upper-Level Disturbance
VAREPS	VARIational Resolution Ensemble Prediction System
WMO	World Meteorological Organization
WCB	Warm Conveyor Belt
Z	Geopotential height

Chapter 1

Introduction

1.1 Motivation

One of the main goals of national weather services and research groups at universities or research centres working with numerical weather prediction (NWP) models is to improve forecasts, especially those of extreme cases and high-impact weather. The focus of this study is on upper-level disturbances, more precisely potential vorticity (PV) streamers stretching into low latitudes and causing high-impact weather (e.g. heavy precipitation events, flooding, dust storms) over the north African continent. In order to improve NWP, it is indispensable to verify the forecasts and to understand processes in NWP models. Over recent decades continuous improvement of deterministic forecasts have taken place, which has led to a similar accuracy for seven-day forecasts today compared to five-days forecasts in the mid-1980s (see Figure 1.1). Due to the chaotic behaviour of the atmosphere deterministic forecasts always have a level of uncertainty, leading to probabilistic forecasting systems. This is the first study to systematically investigate the predictability and dynamics of upper-level troughs over North Africa in predictions of ensemble forecasts.

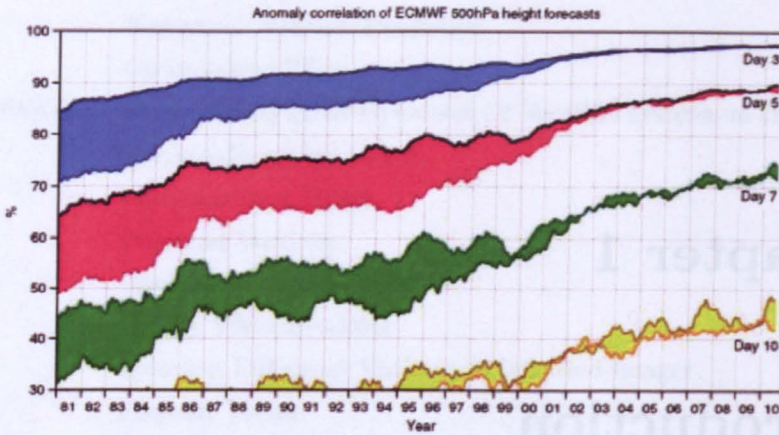


Figure 1.1: The evolution of forecast skill at ECMWF from 1981 to the present. The steady improvement with time can at least partly be ascribed to the improved use of satellite data and in particular the closing of the gap between the Northern and Southern Hemisphere as more and more satellite data are used in the otherwise data-sparse southern latitudes. For each day, the top of the coloured band represents the forecast skill in the Northern Hemisphere while the bottom represents the forecast skill in the Southern Hemisphere. Courtesy of ECMWF. Taken from Collard et al. (2011), plot adapted and extended from Simmons and Hollingsworth (2002).

The present work contributes to several national and international research projects. The World Meteorological Organization (WMO) programme The Observing System Research and Predictability Experiment (THORPEX) is a 10-year international research and development programme to accelerate improvements in the accuracy of one-day to two-week high-impact weather forecasts for the benefit of society, the economy and the environment. The novel data set THORPEX Interactive Grand Global Ensemble (TIGGE), which is a central project of THORPEX, is used for a comprehensive case study in this thesis. Furthermore different workshop participations and collaborations with the German research project Predictability and Dynamics of Weather Systems in the Atlantic-European Sector (PANDOWAE) have been very productive for both their studies and the work presented here. The PANDOWAE project aims to advance the knowledge and understanding of the dynamical processes responsible for the development of high-impact weather systems and to elucidate the factors that limit the predictability of such systems. The work in this thesis fits perfectly into these goals, in particular making use of recent advances in ensemble forecasting techniques.

1.2 Scientific background

1.2.1 Rossby waves

Temperature differences between the poles (cold, dense air) and the equator (warm, less dense air) result in latitudinal pressure gradients where the pressure force is directed polewards. The Coriolis force caused by the Earth's rotation forces air to turn right (left) in the Northern (Southern) Hemisphere. The balance of pressure gradient and Coriolis force is called geostrophic balance and results in westerlies in the mid-latitudes. Regions of strong winds, called jet streams, exist at the tropopause. These are caused by extreme temperature gradients in the lower troposphere. Jet streams are explained by the thermal wind concept, which states that the vertical wind velocity gradient is proportional to the horizontal temperature gradient ($\frac{\partial T}{\partial y} \sim \frac{\partial u}{\partial z}$). At the jet streams waves form with typical wavelength of 4000 km, which correspond fairly well to what is observed in synoptic meteorology. This atmospheric feature is named after Carl Gustav Rossby. Rossby waves are the dominant dynamical feature of the upper troposphere in the mid-latitudes (e.g. Hoskins and Ambrizzi, 1993).

A Rossby wave originates at strong gradients in vorticity ($\zeta = \nabla \times \vec{u}$) fields. Figure 1.2 shows a sketch of two different vorticity fields. A strong gradient occurs at the boundary between ζ_1 and ζ_2 . A perturbation (e.g. an orographic trigger in the real atmosphere) at the boundary can move lower vorticity into higher vorticity and vice versa, resulting in a circulation field. A Negative vorticity anomaly is associated with anticyclonic circulation and a positive anomaly generates cyclonic circulation. The initiated circulations cause anomalies up- and downstream and create a westward propagating vorticity field. (Holton, 2004)

These planetary waves are governed by variations of the Coriolis force with latitude, which is related to vorticity. Absolute vorticity is defined as a sum of the relative vorticity ζ and the Coriolis parameter f

$$\eta = \zeta + f \tag{1.1}$$

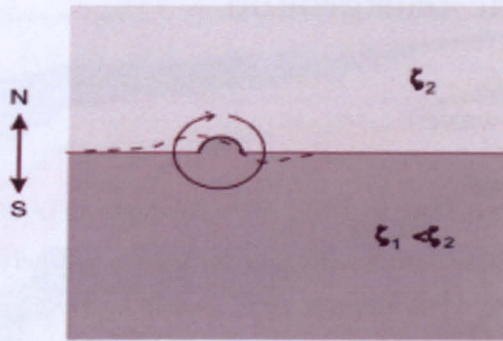


Figure 1.2: Two fields, of uniform, but different, vorticity ζ_1 and ζ_2 are displayed on an east-west boundary. A perturbation in the vorticity field and the resulting circulation is shown (taken from Holton, 2004).

The scalar product of the absolute vorticity vector and the gradient of potential temperature is defined as PV.

$$PV = \frac{1}{\rho} \vec{\eta} \cdot \nabla \theta \quad (1.2)$$

In adiabatic flow and in absence of friction PV is conserved.

Flow over large mountain ridges leads to compression at the windward side, resulting in a decrease in relative vorticity, an anticlockwise turning and therefore an equatorwards flow in the northern hemisphere. A stretching of the air in the lee of the mountain ridge causes a cyclonic turning leading to a poleward flow. The stretching concept is shown in Figure 1.3. Once the wave is initiated it is maintained by the need for PV to be conserved. As air moves poleward the Coriolis parameter increases so in order to maintain absolute vorticity the relative vorticity decreases. By decreasing the relative vorticity it increasingly becomes anticyclonic circulation and the air turns equatorwards. (Gill, 1982)

Thermal forcing from heating differences associated with land and sea distribution and forcing from interactions with smaller scale circulations such as extratropical cyclones act as an initiator of Rossby waves, too (Lynch and Cassano, 2006).

In cases of non-linear amplification Rossby wave breaking (RWB) can occur. A

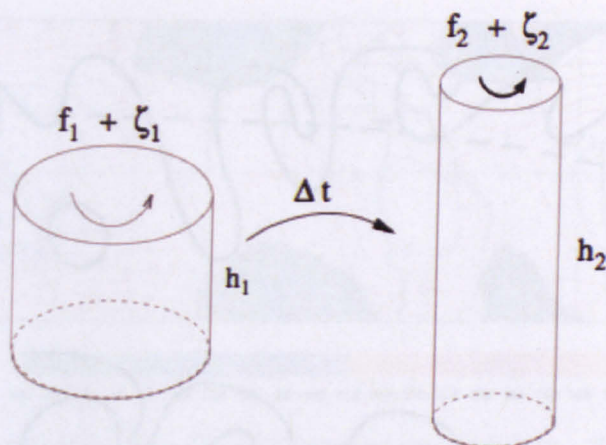


Figure 1.3: Vortex stretching and PV conservation. If a material column is stretched to a greater thickness ($h_2 > h_1 > 0$) while conserving its volume, the PV conservation, $PV_2 = PV_1 > 0$ implies an increase in the absolute vorticity, $f(y_2) + \zeta_2 > f(y_1) + \zeta_1 > 0$ (taken from McWilliams, 2006)

RWB is defined to occur when fluctuations in horizontal direction reach an irreversible state (McIntyre and Palmer, 1983). Regions with the highest occurrence of RWB are at the downstream end of storm tracks (Wernli and Sprenger, 2007). Berggren et al. (1949) and Rossby (1959) were among the first to show the propagation of a Rossby wave train over the North Atlantic, its amplification, and the non-linear wave breaking.

The fastest Rossby wave propagation is associated with the jet stream, which acts as a waveguide (Schwierz et al., 2004b) and coincides with the strongest isentropic gradients of PV that characterise the extratropical tropopause (Hoskins et al., 1985). RWB can result in elongated tongues of high-PV stratospheric air extending equatorwards and downwards into the troposphere. Finally narrow filaments called PV streamers can develop and eventually break up into distinct PV cut-offs (Appenzeller and Davies, 1992). Using idealised modelling, Davies et al. (1991) and Thorncroft et al. (1993) demonstrated that stratospheric filaments can form through dry dynamics and are part of the baroclinic life cycle. Massacand et al. (2001) noted that upstream diabatic heating might be crucial for the development of some real-world PV streamers. Cloud-diabatic heating effects were found to influence the evolution of a PV streamer, leading to heavy precipitation over the Alps,

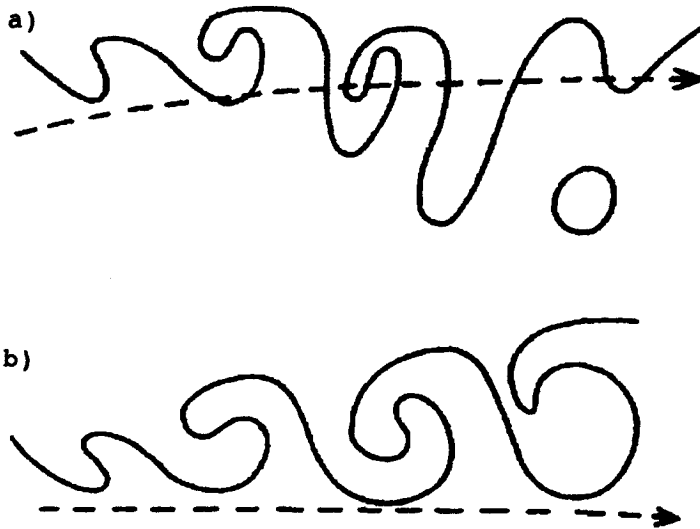


Figure 1.4: Schematic of two types of Rossby wave breaking with a) an LC1-type life cycle and b) an LC2-type life cycle. The dashed line marks the approximate position of the mean jet stream at each stage (taken from Thorncroft et al., 1993).

by creating a negative PV anomaly at the tropopause downstream of the heating event. Stoelinga (1996) showed that the strengthening of low PV associated with latent heating can influence the downstream PV streamer. For example Boettcher and Wernli (2011) showed that diabatic heating in the mid-troposphere can produce a so-called diabatic Rossby wave (DRW defined in Parker and Thorpe, 1995) over the Atlantic basin. If these small scale mid-tropospheric waves interact with a PV anomaly at the tropopause, the combination can lead to explosive cyclogenesis.

Thorncroft et al. (1993) pioneered the concept of two types of RWB life cycles (LCs). The anticyclonic wave breaking (AWB) named LC1 and the cyclonic wave breaking (CWB) termed LC2. Figure 1.4 shows schematics of the two life cycles, with the evolution of the RWB over time depicted from left to right. The position of the mean jet stream is drawn as a dashed line.

As evident in Figure 1.4 both LCs start with a similar trough located north of the mean jet maximum. LC1 starts with a cyclonic roll-up and changes its behaviour when it becomes exposed to the anticyclonic shear on the southern side of the jet

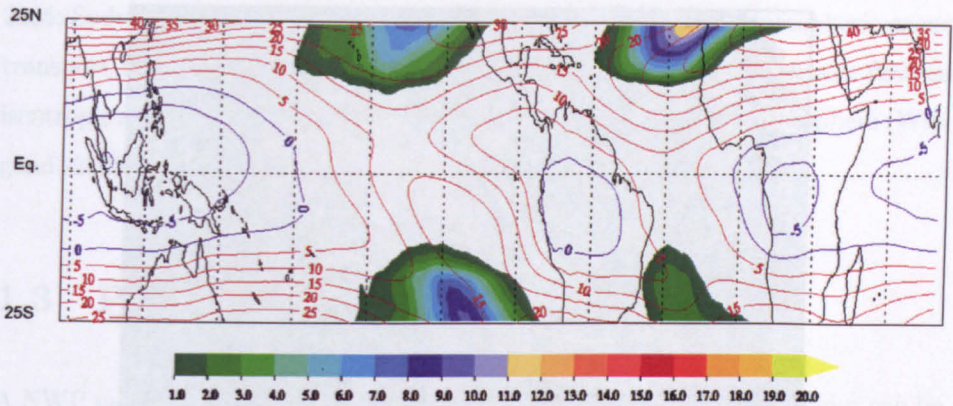


Figure 1.5: Occurrence frequency [%] of PV intrusions into low latitudes 200 hPa zonal wind (contours) in boreal winter (October-March). Data: ECMWF Re-Analysis40 from 1980 to 2001 (taken from Froehlich and Knippertz, 2008, (slightly modified)).

stream. In the following the upper-level wave stretches from northeast to southwest. Thereafter it narrows in its zonal extent and possibly breaks up into a cut-off vortex. LC2 shown in Figure 1.4b remains cyclonic because of its northern position to the jet characterised by cyclonic shear. The wrap-up stays relatively broad and no cut-off occurs. As explained the life cycles differ in the upper-level development. Furthermore the synoptic evolution of associated cyclones, warm/cold fronts and anticyclones are different under LC1 or LC2 conditions, too (e.g. Wernli et al., 1998).

1.2.1.1 Observations and climatology

As explained above, RWB can lead to narrow filaments called PV streamers, which are a common feature in the atmosphere. Several studies in the past were focused on observations and climatologies of these PV streamer events. The northern hemispheric seasonal variability of PV streamers has its maximum in summer (Postel and Hitchman, 1999; Abatzoglou and Magnusdottir, 2004; Wernli and Sprenger, 2007).

PV streamers, which penetrate from the extratropics into the low latitudes, are the main focus of this project. These deep equatorward moving PV streamers mainly occur over the central and eastern Pacific and the Atlantic Ocean during

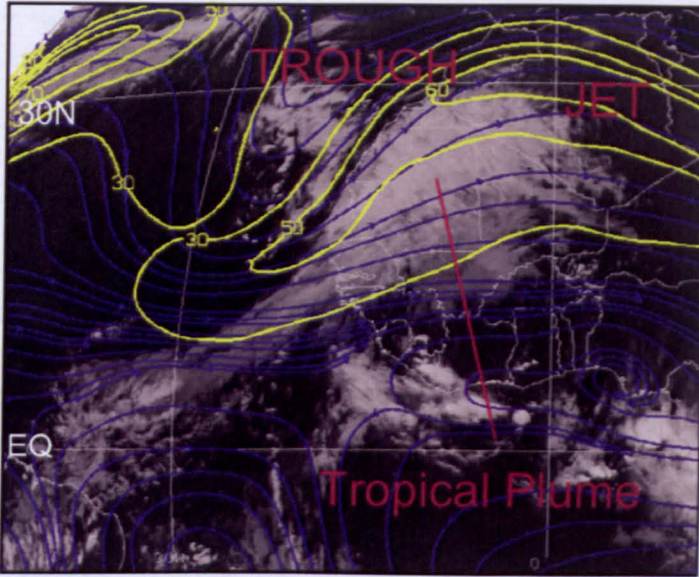


Figure 1.6: Meteosat IR satellite images with superimposed isotachs at the 345 K isentropic level in yellow (ms^{-1}) and streamlines in blue at 00 UTC 10 January 2002 (taken from Knippertz and Martin, 2005).

boreal winter and spring (Waugh and Polvani, 2000; Kiladis and Weickmann, 1997; Froehlich and Knippertz, 2008). Froehlich and Knippertz (2008) found fewer PV streamers over the low-latitude North Atlantic in summer compared to winter. Furthermore they found the highest global frequency in winter in the North Atlantic compared to other ocean basins as it is shown in Figure 1.5.

PV streamers or cut-offs can trigger tropical convection (Kiladis and Weickmann, 1992; Slingo, 1998) as well as mid- and high-level pole- and eastward extending cloud bands from the Tropics into the Subtropics denoted as Tropical Plumes (McGuirk et al., 1987, 1988; Iskenderian, 1995; Knippertz, 2005). Figure 1.6 shows an example of a Tropical Plume occurring east of the upper-level trough. Poleward moisture transport east of the PV streamer is frequent, which can lead to heavy precipitation events (Knippertz and Martin, 2005, 2007). Furthermore Knippertz and Fink (2008, 2009) showed an influence of extratropical troughs on dry season precipitation in tropical west Africa associated with a north shift of the Inter-Tropical Convergence Zone (ITCZ). Large-scale Saharan dust outbreaks are another significant meteorological phenomenon associated with PV streamers (Barkan et al.,

2005; Sodemann et al., 2006; Slings et al., 2006). Furthermore stratospheric ozone transport into the tropical troposphere occurs in RWB situations, where flow on isentropic surfaces can bring ozone rich stratospheric air into the troposphere (Wiegand, 2008).

1.3 Probabilistic forecasting

A NWP model predicts the time evolution of the atmosphere. Its behaviour can be described by a set of physical laws mathematically expressed as differential equations. These include Newton's law of motion, the continuity equation, the first law of thermodynamics and the equation of state for ideal gases. The differential equations cannot be solved analytically. For a numerical solution the three dimensional meteorological variables (e.g. temperature T , pressure p , wind velocity \vec{u} and specific humidity q) need to be discretised. After discretisation a set of coupled differential equations becomes the basis for the predictions. Furthermore subgrid-scale processes (e.g. deep convection, boundary layer turbulence) need to be parametrised to represent these processes at the resolvable scale of the NWP model. To start an NWP simulation an initial state of the atmosphere is needed. To obtain such a state as near as possible to the truth, data assimilation techniques have been developed. These techniques assimilate the inhomogeneous observations into the grid cell model. A short-range forecast (3 or 6 h) usually serves as a first guess and the observations available at this time step are assimilated to give an analysis field. For a good NWP model the initial state is crucial for a successful forecast. Small changes in the initial conditions can cause large differences at later stages in the forecast.

Lorenz (1963) explored the chaotic behaviour of the atmosphere with a low-dimensional three parameter experiment. A chaotic flow is characterised by its non-linear behaviour and its sensitivity to initial conditions. A deterministic forecast is a forecast initialised with complete, sufficiently accurate initial conditions. It produces a single forecast result without any indication how uncertain this evolution is. An

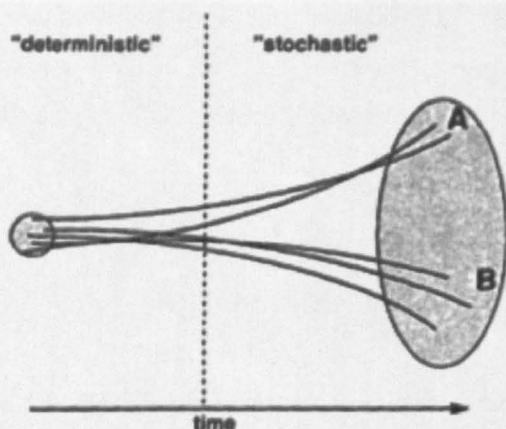


Figure 1.7: Schematic of ensemble prediction, with individual trajectories drawn for forecasts starting from a representative set of perturbed initial conditions within a circle representing their uncertainty and ending within a range of possible solutions, represented by the ellipse. For the shorter range, the forecasts are close to each other and they may be considered deterministic, but beyond a certain time, the forecast is stochastic. Forecasts may cluster into groups of similar trajectories (denoted A and B), whose probability may be related to the number of forecasts in each group (taken from Tracton and Kalnay, 1993).

ensemble of forecasts, or technically the ensemble forecast initialisation, tries to consider uncertainty. Weather, seasonal as well as climate prediction models are increasingly run as a set of forecasts with differing initial conditions and some with modulated model formulations, so-called stochastic physics.

A schematic of an ensemble forecast is shown in Figure 1.7. At the beginning the forecasts lie close together after starting from slightly perturbed initial conditions. At this stage in the forecast they can be called deterministic. After a certain time the forecasts start to spread and show a larger spectrum of possible solutions. Examining how far and after which time the solutions diverge from each other allows a quantification of the uncertainty. Different techniques have been created to find the fastest growing disturbances to represent the full uncertainty in the forecast.

The European Centre for Medium-Range Weather Forecasts (ECMWF) uses the singular vector (SV) method to achieve maximum perturbation growth rate for a given (48 hours) optimisation time (Palmer, 1993). SVs are calculated with a tangent linear model, firstly introduced by Lorenz (1965). The tangent linear

model is the Jacobian of the coupled differential equations of the NWP model explained before. The tangent linear propagator L describes the evolution of the perturbation from t_0 to t_1 . The transpose of the tangent linear model L^T describes the evolution from t_1 to t_0 . Solving the eigenvalue problem the initial SVs are obtained as eigenvectors of $L^T L$. (Kalnay, 2002)

The National Centers for Environmental Prediction (NCEP) use the ensemble transform (ET) technique (Wei et al., 2008), which is an improved version of the breeding vector (BV) technique (Toth and Kalnay, 1993) to perturb the initial conditions. The breeding perturbations use a previous ensemble to obtain the growing component of the analysis error.

It can be summarised that an ensemble forecast including information on 'probability, uncertainty and reliability' and is of greater value than the deterministic forecast alone (Tracton and Kalnay, 1993). Ensemble forecasting is one of the key future technologies. In addition to meteorology it has many applications in other fields like hydrology (e.g. flood forecasting) or socio-economic impacts, e.g. planning and risk management activities in sectors like government, financial and insurance; energy supply and demand (including renewable energy) and many more.

1.4 Aims and objectives of this work

As discussed in Section 1.2, Rossby wave formation, propagation and subsequent non-linear breaking is a common feature in the atmosphere. It still remains to find the factors that control the penetration of PV streamers to low latitudes, and how well these factors and PV streamers are predicted. For these purposes ensemble forecasts are used.

The focus of this study more specifically is on PV streamers that penetrate into northern Africa. An identification and tracking algorithm has to be developed to find PV streamer episodes in (re-)analyses. A major aim in this thesis is to study the forecast quality and predictability over lead time of these cases with

respect to errors of forecast position and intensity. The spread of the ensemble gives an indication of the predictability of the meteorological phenomenon under study. What the dynamical features that influence the forecast of subtropical PV streamers are, is another important question. Last but not least one of the goals of this project is to assess the implications of systematic errors in the PV streamer forecasts for the prediction of high-impact weather, especially extreme precipitation and dust mobilization.

Ensemble forecasts have been employed relatively little in dynamical research studies so far. Ensemble techniques were first operationally implemented in the 1990s. Now the data record is long enough for a statistically meaningful investigation of certain phenomena. As the different member runs start from initial conditions within the range of possible states of the atmosphere all forecasts are 'realistic' realisations of possible evolutions. This feature of ensemble forecasts allows a direct assessment of physical mechanisms and of the predictability of a certain process by showing its sensitivity to initial conditions. Therefore another aim of this study is to test and develop diagnostic tools and methodologies to verify EPS forecasts.

1.5 Structure of thesis

The thesis continues with a chapter describing the different data used in this study. Chapter 3 explains the methods applied to these data to reach the goals and aims stated above. Chapter 4 describes the synoptic evolution of some selected PV streamers and the associated weather, followed by a statistical analysis in Chapter 5, where the forecast performances of PV streamers is examined. Chapter 6 comprises a detailed look into ensemble forecasts of PV streamers with a new ensemble correlation technique. Possible future improvements of the ensemble prediction systems will be investigated in Chapter 7. The result chapters finish with Chapter 8, where a PV streamer case study, which happened in May 2008 and caused two types of related high-impact weather, a dust storm and heavy precipitation

and flooding, are evaluated with TIGGE forecasts. Conclusions, discussion and a summary are given in Chapter 9.

Blank Page

Chapter 2

Data

The main dataset used in this analysis is derived from the EPS from ECMWF. Additionally the new joined dataset of ensemble forecast products from different centres, denoted as TIGGE, served as the basis for a comprehensive case study. Furthermore observational products (satellite images, precipitation data) and (re-)analysis data are used within the framework of this thesis. The datasets will be explained in the following chapter.

2.1 Ensemble Prediction System at ECMWF

The Ensemble Prediction forecasting System, now running operationally twice daily at the ECMWF, started in December 1992 with one forecast per day at 1200 UTC (Palmer et al., 1993; Molteni et al., 1996). The ensemble is using the numerical weather prediction model, with half the resolution of the operational deterministic version. Table 2.1 summarises the changes of the ECMWF EPS based on documentations available from the ECMWF website (ECMWF, 2011b). The EPS system was initially based on 33 model runs at a spectral resolution T63L19, i.e. truncation after wave number 63 (corresponds to ~ 180 km grid point spacing) and 19 vertical levels. One member, the so called control forecast, was initiated with the 12 UTC operational analysis. The remaining 32 members were calculated from

Table 2.1: Changes in the Ensemble Prediction System at the ECMWF from the implementation in 1992 to 2007. The abbreviations used in the table are as follows: SV: singular vector; NH: Northern Hemisphere; SH: Southern Hemisphere; TR: Tropics; TX: spectral triangular truncation at total wavenumber x ; and TL x : spectral triangular truncation at total wavenumber x with linear reduced Gaussian grid; HRes: Horizontal Resolution; VRes: Vertical Resolution; #: Number of EPS members including the control forecast; Stochastic Physics; d: days; h: hours.

Date	Description	Singular Vector's characteristics				Forecast characteristics				
		HRes	VRes	OTI	Target Area	HRes	VRes	Length	#	SP
Dec 1992	operational implementation	T21	L19	36h	NH	T63	L19	10d	33	No
Aug 1994	SV optimisation time	"	"	48h	"	"	"	"	"	"
Mar 1995	SV horizontal resolution	T42	"	"	"	"	"	"	"	"
Mar 1996	NH + SH SV	"	"	"	NH + SH	"	"	"	"	"
Dec 1996	resolution/members	"	L31	"	"	TL159	L31	"	51	"
Mar 1998	evolved SV	"	"	"	"	"	"	"	"	"
Oct 1998	Stochastic Physics	"	"	"	"	"	"	"	"	Yes
Oct 1999	vertical resolution	"	L40	"	"	"	L40	"	"	"
Nov 2000	FC horizontal resolution	"	"	"	"	TL255	"	"	"	"
Jan 2002	Tropic SVs	"	"	"	NH + SH + TR	"	"	"	"	"
Feb 2006	resolution	"	L62	"	"	TL399	L62	"	"	"
Sept 2006	VAREPS	"	"	"	"	TL399(0-10d), TL255(10-15d)	"	15d	"	"

perturbations applied to the 12 UTC analysis (Buizza et al., 1998; Barkmeijer et al., 1999). The perturbations are calculated with the singular vector (SV) technique, started from 1992 with a T42L19 resolution model and an optimisation time (OTI) of the SVs of 36 hours (more details of the SV technique are described in Section 1.3). The OTI increased to 48 hours in August 1994, which it still is today. The SVs were not calculated over the whole globe from 1992 to 2002. Three regions were distinguished: both hemispheres from 30° polewards and the tropics (30°N-30°S). In the first EPS versions from 1992 to March 1996 only SVs in the Northern Hemisphere were implemented to disturb the initial conditions. In 1996 the Southern Hemisphere was included and at the beginning of 2002 targeted moist SV calculations in the tropics have been added. Furthermore, only uncertainties in the initial conditions were simulated without taking into account errors due to model uncertainties. (Buizza and Palmer, 1995)

Buizza et al. (1998) found that increasing ensemble size and model resolution improves the ensemble skill. From December 1996 onwards the operational system has been running with 51 members including the control forecast. Due to this step in the development of the EPS, this study focuses on forecasts from the end of 1996 to 2008 only. Together with the increase of members the horizontal and vertical resolutions were increased to TL159L31 (TL159: spectral truncation at total wavenumber 159 with linear reduced Gaussian grid. Details in Appendix B). Additionally, Buizza et al. (1998) indicated that the ensemble spread was still underestimated, which they ascribed to the neglect of uncertainties caused by model errors. Therefore the 'stochastic physics' scheme and an improved version of the SVs were implemented in March and October 1998, which led to an increased spread (Buizza et al., 1998).

In recent years, a stepwise upgrade of the model resolution both in the horizontal and vertical, was achieved. The highest model resolution used in this study is TL399L62 in the EPS system and T42L62 for SV calculation from February 2006 to the end of 2008. The Variational Resolution Ensemble Prediction System (VAREPS) implemented in 2006, is characterised by the change in the model resolution at day 10.

At the time of writing the model runs twice daily with resolution TL639L62 (~32 km) until day 10 and TL319L62 (~65 km) from day 10 to day 15. Vertical resolution has been enhanced to T42L62. The operational deterministic model currently runs twice daily with resolution TL1279L91 (~16 km) until day 10.

2.2 THORPEX Interactive Grand Global Ensemble

In 2005 a World Weather Research Programme called TIGGE was initiated at a workshop at ECMWF (Richardson et al., 2005). The main goal of this workshop was to enhance collaboration on the development of ensemble prediction between operational centres and universities by increasing the availability of EPS data for research. Since the 01 February 2008 ten operational weather forecasting centres have been delivering near-real time (48 hours delay) ensemble forecast data to three TIGGE data archives located at ECMWF, the National Center for Atmospheric Research (NCAR) and the Chinese Meteorological Agency (CMA). In addition to the above mentioned ECMWF and CMA, the following eight weather centres are participating: the Australian Bureau of Meteorology (BoM), the Canadian Meteorological Centre (CMC), the Brazilian Centre for Weather Prediction and Climate Studies (Centro de Previsão de Tempo e Estudos Climáticos, CPTEC), the Japanese Meteorological Administration (JMA), the Korean Meteorological Administration (KMA), NCEP, the UK Met Office (UKMO) and Météo France.

Table 2.2 summarises the characteristics of the different centres' EPS in May 2008. A predictability study of a Saharan dust outbreak and extreme precipitation at the European Alpine south side caused by a PV streamer, is discussed in Chapter 8. The focus of this case study is on one to ten day forecasts. Only 1200 UTC forecasts were used for this study because nine out of ten centres start forecasts at this time. Unfortunately Météo France could not be included in this study because the maximum available forecast lead time is 2.5 days and forecasts start at 1800 UTC. The models of the different centres differ in many aspects. First, the number of

Table 2.2: Characteristics of the nine EPSs participation in TIGGE in May 2008. The abbreviations used in the table are as follows: SV: singular vector; BV: bred vector; ET: ensemble transform; EnKF: ensemble Kalman filter; ETKF: ensemble transform Kalman filter; EOF: empirical orthogonal function; NH: Northern Hemisphere; SH: Southern Hemisphere; TR: tropics; GenSI: generalised multivariate statistical interpolation; 3-/4DVar: 3-/4-dimensional variational data assimilation; GSI: gridded statistical interpolation; Tx: spectral triangular truncation at total wavenumber x; and TLx: spectral triangular truncation at total wavenumber x with linear reduced Gaussian grid. Abbreviations of the centres' names are found in the text.

Centre	Horizontal resolution	No. of levels	No. of members	Initial perturbations	Perturbation model physics	Forecast length (days)	Forecast frequency (UTC)	Data assimilation
BoM	TL119 (1.5°)	19	32	SVs (NH, SH)	No	10	0000, 1200	GenSI
CMA	T213 (0.5625°)	31	14	BVs (globe)	No	10	0000, 1200	GSI
CMC	TL149 (1.2°)	28	20	EnKF (globe)	Yes	16	0000, 1200	4DVar
CPTEC	T126 (0.9474°)	28	14	EOF (45°S-30°N)	No	15	0000, 1200	NCEP analysis
ECMWF	TL399 (0.45°), TL255 (0.7°)	62	50	SVs (globe)	Yes	0-10 10-15	0000, 1200	4DVar
JMA	TL319 (0.525°)	60	50	SVs (NH, TR)	No	9	1200	4DVar
KMA	T213 (0.5625°)	40	16	BVs (NH)	No	10	0000, 1200	3DVar
NCEP	T126 (0.9474°)	28	20	ET (globe)	No	16	0000, 0600, 1200, 1800	GSI
UKMO	1.25° × 0.83°	38	23	ETKF (globe)	Yes	15	0000, 1200	4DVar

ensemble members ranges from 14 to 50 and the number of vertical levels from 19 to 62. Second, the ensemble systems use different data assimilation techniques as well as different methods of perturbing the initial conditions. CPTEC uses NCEP analysis as a basis for their forecasts. Only some model's (CMC, ECMWF and UKMO) physics are perturbed. Third, the grid spacing of the forecast models range from 0.5° to 1.5° . However, only two models have coarser resolutions than 1° . All meteorological fields evaluated in Chapter 8 are extrapolated to a $1^\circ \times 1^\circ$ grid. More details on TIGGE are available in Bougeault et al. (2010) and Froude (2010, Table 1).

2.3 Limitations of ECMWF stored data

The model data described above has been taken from the ECMWF archive MARS (Meteorological Archival and Retrieval System). All longitude-latitude grid data retrieved from the ECMWF through the MARS archive are on a grid, where a longitude or latitude specification as a certain value throughout this work denotes the centre of a grid box, i.e. in a $1^\circ \times 1^\circ$ grid a latitude 30°N stands for 29.5°N to 30.5°N . This grid has been taken care off in all cases where model data are compared to data from other sources, e.g. precipitation data described below. For inter-comparisons of model data the retrieved grid is used.

As storage space is limited, some data are not archived at all model levels. In particular EPS data is only for five pressure levels (50, 200, 500, 700 and 925 hPa) are available. This fact has an influence on the PV derived from EPS data and will be explained in Chapter 3.

2.4 Analysis and observation data

2.4.1 Analysis and reanalysis data

To evaluate models it is necessary to have data which represent the true state of the atmosphere as close as possible. Different datasets have advantages and disadvantages. Data from direct observations are not available in spatial gridded resolution, are often not available over a long period of time and usually contain instrumental errors. Because of these problems different model analysis data are used. They are the best approximation of the true state of the whole (gridded) atmosphere. It should be noted that the model may bias the analyses or create artefacts. Data assimilation systems attempt to take into account errors of the different sources of information (models, observations). Many different data assimilation methods have been developed. The analysis is produced by a short-range forecast (e.g. 6 hours) and the assimilation of observations around this time. In this study operational analyses as well as the ECMWF Re-Analysis (ERA) - 40 dataset from the ECMWF are used (Uppala et al., 2005). A reanalysis is calculated with a constant model setup (resolution, data assimilation) over a certain time period. ERA-40 was calculated for September 1957 to August 2002. The spectral resolution of the used model version is T159L60, which corresponds to 1° in a longitude/latitude grid. The follow-up reanalysis project from ECMWF is ERA-interim, which started in 1989 and is updated daily (Berrisford et al., 2009). Reanalysis data is only influenced by changes in observations over the years and not by model changes as it is the case in operational analysis data. Therefore reanalysis data are more suitable for statistical investigations. Additional to ECMWF analyses, analyses from the TIGGE centres mentioned in 2.2 are used.

2.4.2 Observational data

To illustrate dust mobilization and transport, visible satellite images and an RGB composite were used. The RGB product is based on brightness temperature differences from the 8.7, 10.8 and 12.0 μm wavelength infrared channels. With a sampling rate of 15 minutes and a spatial resolution of 3 km at nadir, the radiances in twelve channels are measured by the Spinning Enhanced Visible and Infrared Imager (SE-VIRI) instrument onboard the geostationary Meteosat Second Generation (MSG) satellite at 3.5°E (for more details, see Schepanski et al., 2007).

Verification of precipitation was achieved with different datasets. Over Europe the Ensembles-Based Predictions of Climate Changes and Their Impacts (ENSEMBLES) E-OBS (Haylock et al., 2008) dataset was used, where amounts from rain gauges over land areas are gridded. The Tropical Rainfall Measurement Mission (TRMM) was applied to show rainfall periods over Africa. TRMM is a satellite product using microwave and visible-infrared estimates and a space-borne precipitation radar adjusted with rain gauges (technical details in Huffman et al., 2007) and were retrieved from the National Aeronautics and Space Administration (NASA) website (NASA, 2009).

Additionally, the National Hurricane Center's (NHC) Tropical Cyclone Reports (NHC, 2010) were used for comparison of the analysed tracks of hurricanes with the results in Chapter 6.

The North Atlantic Oscillation (NAO) index is used to check if there are connections between the studied deep extratropical intrusions and the NAO. The index describes the north-south pressure dipole over the North Atlantic located over Greenland/Iceland ("Icelandic Low") and the subtropical latitudes (35° - 40°, "Azores High") (Hurrell, 1995). The positive phase defines below-normal pressure at high latitude and above-normal pressure at low latitudes, which leads to wet conditions in central and northern Europe and dry conditions in southern Europe. Wet conditions in southern Europe and the northern Sahara are described by the negative phase, which is defined by the opposite patterns of the pressure anomalies. The

NAO data has been obtained from the National Oceanic and Atmospheric Administration (NOAA) Climate Prediction Center (NOAA Climate Prediction Center, 2011) .

Blank Page

Chapter 3

Methods

The following chapter explains most of the used methodologies and techniques to achieve the aims of the present work in the result chapters 4 to 8. The chapter starts with the explanation of deriving PV from model output and the identification of the PV streamers then continues with the description of different verification tools.

3.1 PV derived from limited archived model data

The PV concept initiated by Hoskins et al. (1985) has been entrenched in the field of dynamical meteorology over the last decades. Several studies used this variable in the past years to illustrate the evolution and movement of the atmosphere. Therefore this study uses PV to analyse the dynamics of the upper troposphere. Equation 3.1 is the definition of the so called Ertel-PV in Cartesian coordinates

$$PV_{Ertel} = \frac{1}{\rho} \vec{\eta} \cdot \vec{\nabla} \Theta \quad (3.1)$$

where ρ is the density, Θ the potential temperature and $\vec{\eta} = \vec{\nabla} \wedge \vec{u} + 2\vec{\Omega}$ the vector of the absolute vorticity with $\vec{\Omega}$ being the Earth rotation vector. On the synoptic scale (>1000 km) the third term of the vector product in Equation 3.1 dominates. The full Ertel PV is therefore usually well approximated by the product of vertical

stability and the vertical vorticity component, in Cartesian coordinates Equation 3.2 and pressure coordinates Equation 3.3

$$PV \cong \frac{1}{\rho} \frac{\partial \Theta}{\partial z} \cdot (f + \xi) \quad (3.2)$$

$$PV_p \cong -g \frac{\partial \Theta}{\partial p} \cdot (f + \xi_p) \quad (3.3)$$

where $f = 2\Omega \sin\phi$ denotes the Coriolis parameter with ϕ being the latitude and $\xi = \frac{\partial v}{\partial x} - \frac{\partial u}{\partial y}$ the vertical component of the relative vorticity. In Equation 3.3 the derivatives of ξ_p are taken on surfaces of constant pressure.

Usually PV from model output data are calculated at every vertical model level with Equation 3.2. Θ and ξ are direct model output variables or can be easily derived. As mentioned in Section 2.3, ECMWF archived the ensemble prediction system data at five pressure levels only (50, 200, 500, 700 and 925 hPa) until 2006. Due to that fact, Equation 3.4 is used for calculating upper-tropospheric PV fields for this study.

$$PV_p \cong -g \frac{\partial \Theta}{\partial p} \cdot (f + \bar{\xi}_p) \cong -g \frac{\Theta_{500} - \Theta_{200}}{300hPa} \cdot (f + \frac{\xi_{500} + \xi_{200}}{2}) \quad (3.4)$$

Θ and ξ at both pressure levels are archived directly at the ECMWF.

Figure 3.1 shows an example date calculated with the two different methods. In Figure 3.1a the PV results from calculating PV at model levels, interpolate it to 200 and 500 hPa and average both fields. The resulting PV in Figure 3.1b comes from calculating PV from potential temperature and relative vorticity from the 200 and 500 hPa p-levels (Equation 3.4). Operational analysis data is used for both ways of calculation. It should be noted that the absolute PV values calculated with Equation 3.4 (Figure 3.1b) are generally smaller. The PV field at this date indicates a PV reservoir over the North Atlantic with a PV maximum along the east coast of the American continent and Greenland. Furthermore a wave breaking

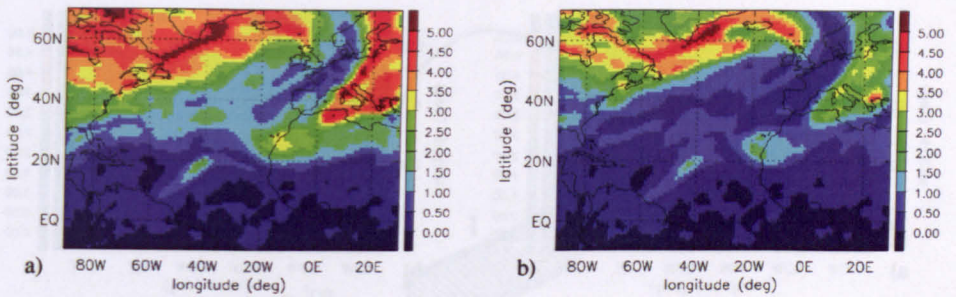


Figure 3.1: Comparison of two upper-level PV fields calculated in different ways from model analysis data for the same date. Left: Calculation of PV at every model level, interpolation to 200 and 500 hPa and averaging both fields. Right: Calculation of PV with potential temperature and relative vorticity at 200 and 500 hPa using Equation 3.4.

event took place east of the PV reservoir. This is characterised by a poleward breaking (also called negative PV streamer) situated over Western Europe. The elongated PV streamer with its southern tip over Northern Africa originated from the wave breaking as well. The general PV structures are evident in both PV fields (Figure 3.1a and b). Therefore it can be summarised that the structure in both fields corresponds satisfactorily. Several studies, (e.g. Appenzeller et al., 1996), defined the dynamical tropopause at 2 PVU (Potential Vorticity Unit, $1 \text{ PVU} = 10^{-6} \text{ m}^2 \text{ s}^{-1} \text{ K kg}^{-1}$). $\text{PV} > 2 \text{ PVU}$ corresponds to the stratosphere and $\text{PV} < 2 \text{ PVU}$ are tropospheric values. The value in Figure 3.1b is reduced by approximately 0.5 PVU, which defines the dynamical tropopause to 1.5 PVU for this study. Details on this definition follow in Section 3.2.

The same example date as in Figure 3.1 is used to assess how much a PV field varies under the change of the employed model resolution. Both PV fields in Figure 3.2 are calculated with Equation 3.4. For Figure 3.2a the used data is a 1° by 1° grid resulting in the same PV field as Figure 3.1b. The Θ and ξ_p data used was then interpolated to a 2.5° by 2.5° grid before PV calculation. Figure 3.2b shows, compared to Figure 3.2a, fewer small-scale structures, e.g. the high PV area south of Iceland, which has a slightly different hook shape and the PV value is somewhat smaller. It can be said that the absolute PV values are slightly smaller only on small features, e.g. the high PV values over Greece. In total the synoptic-scale features in the fields from different resolution match satisfactorily and the loss of

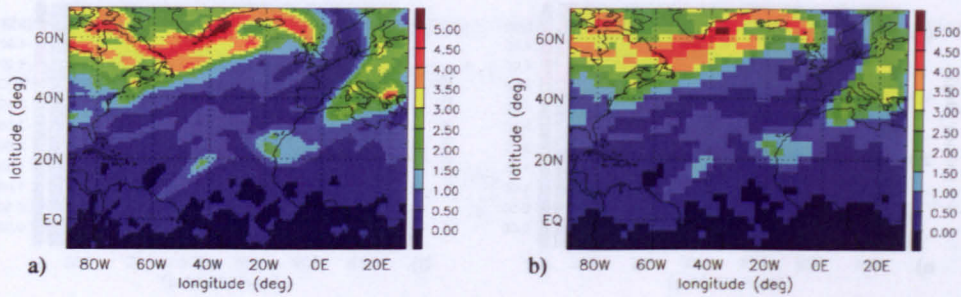


Figure 3.2: Comparison of two similar upper level PV fields calculated on different grid resolutions. Left: 1° by 1° , right: 2.5° by 2.5° .

structure in the coarser resolution can be tolerated for the large scale investigation performed in this work.

An additional fact led to the decision for the usage of coarser resolution. The coarser resolution data saves disk space during the whole project as it should be noted that for every forecast step two variables at two levels for 51 members had to be downloaded and processed et cetera. The decision of using the coarser grid to save storage space also led to the choice of investigating the EPS forecast just for cases when a PV streamer occurred in the analysis. Therefore this analysis can capture hits and misses of PV streamers but no false alarm forecasts or correct negatives.

3.2 PV streamer identification

To identify periods of significant ULDs a PV streamer identification algorithm from Wernli and Sprenger (2007) has been adapted. In a first step, the algorithm identifies a PVU contour. A second step checks for every pair of contour points whether the spherical distance between the two points d is smaller than a certain threshold D and whether the distance along the contour l is larger than a threshold value L (Figure 3.3). If both criteria are fulfilled the spherical line between the points and the PV contour line between the two points encircle the defined PV streamer (shaded area in Figure 3.3). Wernli and Sprenger (2007) used the 2PVU contour as the dynamical tropopause and $D = 800$ km and $L = 1500$ km as threshold values.

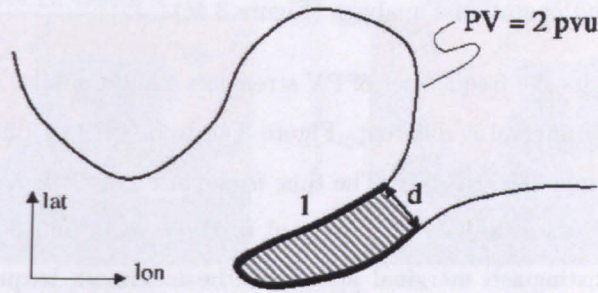


Figure 3.3: Schematic depiction of the streamer identification. The black line depicts a PV contour. The shaded area account for the identified streamer if the spherical distance d (line with arrows) between two points is smaller than the threshold D and l (black solid line) is larger then the threshold value L (taken from Wernli and Sprenger, 2007).

As discussed in Section 3.1 the absolute PV values from calculations with Equation 3.4 are smaller. Therefore different values for the PV contour, D and L were tested to detect the best combination for the identification of PV streamers from the available PV fields. Several sensitivity studies are performed: (i) calculating PV fields from ECMWF ERA-40 data as well as operational analysis and (ii) running the identification algorithm with different set-ups (PV-, D - and L -threshold values). Figure 3.4 summarises the results with a climatology result from Wernli and Sprenger (2007) (3.4a). They used the ECMWF ERA-15 data and the 2.0 PVU on 320 K as PV contour, $D = 800$ km and $L = 1500$ km as threshold values for the identification. Figure 3.4 b and c using the same D - and L -threshold values and a reduced PV value (1.5 PVU) due to the limitations explained above and ERA-40

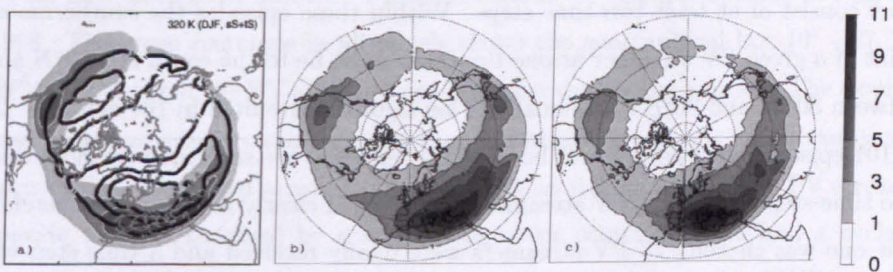


Figure 3.4: Winter mean (DJF) frequency in % (gray shading) of PV streamers on a) 320 K for the ERA-15 time period of 1979 - 1993 (taken from Wernli and Sprenger, 2007), b) 200 / 500 hPa - PV for the ERA-40 time period 1980 - 2001 and c) 200 / 500 hPa - PV for the operational analysis in the time period of available ensemble data 1996 - 2008.

(Figure 3.4b) and operational analyses (Figure 3.4c).

In all three results the frequencies of PV streamers exhibit similar structures even though the time interval is different. Figure 3.4a from 1979 to 1993, b from 1980 to 2001 and c from 1996 to 2008. The time frame of Figure 3.4c have been chosen due to the EPS data availability restricted to these years (cf. Section 2.1). All three figures distinguish marginal and show the maximum frequencies over the Mediterranean Sea and North America. The sensitivity study with changing set-ups exhibits a decreasing behaviour of frequencies with increasing PV-, D - and L - threshold values.

Therefore it can be stated: The best accordance to the results from Wernli and Sprenger (2007) showed the combination of 1.5 PVU as PV contour, $D = 800$ km and $L = 1500$ km.

3.3 Determination of PV streamer episodes

The adapted algorithm was applied to ECMWF operational analysis data from 1996 up to 2008 as seen in Figure 3.4c. The results are used for detecting suitable PV streamer episodes over northern Africa to study the EPS forecast performance for these cases. A tracking algorithm was created, which searches for a spatial overlap of PV streamers during consecutive 12 or 24 hour time steps. An episode must consist of at least two time steps. Within these episodes the southernmost point of a given PV streamer at one time step must be to the south of 27.5°N and between 30°W and 30°E meridionally. This algorithm resulted in 101 episodes. 26 of 101 episodes were sorted out, because two episodes are separated by more than two time steps without a PV streamer but belonged clearly together and therefore just one was chosen. 75 PV streamers were finally received and a time step was selected subjectively as verification time. The time step within the episodes chosen is usually the time step where the PV streamer has its southernmost extension. Other causes for the decision were highest intensity, largest extension or the highest impact of the PV streamer on weather, e.g. precipitation and or dust mobilization.

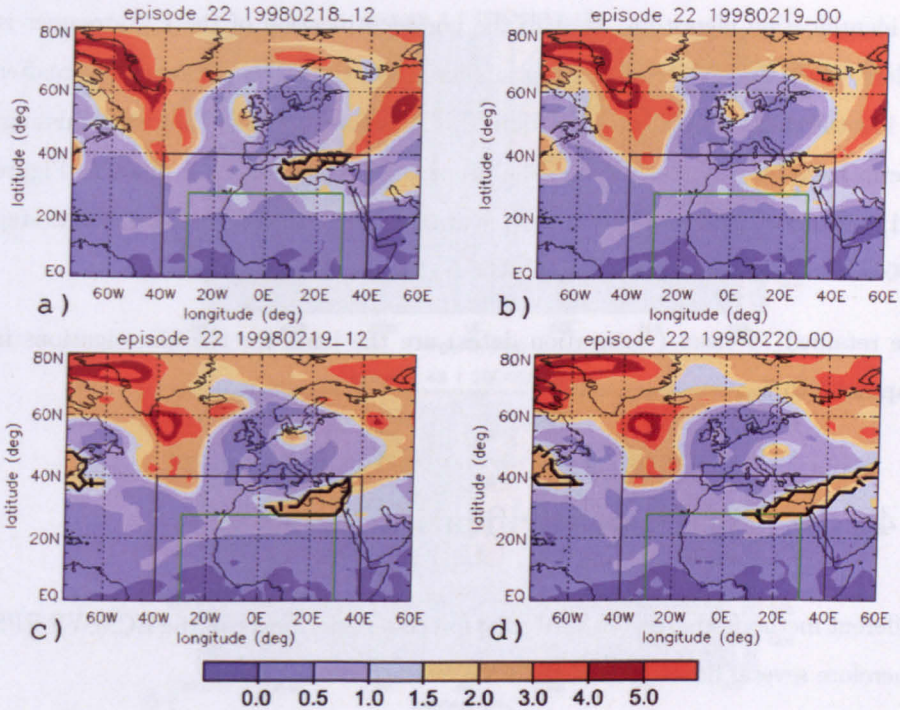


Figure 3.5: Example PV streamer episode from 1200 UTC 18 (a) to 0000 UTC 20 February 1998 (d). Black lines: Identified PV streamer contours, green rectangle: PV streamer need to occur within this area (0° - 27.5° N, 30° W - 30° E) during the episode, black rectangle: verification area (0° - 40° N, 40° W - 40° E) for investigations in Chapter 5, explained in Section 3.4.

Due to the fact that EPS forecasts were started only at 12 UTC until March 2003 (cf. 2.1), there is a technical limitation to 12 UTC as a chosen initial time step up to March 2003 even if the 00 UTC before or after the chosen 12 UTC PV streamer would have been more suitable. Figure 3.5 shows an example episode in February 1998. The green rectangle in all panels shows the geographical box (0° - 27.5° N, 30° W - 30° E) that the PV streamer need to enter during the episode. The example case describes several components of the algorithm and reasons for the subjective decision for a time step as verification time within the episodes. This PV streamer episode was characterised by a strong ridge over central Europe and a cyclonic wave breaking downstream. The PV streamer occurred from this RWB (marked as black line in Figure 3.5a, c, d) moved from the Mediterranean Sea (Figure 3.5a) into the African continent within the two days shown. As mentioned above the black contour line in Figure 3.5 marks the detection of a PV streamer from

the identification algorithm. In 3.4b the non-identification of the PV streamer is evident. Even the PV streamer looks similar to the time step before and thereafter the identification criteria are not fulfilled. Therefore the 'one time step missing' criteria have been implemented. The deepest PV intrusion took place in Figure 3.5d, but unfortunately this time step is at 0000 UTC. In conclusion the time step 1200 UTC 19 February 1998, Figure 3.5c is defined as verification date.

The retained 75 cases (verification dates) are the basis for the investigations in chapters 5 to 7.

3.4 Definition of verification areas

Different methods are used to verify the forecast performance of the ECMWF EPS. Therefore several boxes around the PV streamer are employed:

Firstly, a spatial box with borders 40°N - 0°S and 40°W - 40°E have been defined. This box covers a relatively large area over the eastern Atlantic and Northern Africa.

Additionally a verification is executed restricted to the area of the PV streamer ($\text{PV} > 1.5 \text{ PVU}$) within this box. This leads to a feature-based verification, which has some caveats who are discussed in Sections 5.2 and 8.4.2.

Due to the fact that the size of the PV streamer area differs between episodes, several approaches to define a box around the PV streamer of constant size are tested. This box is used, e.g. for the investigation 'ensemble correlation analysis' in Chapter 6. Hereafter three different approaches for defining a box are explained. For all attempts the northern and southern borders are set to 40°N and 25°N and a fixed east-west dimension of 25° is defined. The centre longitude can be located between 30°W - 30°E . Finally, the approach is taken where the box contains the maximum of streamer grid points. The algorithms tested will be explained below and are illustrated in Figure 3.6. Figure 3.6 shows three example verification dates with coloured rectangles emerging from the three different box methods.

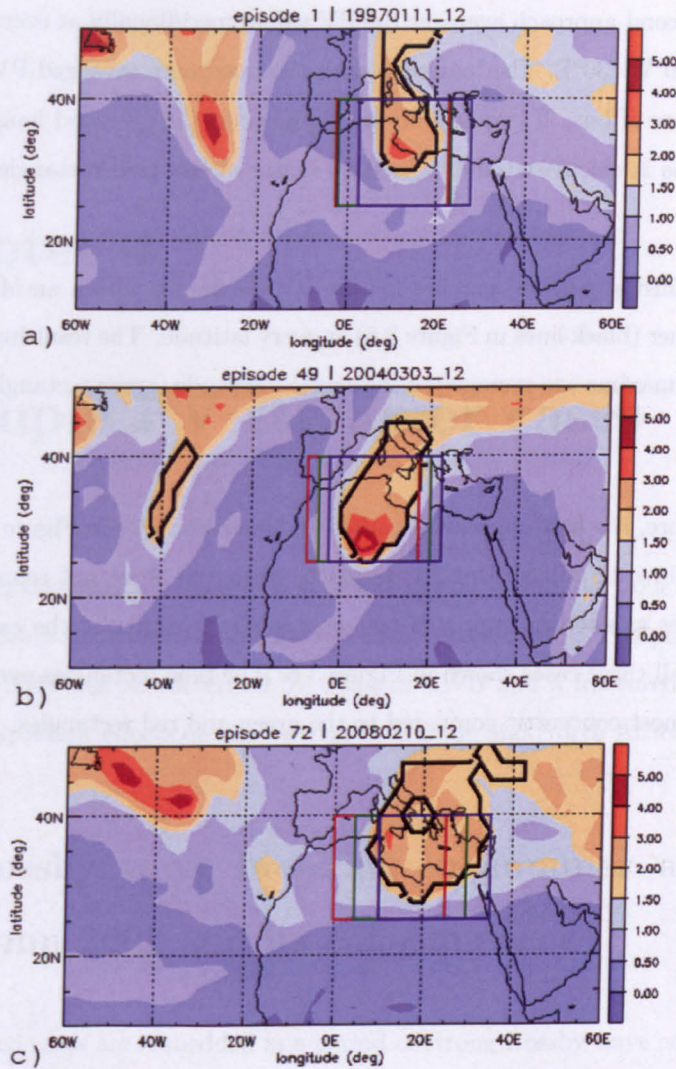


Figure 3.6: Three example of PV streamer verification dates. Coloured boxes are defined with different algorithms. For further investigations the blue rectangle is used (for details see text).

- For the first and definite approach taken, the box is shifted gradually from west to east and the number of grid points that belong to the PV streamer (marked by black contour lines in Figure 3.6) is counted. The box with most PV streamer grid points is taken (blue rectangles in Figure 3.6). If there are boxes with the same amount of grid points, the centre longitudes of these boxes are averaged.

- The second approach averages the PV values meridionally at every longitude from 30°W - 30°E. The longitude with the maximum averaged PV is defined as centre of box. If two or more maxima occur, the averaged longitude of all maxima is calculated and defined as centre of box (red rectangles in Figure 3.6).
- The third algorithm searches for the PV maximum within an identified PV streamer (black lines in Figure 3.6) at every latitude. The resulting longitudes of the maxima are averaged to the centre longitude (green rectangles in Figure 3.6).

As said before, the first approach, marked as blue rectangles in Figure 3.6 is taken for further investigations. Due to approaches two and three not representing the PV streamer as good as approach one does in the majority of the cases. This is evident in all three cases shown in Figure 3.6. The blue rectangles overlay the PV streamers most concentric compared to the green and red rectangles.

Chapter 4

Example PV streamer cases

This chapter discusses an active PV streamer period in summer 2008 to illustrate the atmospheric systems under study and their consequences. The period August to October 2008 was characterised by frequent RWB and a fractured jet stream. This had important effects on the weather in Europe and North Africa.

4.1 Rossby wave breaking in summer and autumn 2008 and its consequences

The presented cases are embedded in a period of strong Rossby wave activity from August until October 2008. During this episode several heavy precipitation events occurred over southern Europe and the northern part of Africa. In general, these three months in late summer 2008 caused wet conditions in Southern Europe and northern parts of Africa and drier conditions compared to the 30 year average in northern parts of Europe. (WMO Report, August 2008, September 2008, October 2008).

In Melilla situated in North Africa in the vicinity of the Mediterranean Sea, the precipitation amount reached 159 mm in September 2008 compared to 7 mm on average for the last 30 years. Ghardaia (Algeria) around 500 km inland in the

Sahara is another rain gauge that received ten times more rain than average in September 2008 (47 mm, 30 years average: 4 mm). (WMO Report, September 2008)

Most IMPETUS (An Integrated Approach to the Efficient Management of Scarce Water Resources in West Africa) precipitation stations recorded a lot more precipitation than usual. Some stations received around 80 mm instead of 2 mm on average over the whole three months period (personal communication with Prof. Dr. Andreas Fink, University of Cologne, October 2009).

The frequent PV streamers caused unusual precipitation amounts in southern and central Europe as well. For example Görlitz (Germany) had 95 mm in October instead of 45 mm on average and Murcia (Spain) received 107 mm in October 2008, and therefore 76 mm more than the 30 year average of 31 mm. (WMO Report, October 2008)

4.2 Precipitation pattern associated with PV streamer

The focus of this section is a selected PV streamer and the associated severe precipitation in Europe and Northwest Africa, illustrated in Figure 4.1. This PV streamer is studied in more detail and with focus on the diabatic influence on Rossby wave propagation and breaking in Grams et al. (2011). On 12 September the PV streamer (indicated by the green contour line in Figure 4.1a) was situated over the British Isles, France with its southern tip over northern Spain. The PV streamer originated from a PV reservoir connected to ex-hurricane *Hanna* which underwent extratropical transition (ET) at 0600 UTC 07 September 2008 (not shown). The cyclone evolved and deepened in the following days on its way east- and northwards supported by the PV streamer shown in Figure 4.1a in its early stages. At the time step shown in Figure 4.1a (00 UTC 12 September) the mean sea-level pressure contours (black lines) show no signs of a low pressure system on the east-side of the

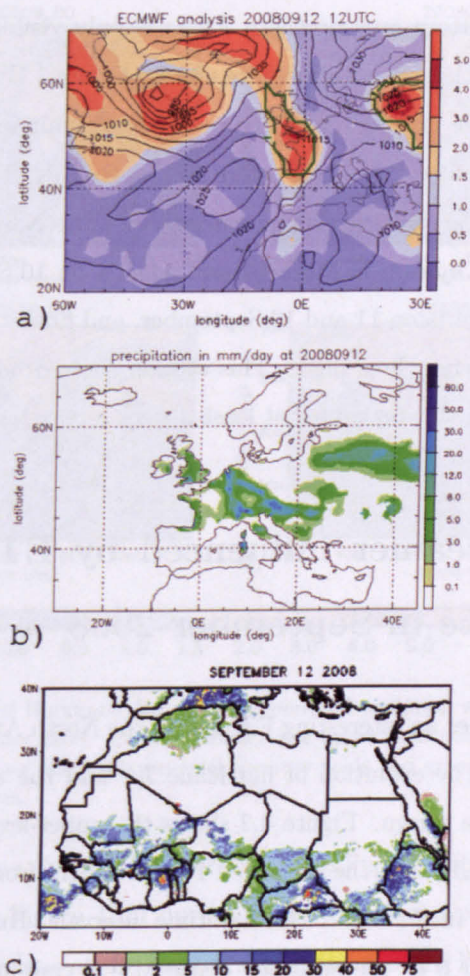


Figure 4.1: Synoptic situation on 12 September 2008: a) Upper-level PV in colours with black lines showing mean sea-level pressure. A green contour encircles the detected PV streamer. b) Precipitation amounts from ENSEMBLES E-OBS gridded rain gauge data over Europe (restricted to land) from 0600 UTC 12 to 0600 UTC 13 September 2008. c) TRMM satellite rain product over Northern Africa in mm from 0600 UTC 12 to 0600 UTC 13 September 2008.

PV streamer. The remnants of low "ex-Hanna" are visible over Iceland and are merged with another low pressure system. Nevertheless, the cold front of *Hanna* was still influencing the weather over Europe as evident in Figures 4.1b and c.

As shown in Figure 4.1b frontal rain occurred from Britain to the Balkans. Furthermore, thunderstorms in Northern Italy, the western Mediterranean and northern Africa were caused by the PV streamer, which generates an unstable troposphere by advecting cold air in higher altitudes over warm air in the lower troposphere.

The precipitation pattern over northern Africa is only visible in TRMM data in Figure 4.1c, because the precipitation data used in Figure 4.1b are restricted to European land. The time step chosen in Figure 4.1c shows rain in a wide area whereas the rain was more localised the days before and afterwards. The rain started three days before the date shown with thunderstorms over the Northern Morocco on 09 September, followed by rain in Morocco and Algeria on 10 September, continued further east over Algeria on 11 and 12 September, and finally with heavy rain over Tunisia in the following three days. This section showed how PV streamers can affect the weather in this region for at least a week.

4.3 PV streamer influenced by ET from hurricane *Ike* in September 2008

This section describes an interesting ET case in the North Atlantic during the late summer of 2008. The evolution of hurricane *Ike* and the associated upper-level development will be shown. Figure 4.2 shows the upper-level PV, the mean sea-level pressure (MSLP) and the identified PV streamers from 09 September until 19 September 2008 in three and four day time intervals. Hurricane *Ike* is evident in Figures 4.2a and b as the encircled dense MSLP contours less than 1000 hPa and marked with **A**. The storm system was situated over the Caribbean Islands on 09 September (Figure 4.2a). In the following days the system crossed the Gulf of Mexico northwestwards and underwent landfall in Texas at 0700 UTC 13 September (Figure 4.2b). After landfall its intensity decreased and its movement changed to northwest. An elongated PV streamer (see Figure 4.2b) over the western parts of the USA (subsequently western PV streamer and marked as **B** in Figure 4.2b) supported the northwestward flow by inducing southerly winds at its eastern side. The configuration with low PV between the western PV streamer (**B**) and the high PV values off the south coast of Greenland (marked as **C** in Figure 4.2b) intensified in the following days. The low-pressure system connected with the high PV values over Iceland (marked as **D** in Figure 4.2b) caught up the remnants

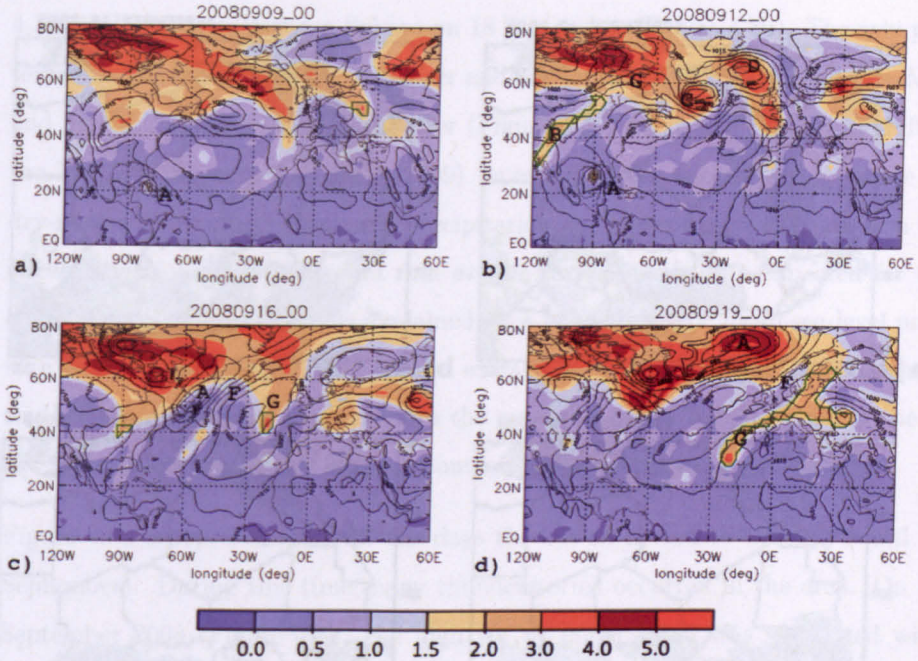


Figure 4.2: Influence of Hurricane *Ike* on the upper-level evolution at 00 UTC a) 09, b) 12, c) 16 and d) 18 September 2008. Colours indicate the upper level potential vorticity in PVU units. Black contours show the mean sea-level pressure fields and green dashed contours mark the detected PV streamers.

of ex-hurricane *Hanna* (low MSLP over Iceland in Figure 4.2b). *Ike* underwent an ET (marked as **A** in Figure 4.2c) during its northward movement and continued as an extratropical cyclone at the eastern side of the western PV streamer (**B**). *Ike* advected a lot of warm subtropical air into high latitudes and in consequence the PV ridge (low PV values) intensified. Until 16 September the northern border of the ridge (marked as **F** in Figure 4.2c) was stationary at 60°N but on 17 September the ridge started to spread northward (not shown). The Rossby wave amplitude increased and a negative wave breaking occurred, originating from the intensified ridge. Downstream of the ridge a positive wave breaking occurred. In Figure 4.2d the negative wave breaking is recognisable as a northward shift of low PV values, marked as **F**. The green line surrounds the downstream PV streamer identified with the algorithm explained in Section 3.2 and is marked as **G**. The PV streamer developed from high value PV over the Gulf of St. Lawrence and the PV reservoir over northeast Canada (marked as **G** in Figures 4.2b, c and d). The PV streamer

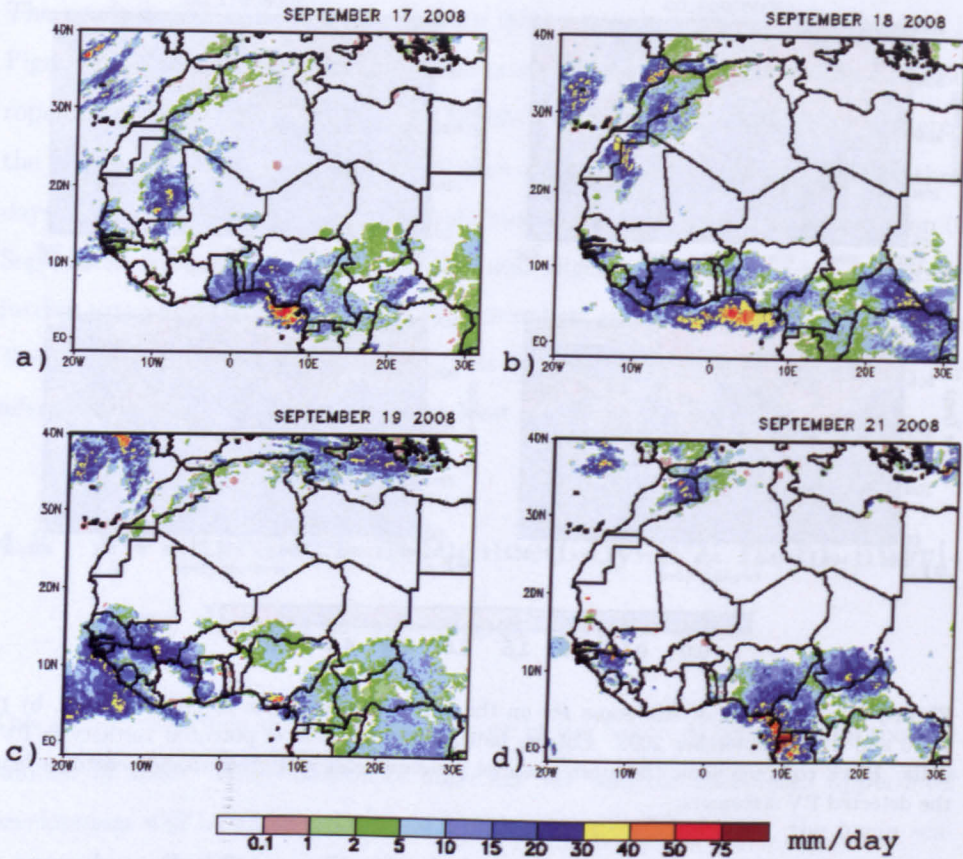


Figure 4.3: Precipitation amounts from TRMM satellite rain product over Northern Africa on a) 17, b) 18, c) 19 and d) 21 September 2008.

emerged and elongated between 14 and 19 September and reached his southernmost extension, south of 30°N, at 0000 UTC 19 September 2008. Finally, a cut-off formed on 21 September.

From 17 to 24 September the high PV system situated offshore Spain and northwest Africa was associated with a significant amount of precipitation (up to 60mm/day) in southern Spain, northern Algeria and Morocco.

Figure 4.3 shows the rainfall over northern Africa for four days when the PV streamer was situated off the African coast. Later on, the streamer cut off and moved eastward along the northern coast of Africa. Notable are the large precipitation amounts caused by thunderstorms over Mauritania on 17 September (Figure

4.3a) and Morocco/Western Sahara on 18 September (Figure 4.3b). The rain patterns over Mauritania on 17 September and particularly over Senegal, western Mali and northern Guinea on 19 September (Figure 4.3c) point to a northward shift of the ITCZ. Knippertz and Fink (2009) investigated the subtropical influence on dry-season (November - February) precipitation and showed a clear connection between extratropical troughs and rain events further north than expected for the dry-season. The mechanism is explained by a lowering of the mean sea-level pressure over the Sahara initiated by the extratropical disturbances. Subsequently, southerly winds advect moist air into the western African region, which is one of the triggers and necessities for deep convection.

Figure 4.3d is representative for the days the cut-off moved to the east (until 25 September). During this time many thunderstorms occurred in the area. On 21 September 2008 (Figure 4.3d) the high PV at upper levels was associated with heavy precipitation in northern Morocco at the border to Algeria. From the end of September until the beginning of October 2008 remnants of high PV remained over the northern coast of Africa, which supported deep convection. Among other severe weather events, these thunderstorms resulted in a flood in Ghardaia (Algeria) on 02 October 2008. The flooding killed over 30 people and left around 1000 people homeless (International Federation of Red Cross and Red Crescent Societies, 2008)

Blank Page

Chapter 5

Statistical analysis

This chapter focuses on the forecast performance of the ECMWF EPS system for the PV streamer cases identified in Chapter 3. In the first section the distribution of the PV streamers per year, month and longitude are presented. The following sections concentrate on the verification of one to ten day forecasts with a focus on the overall dispersive behaviour, forecast histograms and an investigation of the displacement error.

5.1 PV streamer climatology

As described in Chapter 3 the PV streamer identification resulted in 75 cases as a basis for this analysis. Figure 5.1 shows the interannual distribution of the cases for the years 1996 to 2008.

The fewest cases of low-latitude PV streamers occurred in 2000, 2003 and 2004 with only four cases. The maximum number of nine cases occurred in 1999 and 2008. The annual average over these twelve years is 6.25 PV streamers a year. Overall the histogram shows more frequent PV streamers occurring in the years at the beginning of the investigation period, with a decrease of occurrences for the years thereafter and a slight increase up to the end of the period.

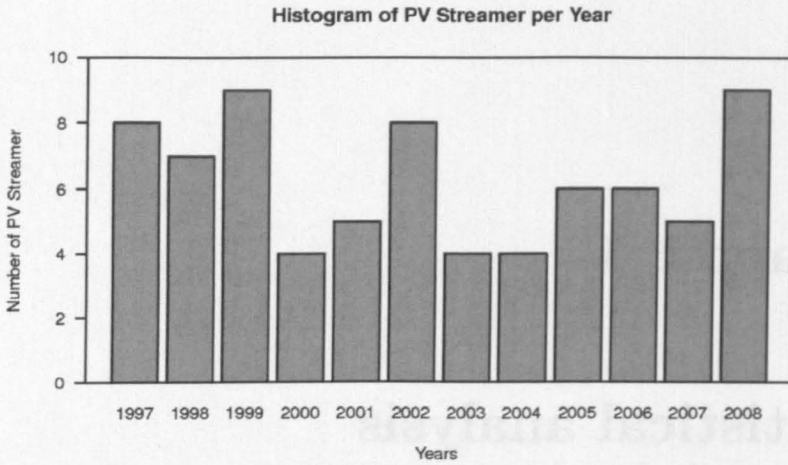


Figure 5.1: Number of PV streamers per year identified in ECMWF operational analysis data. Identification of the PV streamers described in detail in Chapter 3.

Figure 5.2 shows the monthly distribution of the 75 PV streamer cases. Activity is confined to boreal winter and spring from November to April. From May to October, no low-latitude PV streamer episodes were identified using the identification and filtering algorithms explained in Chapter 3. The maximum frequency occurred in January and February with an average of 2 (1.6) PV streamers per year in January (February). The seasonal variability is mainly due to the seasonal cycle of temperature in the extratropics and the associated shift of the tropopause, and consequently the North Atlantic storm track. This distribution is consistent with

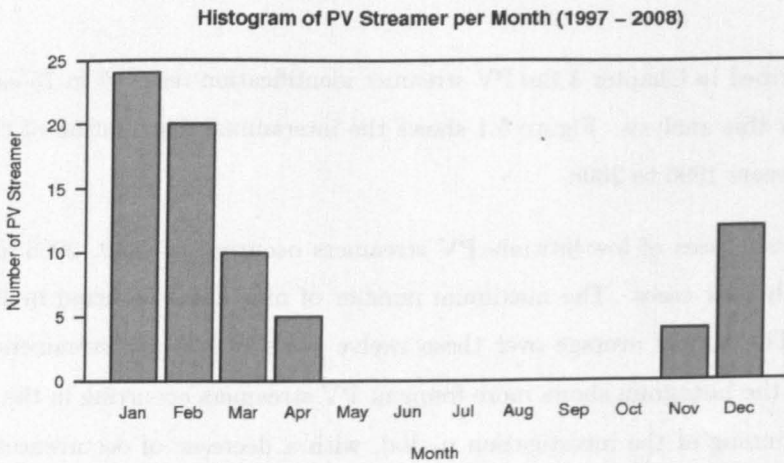


Figure 5.2: Number of PV streamers per month identified in ECMWF operational analysis data. Identification of the PV streamers described in detail in Chapter 3.

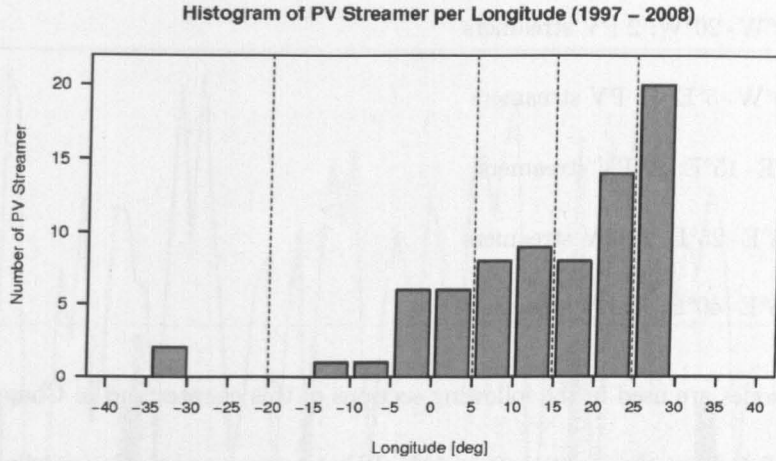


Figure 5.3: Number of PV Streamers per longitude in 5° steps from 40°W - 40°E as identified in ECMWF operational analysis data. Identification of the PV streamers described in detail in Chapter 3. Dashed lines are the divide of the five longitudinal zones, see details in text.

various other studies as described in Section 1.2.1.1.

As described in Section 3.4 a central longitude has been defined for each PV streamer. Figure 5.3 shows the distribution for all 75 PV streamer cases in 5° longitudinal steps. The histogram shows a clear increase from west to east. The maximum is found between 25°E and 30°E with 20 cases over the twelve years examined in this study. This longitude region is mainly located over the western half of Egypt. The Libyan-Egyptian border roughly runs along the 25°E meridian. Together with the second most frequent longitudinal region (20°E to 25°E), which has 14 cases, nearly half of all PV streamers under study are placed within this 10° longitudinal zone. The rest of the cases, except for two outliers, are identified between the west coast of Morocco ($\sim 15^\circ\text{W}$) and the Gulf of Sidra (20°E). Within this area, only two PV streamers were identified at the western edge over Morocco. The majority lie between 5°W (east of the Strait of Gibraltar) and 20°E . The two outliers over the Atlantic are both located at $\sim 30^\circ\text{W}$.

Five longitudinal zones are defined for further investigations that contain similar amounts of PV streamers, with the exception of the two PV streamers over the ocean. The dividing lines are shown as dashed lines in Figure 5.3.

- 40°W - 20°W: 2 PV streamers
- 20°W - 5°E: 14 PV streamers
- 5°E - 15°E: 17 PV streamers
- 15°E - 25°E: 22 PV streamers
- 25°E - 40°E: 20 PV streamers

These zones are used in the following sections of this chapter and in Chapter 6.

Figure 5.4 shows the exact timing of the PV streamers and the longitudinal zones as colours. Overall, it can be said that the distribution per month is well balanced, with most individual months having one or two PV streamers. However, some months show maxima and minima. The minima are often characterised by consecutive months without any PV streamer. Two months have four PV streamers. The first, January 1999 contains three PV streamers from the longitudinal zone 5°E - 15°E, mainly over Tunisia and Libya. The other maximum occurred in January 2006 with two PV streamers between 15°E - 25°E.

The longest time period without PV streamers took place between March 2000 and February 2001 followed by only two PV streamers in March and April 2001. The other minima occurred at the end of a winter (March/April) together with the beginning of the next winter season (November/December). In 2003, the minimum lasted four months, whilst in 2006 and 2007 minima of three months occurred and in three years (1997, 2004, 2005) minima of two months occurred.

Examining the repeated appearance of PV streamers in one longitudinal zone within a short time period, it becomes evident that half of the PV streamers in 15°E - 25°E (blue, eleven out of 22) occurred from 1997 to the end of winter 1998/1999. The same behaviour exists for the easternmost zone (black), where ten out of 20 PV streamers happened in the last three years (2006 - 2008). Nearly half of the PV streamers (six out of 14) from the longitudinal zone 20°W - 5°E occurred in two consecutive winters (2004/2005 and 2005/2006). These accumulations suggest a clustering of PV streamer evolution for every longitudinal zone. Therefore,

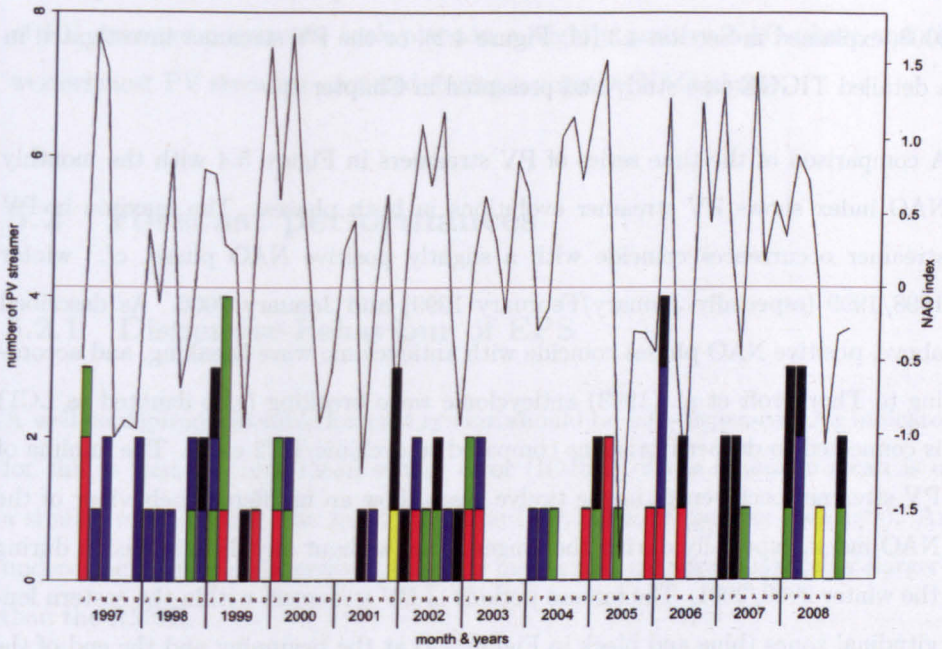


Figure 5.4: Time series of PV Streamers for every January (J), February (F), March (M), April (A), November (N) and December (D) from 1997 to 2008. Colours depict the different longitude sections defined in Section 5.1 from Figure 5.3: yellow = $40^{\circ}\text{W}-20^{\circ}\text{W}$, red = $20^{\circ}\text{W}-5^{\circ}\text{E}$, green = $5^{\circ}\text{E}-15^{\circ}\text{E}$, blue = $15^{\circ}\text{E}-25^{\circ}\text{E}$, black = $25^{\circ}\text{E}-40^{\circ}\text{E}$. The monthly mean NAO index is shown as black line.

it might be possible that different evolutions prefer different atmospheric structures or regimes. This aspect will be investigated further in the following sections and chapters.

The NAO index is an indicator of the large-scale regime over the North Atlantic and Europe. The monthly mean NAO index is shown in Figure 5.4 as a black line. Benedict et al. (2004) discovered the importance of Rossby wave breaking for the initiation and maintenance of different NAO phases. The negative phase is supported by strong cyclonic wave breaking over the central North Atlantic, which leads to a high amplitude ridge over Iceland. Pronounced PV streamers initiated by anticyclonic wave breaking over western North America and the North Atlantic are crucial for the positive NAO phase. Both phases can potentially lead to deep PV streamer intrusions into the Tropics. The negative phase, with the pronounced ridge over Iceland, can support a PV streamer downstream. Examples

of this evolution include the PV streamer influenced by hurricane *Ike* in September 2008, explained in Section 4.3 (cf. Figure 4.2), or the PV streamer investigated in a detailed TIGGE case study and presented in Chapter 8.

A comparison of the time series of PV streamers in Figure 5.4 with the monthly NAO index shows PV streamer evolutions in both phases. The maxima in PV streamer occurrences coincide with a slightly positive NAO phase, cf. winter 1998/1999 (especially January/February 1999) and January 2006. As described above, positive NAO phases coincide with anticyclonic wave breaking, and according to Thorncroft et al. (1993) anticyclonic wave breaking (also denoted as LC1) is connected to deeper intrusions compared to cyclonic/LC2 cases. The minima of PV streamer occurrences in the twelve years show an indifferent behaviour of the NAO index, especially during the longest time without any deep intrusion during the winter 2000/2001. The intense periods of PV streamers within the eastern longitudinal zones (blue and black in Figure 5.4) at the beginning and the end of the time series are marked by a slightly positive NAO phase as well. In contrast, high positive NAO values do not necessarily imply high frequencies of PV streamers.

The detailed look into the negative NAO phase, which according to Hurrell (1995) leads to wet conditions in Southern Europe and Northern Africa, shows an inconclusive behaviours as well. Overall the negative NAO phase does not coincide with high PV streamer frequencies. However an exception to this occurred in December 2001 where three PV streamers were observed, one of which is one of the only two western PV streamers in the time series. The second in this longitudinal zone (around 30°W) happened in April 2008, also in a negative phase. As mentioned above, the negative phase is marked by cyclonic wave breaking over the North Atlantic and a ridge building over Iceland. According to Thorncroft et al. (1993) this LC2 evolution leads to a cyclonic roll-up of the PV streamer downstream. However, it cannot be concluded that the negative phase supports only the western PV streamers. Most of the strong negative phases (e.g. April 1999, March and December 2001, December 2002, March 2006) coincide with PV streamers from the easternmost longitudinal zone.

It can be concluded that PV streamers occur in both NAO phases. The maxima of PV streamer occurrence took place in a slightly positive NAO phase and the westernmost PV streamer occurred during a negative NAO phase.

5.2 Forecast performances

5.2.1 Dispersive behaviour of EPS

A well-configured ensemble forecast system should be non-dispersive. An indicator for this is that the root mean square error (RMSE) of the ensemble mean is of a similar magnitude to the spread (standard deviation of member forecasts). An underdispersive (overdispersive) behaviour means that the spread is smaller (larger) than the RMSE.

The ensemble system behaviour, averaged over all 75 PV streamer cases, is shown in Figure 5.5. Figure 5.5 a shows a comparison of RMSE and spread calculated from PV in two different areas. The red lines depict the calculations inside the box $40^{\circ}\text{N}-0^{\circ}\text{S}$, $40^{\circ}\text{W}-40^{\circ}\text{E}$ and the black lines just the area of the PV streamer ($\text{PV} > 1.5 \text{ PVU}$) within this box. The red lines in Figure 5.5 b are the same as in Figure 5.5 a, but note the different limits of the axis. The blue lines in Figure 5.5 b show the RMSE and spread calculated with the atmospheric variable geopotential height at 500 hPa within the same $40^{\circ}\text{N}-0^{\circ}\text{S}$, $40^{\circ}\text{W}-40^{\circ}\text{E}$ box. In all three approaches the RMSE and spread grows with lead time as expected. The overall behaviour is strongly underdispersive, independent of which variable or box is used.

In Figure 5.5 a the values of the black lines are nearly twice as large as those of the red lines. A climatological PV distribution in the northern hemisphere shows that most of the area south of 40°N (northern border of the box) has small PV values. Therefore, for grid points away from the PV streamer the differences between the forecast and the analysis are small independent of the quality of the forecast. This leads to small RMSE and spread values, and hence a smaller RMSE

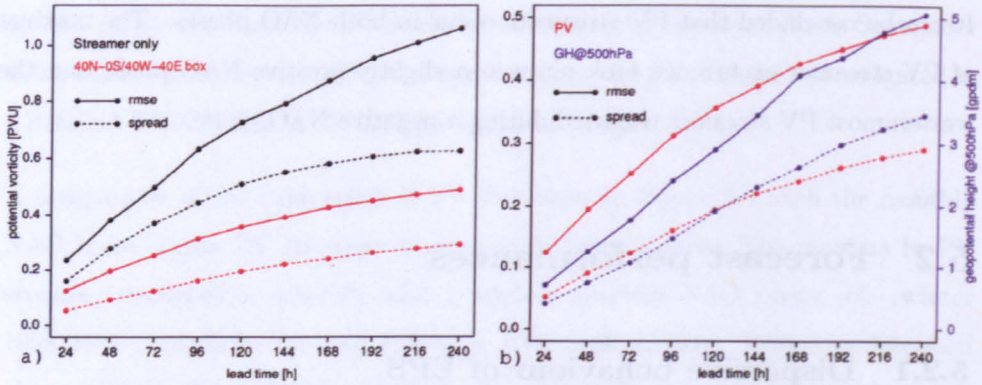


Figure 5.5: Comparison of RMSE (solid line) and spread (dashed line) for the 1- to 10-day ECMWF ensemble forecasts. RMSE and spread were averaged over 75 PV streamer cases and calculated for the PV in a box $40^{\circ}\text{N}-0^{\circ}\text{S}$, $40^{\circ}\text{W}-40^{\circ}\text{E}$ (red lines in a and b), PV restricted to the PV streamer area within the box (black line in a) and geopotential height at 500 hPa in the whole box (blue line in b).

and spread when averaged over the whole box than those which are restricted to the PV streamer area within the box.

Most studies, which investigate the dispersive behaviour of one EPS or comparisons between ensemble systems from different centres, use geopotential height at 500 hPa and the whole northern hemisphere as a basis for their calculations, see e.g. Buizza et al. (2005). In order to compare these studies with the PV forecast errors, Figure 5.5 shows RMSE and spread for PV and geopotential height at 500 hPa. It is evident that both lines have very similar shape and slope. For small lead times (24h-144h) the gap between the geopotential height RMSEs and spread is slightly smaller compared to the PV RMSEs and spread. A possible explanation might be the smoother field of geopotential height compared to PV. Especially in the synoptic situations under study, where the gradients in the PV fields are strong at the edges of PV streamers. In consequence slightly wrong PV forecasts can cause higher RMSEs than in the forecasts in geopotential height. For longer lead times stronger deviations of forecast and analysis lead to RMSEs of the same range.

The next paragraphs focus on a detailed investigation of the results for RMSE and spread with respect to the temporal (annual, model changes in EPS) and spatial distributions of PV streamers. Figure 5.6 shows the error calculations divided into

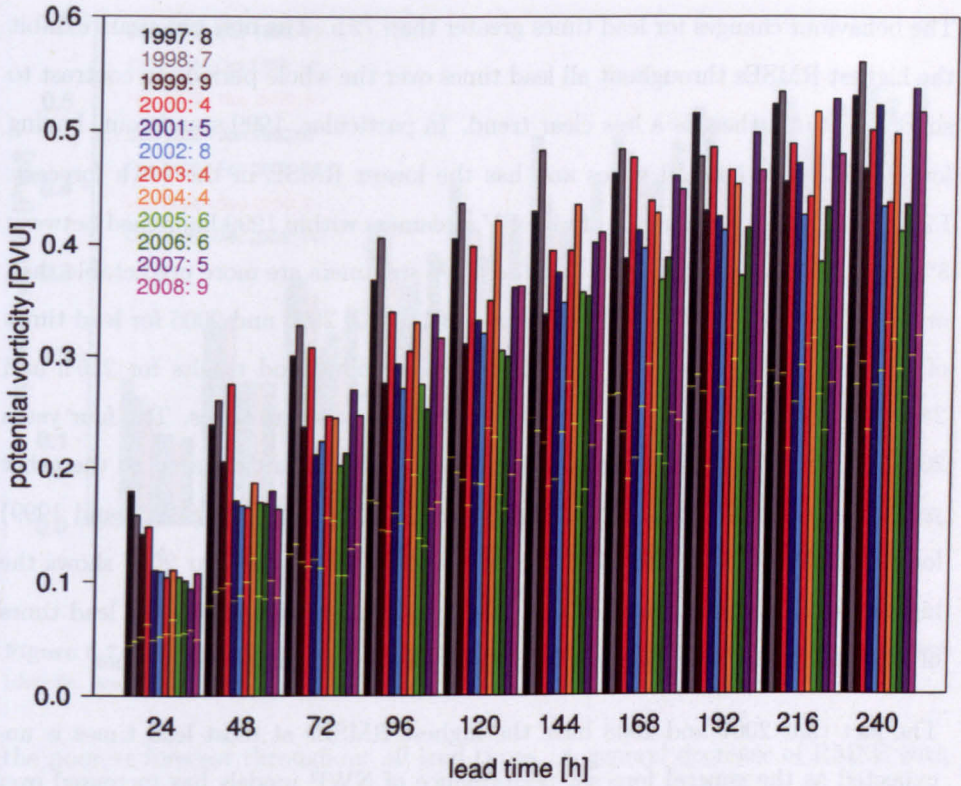


Figure 5.6: Comparison of RMSE (bars) and spread (yellow lines) for the 1- to 10-day ECMWF ensemble forecasts separated into yearly sections. Numbers of PV streamers per year are given in the legend. RMSE and spread were averaged over all PV streamer cases per year and calculated for PV in the box $40^{\circ}\text{N} - 0^{\circ}\text{S}$, $40^{\circ}\text{W} - 40^{\circ}\text{E}$.

years. As shown in Figure 5.1, the number of PV streamers ranges between four (2000, 2003, 2004) and nine cases (1999, 2008) per year. Owing to the small number of cases in some years, a statistically robust statement cannot be made, as single outlier forecasts can influence the results strongly.

In general, the RMSE decreases over the years for small lead times (24-48h), with the first four years (1997-2000) exhibiting around 50% higher RMSEs than the years thereafter. From 2001 to 2008 the RMSEs are in the same range. Interestingly, the spread does not change dramatically over the years for these two lead times. This leads to an improvement of the EPS by decreasing the RMSE with a simultaneous increase/non-change in the spread. Hence, the EPS became less underdispersive over the years for small lead times.

The behaviour changes for lead times greater than 72 h. The first two years exhibit the highest RMSEs throughout all lead times over the whole period. In contrast to short lead times there is a less clear trend. In particular, 1999 stands out, having low RMSEs over all lead times and has the lowest RMSE in the 144 h forecast. Figure 5.4 shows that four out of nine PV streamers within 1999 happened between 5°E- 15°E. It might be the case that these PV streamers are more predictable than others. Other years with low RMSEs are 2001, 2002, 2005 and 2006 for lead times of 72 h to 192 h, whereas all four, except 2001, show good results for 216 h and 240 h. The RMSE increases in 2001 for the two longest lead times. The four years 2003, 2004, 2007 and 2008 show higher RMSEs after 48 h compared to the other years. 2004 stands out as having the highest RMSEs (excluding 1998 and 1999) for lead times of 120 h and 144 h. For longer lead times, the year 2007 shows the highest RMSEs. In contrast to 2004, 2003 has its maximum RMSE for lead times of 168 h to 192 h with a decrease in RMSEs for the two longest lead times.

The fact that 2007 and 2008 have the highest RMSEs at most lead times is unexpected as the general forecast performance of NWP models has increased over the last decades. However as mentioned before, the studied low number of PV streamers going into the calculations is problematic.

The spread behaviour over the years and lead times should be interpreted relative to the RMSE evolution. In other words, the RMSE increases over the years and the spread increases as well. The gap, however, between both values becomes larger with increasing lead time, consistent with Figure 5.5 for all PV streamers. The spread follows the RMSE forecast performances in every year, with the smallest (highest) spread values coincide with the minima (maxima) in RMSEs.

Figure 5.7 shows RMSE and spread calculations separated by dates when the EPS changed (see Table 2.1 in Section 2.1). The legend shows how many PV streamers were identified in each period.

To first order, the RMSE results for short lead times (24 h to 72 h) show similar results compared to Figure 5.6, with higher RMSEs in the early years up to the change in November 2000. The first period (January 1997 to March 1998), remains

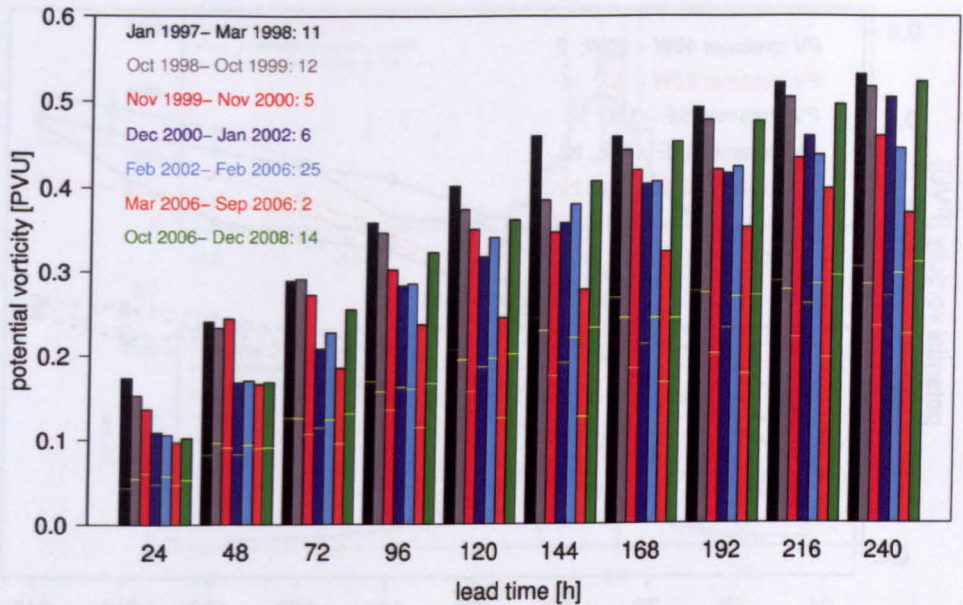


Figure 5.7: Same as Figure 5.6. Separated into temporal sections based on EPS changes in time (details: see Table 2.1).

the poorest forecast throughout all lead times. A general decrease of RMSE with model change is evident, except for an increase of RMSE after the last change in October 2006. In 2006 the VAREPS technique has been implemented. It might be that this technique leads to poorer PV streamer forecasts. Buizza et al. (2006) stated that the implementation of VAREPS aims to provide better predictions of small-scale, severe-weather events in the early forecast range. The results found in Figure 5.7 cannot support an improvement but rather imply a deterioration.

The best RMSEs for all lead times are found from March to September 2006, however, there are only two PV streamers in this period. The behaviour of the spread is slightly different to that observed in Figure 5.6. In general, the underdispersive behaviour is evident, however some model changes increased the spread, whilst the RMSE remained constant or decreased slightly. Examples of this behaviour are the first two changes with a lead time of 24 h and the changes in November 2000 and January 2002, where the longer lead times in particular show a dramatic increase in spread with a nearly constant RMSE. In November 2000, the model resolution

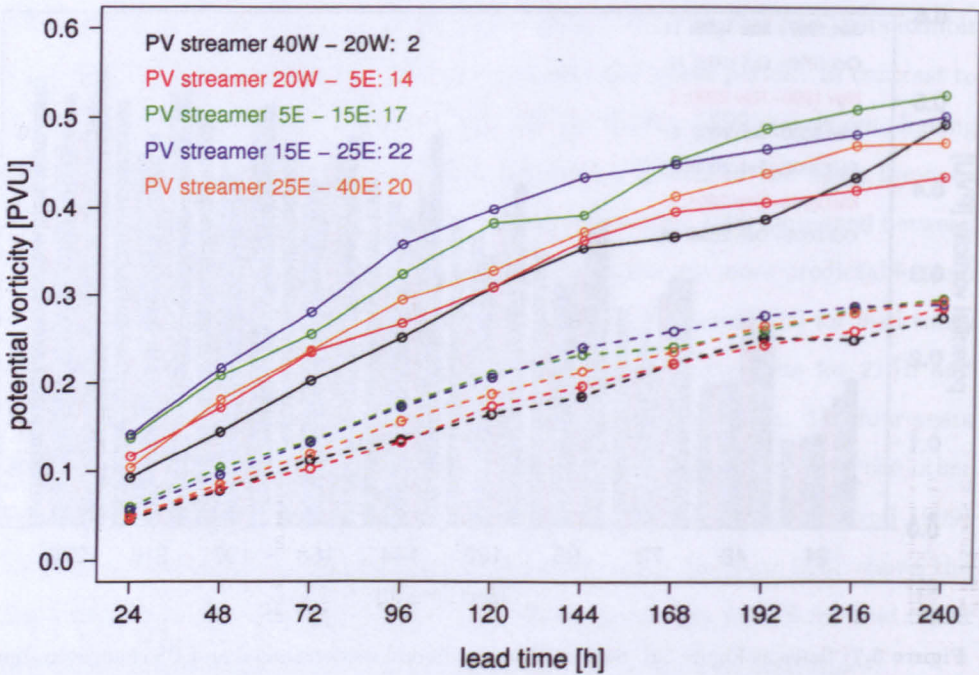


Figure 5.8: Comparison of RMSE (solid line) and spread (dashed line) for the 1- to 10-day ECMWF ensemble forecasts separated in longitudinal sections (details in Section 5.1). Number of PV streamers per section are given in the legend. RMSE and spread were averaged over all PV streamer cases and calculated for PV in the box 40°N - 0°S , 40°W - 40°E .

was increased from TL159 to TL255 and in January 2002 the Tropic SVs were implemented. Both changes proved their value by increasing the spread for the cases under study.

The comparison of RMSE and spread in Figure 5.8 is divided into longitudinal sections as defined in Section 5.1. The legend gives the number of PV streamers per longitudinal zone.

Not surprisingly, the underdispersive behaviour of the EPS is apparent in all geographical regions. In general, the shape and slope of the spread curves coincide with those of all five RMSE curves. The two 10° -longitudinal bands from 5°E - 25°E generally show the highest RMSEs. Both are equal for short lead times (24 h and 48 h), for longer lead times from 72 h to 144 h the more eastern zone (15°E - 25°E) has higher RMSE values whereas for lead times longer than 192 h the 5°E - 15°E

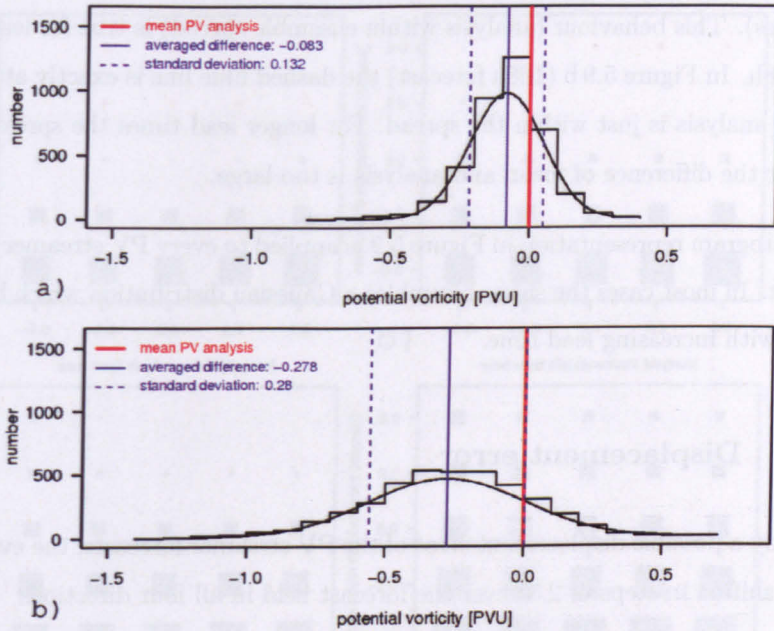


Figure 5.9: Difference between forecast (a) 72h and b) 168h) and analysed PV. PV values are a box average and all 75 PV streamer forecasts are included (see text for details).

zone has higher RMSEs. Smaller RMSEs are found for the more western areas, with higher RMSE values observed over the easternmost zone (25°E-40°E).

5.2.2 Forecast histograms

As described in Section 3.4, a box has been defined around each PV streamer, this will be used for further investigations into position and amplitude errors.

In Figure 5.9 the distribution (black line) of the differences between forecast and analysed PV in the box are shown. The box averaged PV over all 75 PV streamer cases in the analyses is 1.514 PVU. The solid blue line marks the mean difference between the 72h (Figure 5.9 a) and the 168h (Figure 5.9 b) forecast and the analysis. The dashed blue lines depict the ensemble spread.

The difference between the forecast and the analysis is negative for every forecast step (lead time 24h-240h) and increases with increasing lead time. As can be seen in Figure 5.9a, the mean analysis lies within the ensemble spread (dashed

blue lines). This behaviour (analysis within ensemble spread) is true for lead times 24h - 168h. In Figure 5.9 b (168h forecast) the dashed blue line is exactly at 0 PVU, i.e. the analysis is just within the spread. For longer lead times the spread is too small or the difference of mean and analysis is too large.

The histogram representation in Figure 5.9 is applied to every PV streamer episode forecast. In most cases the shape resembles a Gaussian distribution which becomes flatter with increasing lead time.

5.2.3 Displacement error

To study a possible displacement error of the PV streamer forecasts, the evaluation box is shifted in steps of 2.5° over the forecast field in all four directions

Figure 5.10 shows the different behaviour for several lead times. Red (blue) squares stand for higher (lower) averaged PV values inside the shifted box than in the analysis. The PV streamer is correctly predicted in terms of PV within the box if there is no square. The squares in the middle of each plot show the result without any shifting. They grow with lead time, reflecting the increase of the difference between forecast and analysed PV in the objective boxes containing every PV streamer, consistent with Figure 5.9.

The smallest square in the 24 h forecast is in the middle (Figure 5.10a) implying accuracy in position and amplitude. The 96 h forecast (Figure 5.10b) shows smaller differences if the box is shifted to the north and slightly to the east, indicating too weak penetration of the PV streamer into low latitudes. This behaviour continues with lead times up to 144 h (Figure 5.10c), with differences close to 0 PVU (small square) for NE shifts. Therefore, the displacements with the best results are migrating northeastwards with increasing lead time. For lead times greater than 168 h, the forecast PV values are too small everywhere, but again the smallest differences are found in the northeast.

Beside the calculation of the displacement error for all 75 PV streamer, the analysis was examined, divided into longitudinal zones (introduced in Section 5.1). The

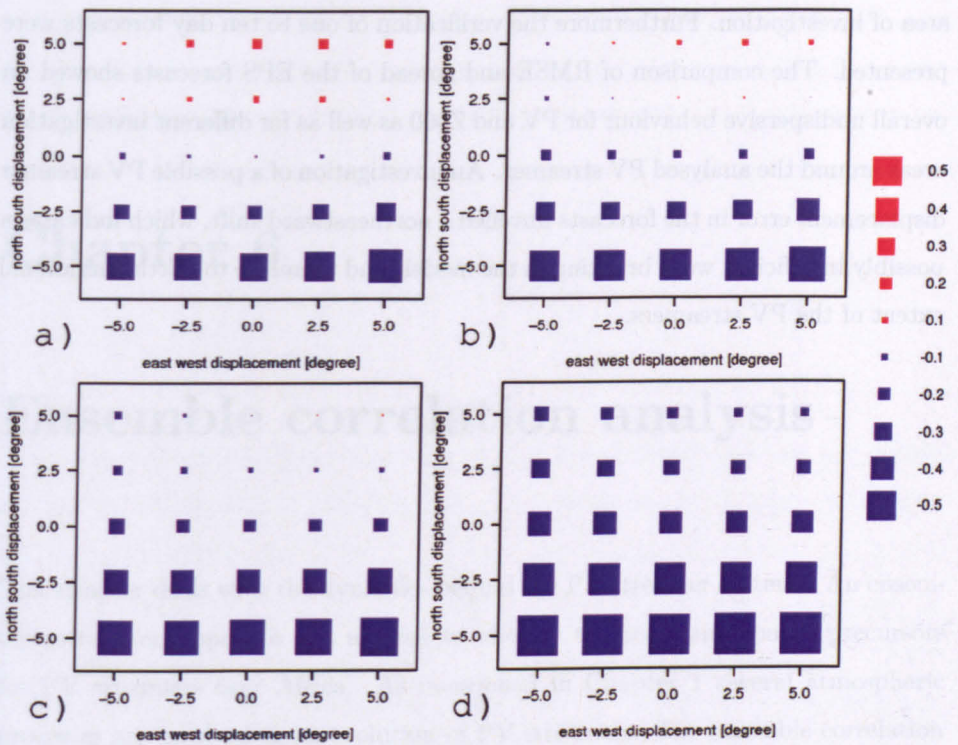


Figure 5.10: Difference between box averaged PV of displaced forecast and steady spatially analysed PV for 75 PV streamer events. The figures show the results for the a) 24 h, b) 96 h, c) 144 h and d) 216 h forecasts.

outcomes reflect the results presented above and can be seen in Figures A.1 to A.5 in Appendix A.

This indicates that PV streamer development stops too far north in most forecasts, possibly due to insufficient wave breaking and therefore too little meridional extension.

Concluding remarks

The past chapter examined the forecast performance of the ECMWF EPS for 75 PV streamer cases. The distributions of the PV streamers per year, month and longitude were shown with more regular distribution over the 12 years (1997 - 2008) and with maxima in boreal winter and to the east of the 30°W to 30°E restricted

area of investigation. Furthermore the verification of one to ten day forecasts were presented. The comparison of RMSE and spread of the EPS forecasts showed an overall undispersive behaviour for PV and Z500 as well as for different investigation areas around the analysed PV streamer. An investigation of a possible PV streamer displacement error in the forecasts unveiled a northeastward shift, which indicates a possibly insufficient wave breaking in the models and therefore too little meridional extent of the PV streamers.

Chapter 6

Ensemble correlation analysis

This chapter deals with the dynamics behind the PV streamer systems. An ensemble correlation approach was applied to identify temporal and spatial precursors for PV streamers over Africa. As mentioned in Chapter 1 several atmospheric processes are involved in an evolution of PV streamers. The ensemble correlation allows a detailed look into the forecasts and this technique can give indications, which processes lead to a strong/weak PV streamer. From studies in the past the following research questions regarding a strong/weak PV streamer forecast arise:

- Is blocking downstream important?
- Does diabatic heating upstream occur several days before the PV streamer reaches the low latitudes?
- Does ridge building up- and/or downstream amplify the Rossby wave in early stages of the forecast?

6.1 Introduction and method

The ensemble correlation method is adapted from Hawblitzel et al. (2007) who used correlations between different forecast variables to investigate precursors for

successful forecasts of convective systems. Here, the correlation between different forecast variables is investigated to find out which precursors several days before the PV streamer event are important for an (un)successful forecast. The linear correlation coefficient r is calculated using

$$r(x_{i,j}^t, PV_{box}^{168h}) = \frac{\frac{1}{N-1} \sum_{n=1}^N ({}^n x_{i,j}^t - \overline{x_{i,j}^t}) ({}^n PV_{box}^{168h} - \overline{PV_{box}^{168h}})}{\left[\frac{1}{N-1} \sum_{n=1}^N ({}^n x_{i,j}^t - \overline{x_{i,j}^t})^2 \right]^{\frac{1}{2}} \left[\frac{1}{N-1} \sum_{n=1}^N ({}^n PV_{box}^{168h} - \overline{PV_{box}^{168h}})^2 \right]^{\frac{1}{2}}} \quad (6.1)$$

The variable ${}^n PV_{box}^{168h}$ is taken from the 168 hour member forecasts of the PV field. For every single member n of all $N=50$ EPS members, a *box* average is calculated. The box is defined objectively over the PV streamer at verification time, as described in Section 3.4. The box-averaged PV for every member is correlated with the forecast $x_{i,j}^t$ of an atmospheric variable x at every grid point i, j for the same member several days before verification time (t =forecast step). Both forecasts (x and PV) are started from the same analysis time and the verification time equal to the 168 h forecast. Equation 6.2 shows an example of Equation 6.1.

$${}^{Z200} r_{i,j}^{48h} = \sum_{n=1}^{50} ({}^n Z200_{i,j}^{48h}, {}^n PV_{box}^{168h}) \quad (6.2)$$

At every grid point (i, j) the 48 h forecasts of the variable geopotential height at 200 hPa (Z200) is correlated with the box average of the 168 h forecast PV.

Based on the research questions described above different atmospheric variables are correlated with the 7-day forecast PV: (i) Geopotential heights at 200 and 500 hPa (Z200/Z500) are chosen for testing if atmospheric blocking downstream is involved in PV streamer formation; (ii) Equivalent potential temperature at 850 hPa (THE850) is an indicator if latent heating upstream intensifies the ridge and consequently enhances the PV streamer. For this investigation the vertical wind at 700 hPa (w700) is considered, too. Uplift of air at the same geographical point as high THE850 implies rising air, which leads to condensation and thus latent heat release.

The current ensemble correlation method has its limitations since it is well known in statistics that correlation does not directly imply causality. Furthermore the ensemble correlation does not work for a small spread of the EPS. Forecast histograms introduced in Section 5.2.2 provide the information about the spread behaviour of PV streamer forecasts.

6.2 Example case

Figure 6.1 shows one example from the set of 75 PV streamer episodes. The chosen case illustrates nicely the main aspects of the ensemble correlation approach for PV streamer forecasts.

The 1.5 PVU contour lines from the ECMWF analysis (black lines in Figure 6.1) depict the evolution of the PV streamer from 26 November 2005 (left) to 01 December 2005 (right). The initialisation date of this case is 24 November 2005 and the verification date is 01 December 2005 (right panel in Figure 6.1). It can be seen that the PV streamer originates from high PV over Western Europe, which already existed a few days before the verification date. During these days this PV reservoir narrowed and the PV streamer stretched into the African continent. Upstream of the PV reservoir, a ridge built associated with a northward wave breaking. This structure is marked by low PV values being advected towards the pole.

The colours in Figure 6.1 show the correlation coefficient r between the forecasts of selected atmospheric variables and the 168h forecast PV. The PV is averaged in the red box (apparent in the right column of Figure 6.1). A correlation coefficient of 0.23 is statistical significant (level of 95%) for 50 participants, which are assumed to be independent for the sake of simplicity. From left to right the 48 h to 168 h forecast steps are shown. Basis for the top panel in Figure 6.1 is the variable Z200 correlated with PV. The middle panel is calculated from THE850 and PV and the bottom panel shows the results of the correlation of PV with w700. The unit of the underlying variable w700 is hPas^{-1} and therefore negative values correspond

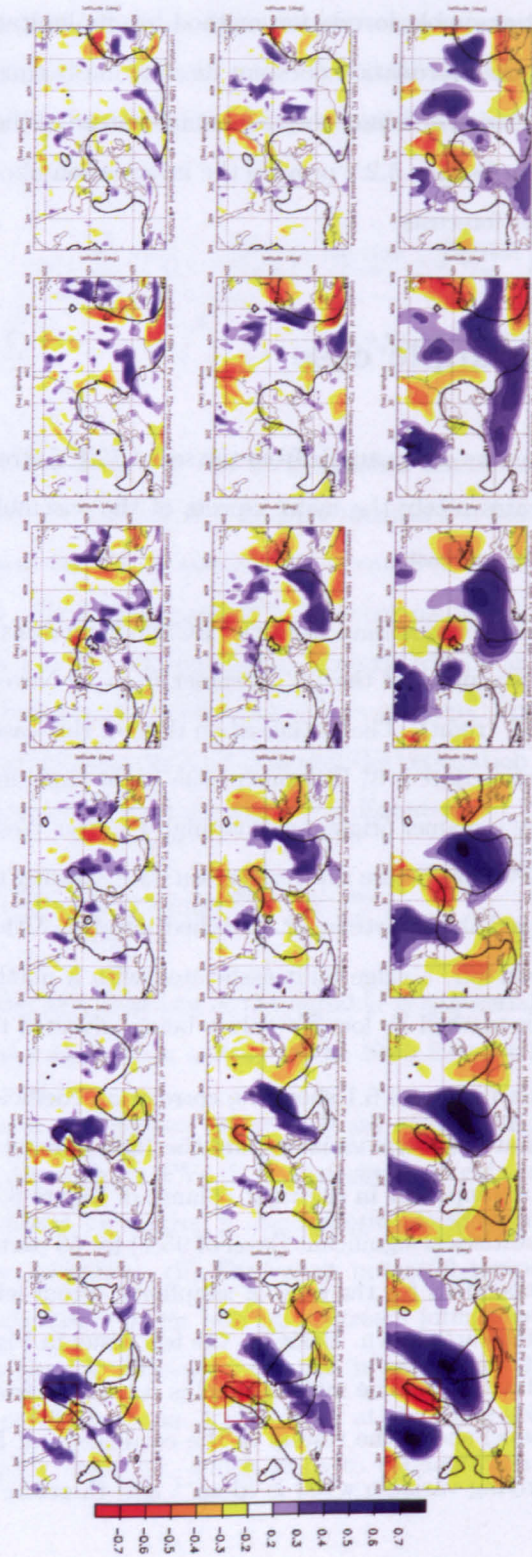


Figure 6.1: Correlation coefficients (in colours) between different atmospheric variables in the ensemble prediction system. Every grid point of (i) geopotential height at 200 hPa (top panel), (ii) equivalent potential temperature at 850 hPa (middle panel) and (iii) vertical wind at 700 hPa (bottom panel) is correlated with upper tropospheric PV averaged in a box (red box in right panels). The PV from 168 h forecast is correlated with atmospheric fields from 48 h (left panel) to 168 h (right panel) (details described in text). Black lines are the 1.5 PVU ECMWF analysis from 0000 UTC 26 November 2005 (left) to 0000 UTC 01 December 2005 (right).

to rising airmasses, which supports the release of latent heat as explained before. The example Equation 6.2 is the basis for the upper left image in Figure 6.1.

In the direct environment of the PV streamer high values for r are obvious. Low geopotential heights (red colours in top panel), cold temperatures (red colours in middle panel) and downdrafts at the back side (blue colours in bottom panel) as well as updrafts front side (red colours in bottom panel) of the PV streamer are clearly seen from three days before the verification date onwards.

The images in the middle panel show high $r_{THE850/PV}$ values (blue colours) east of the upstream trough. This means 168 h forecast high (low) PV values correlate with high (low) forecast THE850 values. High equivalent potential temperatures suggest strong latent heating in this regions. In the same region high negative $r_{w700/PV}$ values (red colours) in the bottom panel of Figure 6.1 support this argument. Consequently the negative correlations imply uplift of air mass in 700 hPa in the early forecast steps support the 168 h PV streamer forecast. The high correlations in THE850 and w700 already exist five days before the PV streamer has its southernmost extension (left panel of Figure 6.1). These processes lead to a poleward transport of warm moist air, which intensifies the ridge. As mentioned before, the top panel of Figure 6.1 depicts the correlation coefficients of PV with Z200. The maximum (positive blue r values) in the environment of the ridge is evident. This additional precursor can be clearly seen three days before the PV streamer occurred, and first indications five days before the verification date of the PV streamer. In summary it can be stated that a correct predicted ridge and poleward wave breaking in the early forecast steps are important for the 7-day PV streamer forecast for this chosen PV streamer episode.

Another striking feature in the $r_{Z200/PV}$ results (top panel in Figure 6.1) is the maximum downstream of the PV streamer. This feature indicates a potential blocking event. Atmospheric blockings are vertically coherent and quasi-stationary high pressure systems in the extratropics whose amplitude is such that they disrupt the prevailing westerly circumpolar flow (Schwierz et al., 2004b). Due to this fact the high PV air mass arriving from the west is forced to extend to the south.

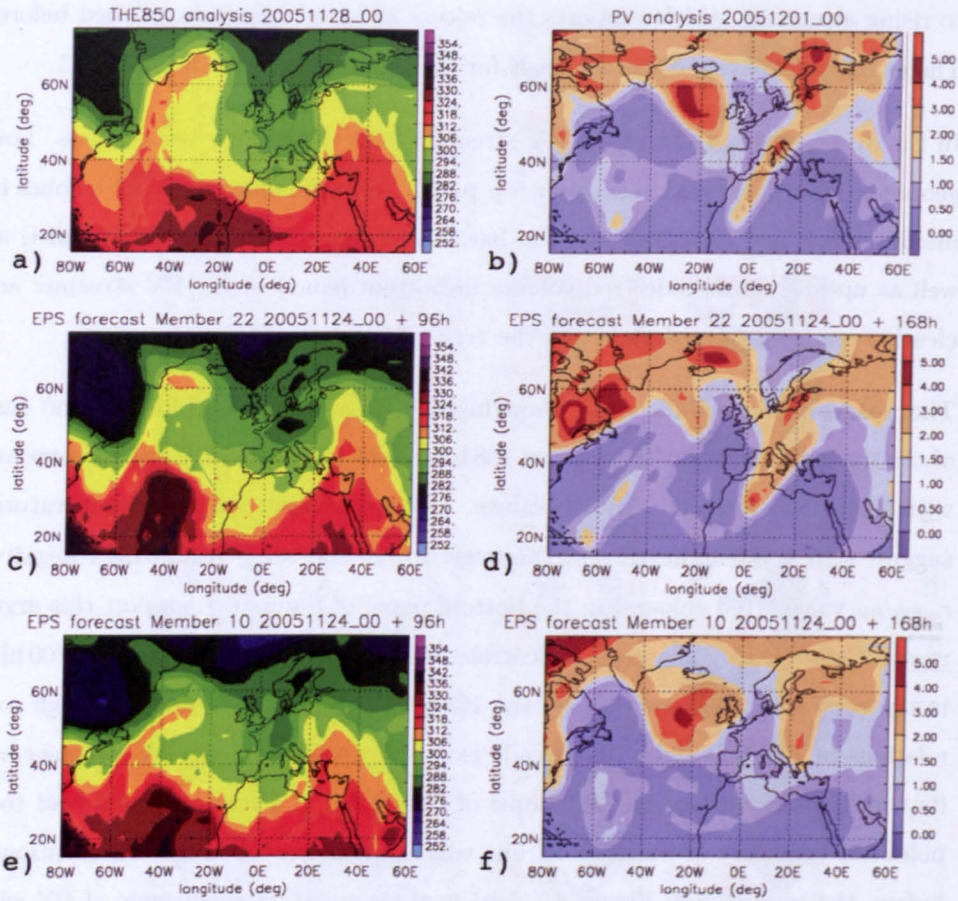


Figure 6.2: Comparison of equivalent potential temperature at 850 hPa (left) and upper-tropospheric PV (right) for selected 96 h EPS member THE850 forecasts (c and e), 168 h EPS member PV forecasts (d and f) and ECMWF operational analysis at the respective dates (a and b).

To illustrate the correlation approach, Figure 6.2 provides a detailed look into selected member forecasts and the corresponding analysis fields for THE850 (left column in 6.2) and PV (right column in Figure 6.2). The upper row in Figure 6.2 shows the analysis of THE850 (Figure 6.2a) at 28 November 2005 and the PV analysis at 01 December 2005, which is the verification date of this PV streamer episode (Figure 6.2b). The two bottom rows in Figure 6.2 show forecasts from selected EPS members (no. 22 and 10) for the PV streamer case described above. The left-column panels for these two members are 96 h forecasts of THE850 and the right-column panels are 168 h forecasts of PV.

The analysis PV field (Figure 6.2b) shows a long and narrow PV streamer stretching from central Europe and the Mediterranean Sea into the Sahara with its southern tip at almost 20°N . The comparison with the 168 h PV streamer forecasts (Figures 6.2d and f) shows two different solutions of the upper-tropospheric evolution. The EPS member 22 in Figure 6.2d predicted the PV streamer in fairly good agreement with the analysis. It is a little wider and the southern extension is slightly smaller. However, the location and strength match satisfactorily; the PV values at the southern tip are even forecast slightly higher than analysed. The 168 h PV forecast of member 10 (Figure 6.2f) predicts the overall upper-tropospheric evolution with its ridge-trough-ridge-trough pattern over the North Atlantic and Europe well. However, the stretching of the PV streamer from Europe into Africa is missed by this forecast.

The THE850 analysis (Figure 6.2a) four days before verification time of the PV streamer (Figure 6.2b) shows a distinctive ridge over the western North Atlantic with high temperatures reaching Greenland. Furthermore a trough, denoted by cooler temperatures east of the ridge over northwestern parts of Europe is evident. This trough is connected to the PV streamer three to five days later. The two 96 h THE850 forecasts (Figures 6.2c and e) predict the general ridge-trough pattern reasonably accurately. Especially the trough over Europe has the same temperature values as in the analysis. The most obvious deviations can be seen in the ridge structure. The temperature values vary within the analysed (Figure 6.2a) and predicted ridges (Figures 6.2c and e). Whilst the analysis shows a wide ridge, both forecasts predict a narrower feature. Especially the forecast of member 10 in Figure 6.2e shows only a thin fragment of warmer air (up to 288 K) advected into polar regions over Greenland and no values up to 306 K as far north as Greenland. In contrast the forecast of member 22 shows some warmer air of 306 K at the southern edge of Greenland and thus closer to the analysis. This shows that the member with the better THE850 field during early stages of the forecast also had a more accurate upper-tropospheric PV field three days later (cf. Figure 6.2d).

In summary it can be stated that this case shows impressively a few precursors,

which are necessary for PV streamer evolution. For satisfactory PV streamer forecasts it is very important that NWP models simulate these features correctly in the early stages of forecasts.

6.3 Statistical analysis over all PV streamer

After the detailed look into one of the 75 PV cases, this section continues with the analysis of all cases.

As mentioned in section 6.1 the ensemble correlation was calculated for Z200/Z500, THE850, w700 and PV 24 h - 168 h forecasts with the 168 h PV forecast (box average around the PV streamer) for all 75 PV streamer cases. Geographically fixed mean calculations over all 75 cases for each lead time correlation turned out to be not useful. As mentioned in Chapter 5 the final PV streamers extend from 35°W to 30°E (cf. Figure 5.3). Therefore the geographical distribution of the atmospheric structures in THE850, w700 and Z200/500 are widely spread and therefore the resulting correlation coefficients as well. In consequence the geographically fixed mean calculation eliminates the interesting features.

To account for this effect a composite was generated where all correlation fields are shifted. In section 3.4 boxes surrounding the PV streamer were introduced. All correlation fields were shifted by the longitudinal distance between the box centre and 0°E. In other words the longitudinal centres of all PV streamers are located at the Greenwich meridian for this composite.

In Figure 6.3 the mean for each lead time over all 75 shifted correlation results is shown. The presentation is identical to Figure 6.1. In colours the correlation coefficient r is shown between the forecasts of selected atmospheric variables at certain forecast steps and the 168 h forecast PV. The 168 h PV forecast is averaged between 25°N to 40°N and 12.5°W to 12.5°E. Columns in Figure 6.3 are 96 h to 168 h forecast steps. Basis for the top panel in Figure 6.3 is the variable PV correlated with the 168 h box-averaged PV, in contrast to the top panel of Figure 6.1, where

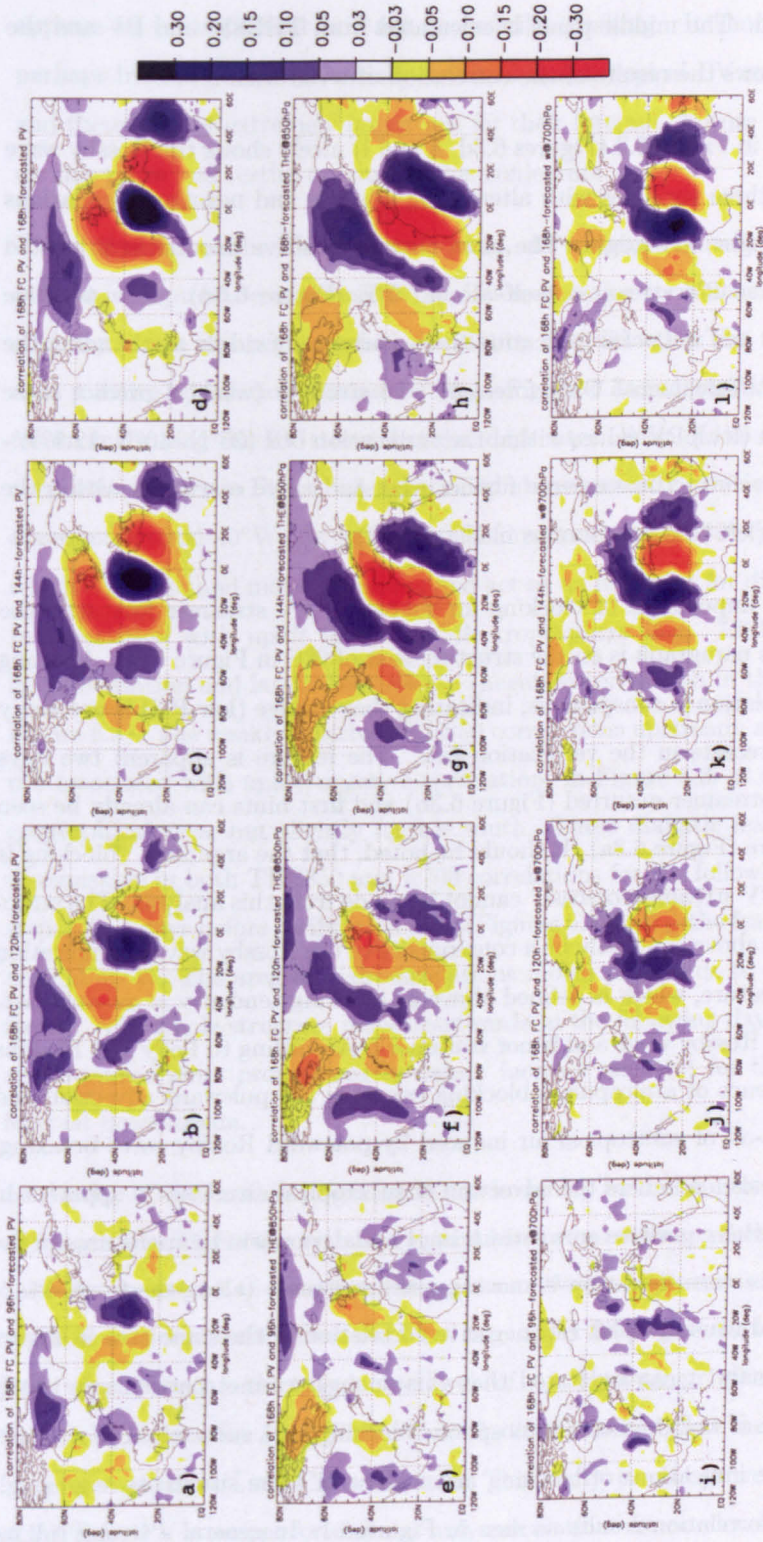


Figure 6.3: Mean over all 75 PV streamer episodes correlation coefficients (in colours). All fields are shifted with the result that the PV streamer verification boxes have their longitude centre at 0°E (technical details see text). Every grid point of (i) upper-tropospheric PV (top panel), (ii) equivalent potential temperature at 850 hPa (middle panel) and (iii) vertical wind at 700 hPa (bottom panel) is correlated with upper-tropospheric PV averaged in the verification box (12.5°W - 12.5°E and 25°N - 40°N). The PV from 168 h forecast is correlated with atmospheric fields from 96 h (left panel) to 168 h (right panel) forecasts (details described in text).

Z200 is displayed. The middle panel is calculated from THE850 and PV and the bottom panel shows the results of the correlation of w700 with PV.

The last column in Figure 6.3 (Figures 6.3d, h and l) nicely shows the Rossby wave structure in all three variables with alternating positive and negative correlations representing troughs and ridges. The most obvious positive maximum is located in the area of the PV streamer itself around 0°E (Figure 6.3d). The negative correlations east and west of it indicating the occurrence of ridges surrounding the fairly narrow PV streamers. Only forecasts who strongly (weakly) predict these features get high (low) PV values within the verification box ($25^{\circ}\text{N} - 40^{\circ}\text{N}$, $12.5^{\circ}\text{W} - 12.5^{\circ}\text{E}$). All these structures emerge further west and move eastwards within the forecast period (left to right columns in Figure 6.3).

Concerning the importance of blocking for successful PV streamer forecasts, the attention in this paragraph is on the structure east of 0°E in Figure 6.3d. A strong (negative) correlation is conspicuous, indicating that a ridge (low PV) is necessary for high PV forecasts in the verification box. The feature is apparent two days before the PV streamer occurred (Figure 6.3b) and first hints can already be seen three days before (Figure 6.3a). It should be noted, that the argument “blocking is important for PV streamer forecast” cannot be made from this analysis. The structures explained above can easily be a consequence of the Rossby wave configuration as such. The feature, which is defined above as blocking tendency is moving eastwards with the Rossby wave and is not stationary. According to Pelly and Hoskins (2003), the essence of atmospheric blocking events is the poleward advection and subsequent cut-off of subtropical air induced by poleward Rossby wave breaking. From the analysis made here the advection of subtropical airmasses is apparent in figures 6.3f-h, where positive correlations imply relative warm temperatures in the same area. This warm moist air is moving northeastwards (along the front side of the trough) and causing uplift (cf. negative correlation in the same area in Figure 6.3l). In summary it can be stated that this analysis cannot particularly testify the importance of well predicted atmospheric blocking for a successful PV streamer forecast. Some indications of blocking are evident in some situations, e.g. single PV streamer correlation results as seen in Figure 6.1. In general a strong ridging

appears to be important but not necessarily blocking. It should be noted that perhaps blocking is not essentially involved in subtropical PV streamer formation and therefore not extremely important for their forecast. Future analyses can take up this point and testify or confute this conjecture.

Three days before the PV streamers occur, the strongest correlation of THE850 is evident in Figure 6.3e at around 20°W. These negative correlations imply relatively cold dry air in this region, which is relating to a trough. The trough is marked as a positive correlation around 10°W in Figure 6.3a, which functioned as a PV reservoir forming the PV streamer three days later. West of the negative THE850 correlation values in Figure 6.3e (described above), weakly positive correlations are apparent around 40°W. As mentioned before positive THE850 correlations imply relatively warm and moist airmasses and act as an indicator for diabatic processes. In connection with uplift in the middle troposphere (e.g. 700 hPa) this results in condensation and latent heat release (negative correlation in the bottom row of Figure 6.3). The weakly positive THE850 correlations upstream, around 40°W, are not associated with uplift/negative correlations in Figure 6.3i at exactly the same geographical area, but slightly further south. These diabatic features are clearly recognisable in both THE850 and w700 correlations for the following forecast time steps. Two days before verification date (Figures 6.3f and j) the features are located around 40°W. The area of high correlations moves polewards to the east in both figures. The whole structure moves eastwards in the following days of the forecast and becomes more pronounced (r values increase slightly) for the PV streamer forecast downstream.

At the day of verification (Figure 6.3h) and one day before (Figure 6.3g) the shape of the positive THE850 correlation resembles a warm conveyor belt (WCB). These belts are connected to extratropical cyclones. Warm moist air is advected northwards front-side the cold front and lifted into upper-levels and the belt bends to the right when it reaches the tropopause level (cf. e.g. Browning, 1990; Carlson, 1998). Climatological studies (e.g. Eckhardt et al., 2004) showed that the North Atlantic is a preferred region for WCB occurrence. This study, cannot prove the importance of WCB for PV streamer forecasts as only calculations for one level (850 hPa) were

performed. The WCB-like shape gives some hints of a possible influence of WCB on PV streamer forecasts downstream and can be the basis for future studies.

Another interesting feature in the THE850 fields are strong positive correlations at 100°W (Figure 6.3e), thus another wavelength further west. In consequence EPS members, which produce high (low) THE in 850 hPa three days before the verification date predict high (low) PV within the verification box in the 7-day forecast. However, these positive THE850 correlations do not necessarily imply diabatic processes because negative correlations (uplift) in w700 are not apparent (cf. Figure 6.3i). Furthermore this feature diminishes over the days. It appears to be important that a ridge exists at this stage (three days before verification time) in the forecast further west to amplify the Rossby wave.

As mentioned in the beginning of this section the geographical fixed mean over all PV streamer correlation results lead to an elimination of the interesting structures. Beside the mean calculations of the shifted correlation fields, means over PV streamer correlations divided into longitudinal zones (introduced in Section 5.1) were performed. The outcomes reflect the results presented above and can be seen in Figures A.6 to A.10 in Appendix A.

In summary the diabatic processes upstream appear to be more important for a successful 7-day forecast of deep PV intrusions into the subtropics than blocking downstream. Furthermore the Rossby wave structure and a high amplitude of the wave in the early stages of the forecast and their correct reproduction in the model influence the medium-range prediction of subtropical PV streamers.

6.4 Correlation signals from hurricanes

As presented in section 4.3 hurricanes can influence the tropospheric evolution downstream. (For example Jones et al., 2003) demonstrated the crucial role of diabatic processes during an ET when a hurricane becomes an extratropical cyclone.

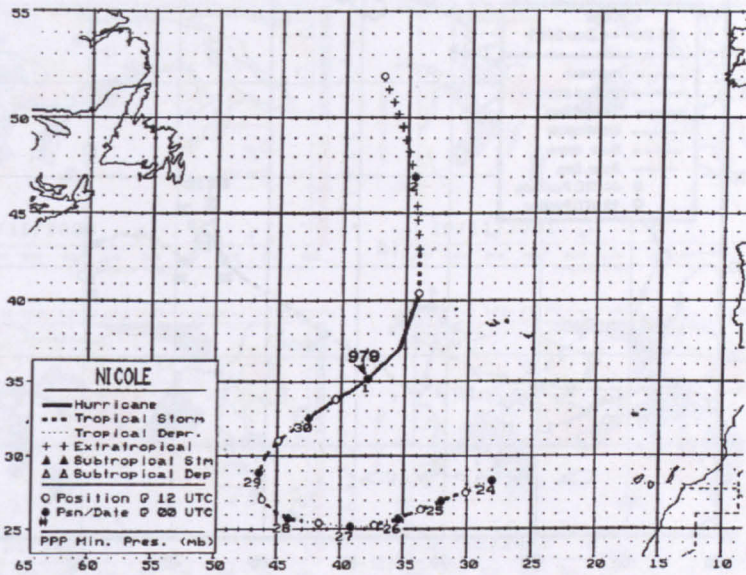


Figure 6.4: Track of Tropical Cyclone *Nicole* from 00 UTC 24 November to 12 UTC 02 December 1998 (extracted from NHC Preliminary Report-Hurricane Nicole, accessed on <http://www.nhc.noaa.gov/1998nicole.html>, 15 February 2011).

The outflow of a tropical/extratropical cyclone during ET can influence the midlatitude flow. In this section the focus is on the PV streamer cases within the dataset where a hurricane occurred upstream several days ahead.

Within the years 1996 to 2008, which are the focus of this study, only two PV streamers over the African continent were preceded by a hurricane in the North Atlantic basin. The number is fairly low, which is mainly because the seasons of both phenomena do not match. As shown in Figure 5.2 deep PV intrusions occur from November to April. The hurricane season in the North Atlantic usually starts in June and ends in November. Therefore it is not surprising that both cases occurred at the end of November. As mentioned in section 2.4.2 the hurricane track data were taken from the NHC's Tropical Cyclone Reports.

The last hurricane in 1998, named *Nicole*, occurred from 24 November to 01 December. Figure 6.4 shows its 12 hourly geographical position. Its track was over the Atlantic Ocean only, without a landfall. It started as a tropical depression at 28°N/30°W and moved westwards until 28 November (position: 27°N/46°W). In

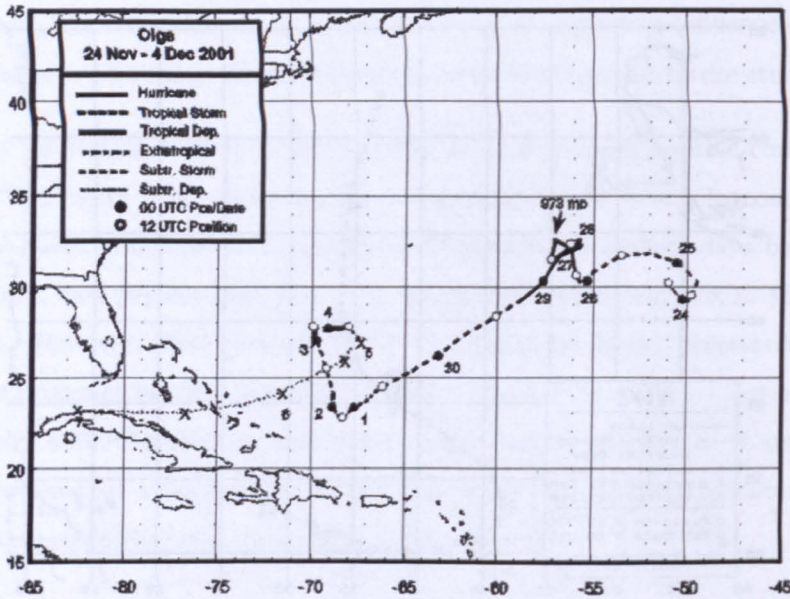


Figure 6.5: Track of Tropical Cyclone *Olga* from 00 UTC 24 November to 12 UTC 04 December 2001 (extracted from NHC Tropical Cyclone Report - Hurricane *Olga*, accessed on <http://www.nhc.noaa.gov/2001olga.html>, 15 February 2011).

the following days the track curved polewards and slightly eastwards. During this stage *Nicole* became a hurricane for two days at around 32°N to 40°N and 34°W to 43°W . Within this time, a PV streamer evolved downstream with its southernmost extension around 20°E at 28 November. Although the temporal evolution of these atmospheric features match, the correlation results do not show any signs of a hurricane influence on the PV streamer forecast. This can have several explanations. First, the hurricane has its biggest influence on the upper-level development when it occurs at the front side of a trough, which was not the case for *Nicole*. Instead it moved into the region behind the trough upstream the PV streamer under study. The second explanation is related to the correlation approach itself. The hurricane could have changed the upper-level structure but none of the EPS members captured this. The correlation technique can only represent the influence of a feature when the EPS has sufficient spread.

The second hurricane, which coincided with a PV streamer from the 75 PV streamer dataset, occurred in November 2001. Figure 6.5 shows its 12 hourly geographical position. *Olga* became a hurricane on 26 November 2001 around $31^{\circ}\text{N}/56^{\circ}\text{W}$. It

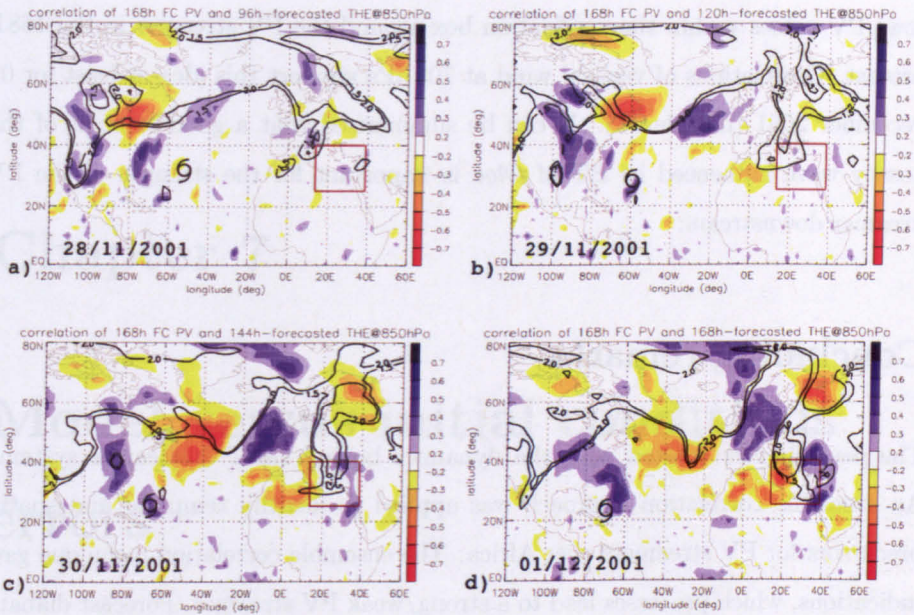


Figure 6.6: Correlation coefficients (in colours) between equivalent potential temperature at 850 hPa (THE850) and upper tropospheric PV averaged in a box (red box in Figure 6.6d). The PV from 168h forecast is correlated with THE850 fields from a) 96h, b) 120h, c) 144h and d) 168h forecasts (details described in section 6.1). Black lines are the 1.5 PVU and 2.0 PVU ECMWF analysis from a) 1200 UTC 28 November 2001 to d) 1200 UTC 01 December 2001. The black spiral symbols mark the hurricane position.

stayed a hurricane for 2.5 days without changing its position remarkably. After 29 November it was classified as a tropical storm and moved towards the south-west until it reached 22°N/68°W at 01 December 2001. Within this time a PV streamer downstream evolved with its southernmost extension at 01 December 2001 around 25°E. The PV streamer development is shown as black contour lines (1.5 and 2.0 PVU) in Figure 6.6. The hurricane positions are marked as black spiral symbols in Figure 6.6 as well.

The correlation results in Figure 6.6 show a weak influence of *Olga* on the 168h PV streamer forecasts. High positive THE850 correlation values are evident in the vicinity of the hurricane/tropical storm position for the last four lead times of the forecast, especially at the verification date (01 December 2001) and the day before. Therefore it can be stated that EPS members forecast high (low) THE850, possibly generated by *Olga*, in the early stages of the forecast, get higher

(low) PV values within the verification box around the PV streamer in the 168 h forecast. Correlations of vertical wind at 700 hPa support this idea at least for 01 December 2001 (not shown). It can be summarised that a good forecast of the Rossby wave influenced by ET of *Olga* is important for the strength of the PV streamer downstream.

Concluding remarks

The past chapter treated with the dynamics behind the PV streamer systems. An ensemble correlation approach was applied to identify temporal and spatial precursors for PV streamers over Africa. The ensemble correlation technique gave indications, which processes lead to a strong/weak PV streamer. Forecast diabatic heating processes upstream in early stages is crucial for a successful PV streamer forecast in the mid- to long-range. Blocking events over Europe do not appear to have a dominating influence on the strength of the PV streamer.

Chapter 7

Model versus initial conditions errors

Chapter 5, especially Section 5.2, analysed errors in forecasting PV streamer situations. RMSEs were found to be twice as high as the spread of the EPS implying an underdispersive behaviour. Section 5.2.3 identified the displacement of the PV streamers in the forecasts as one possible reason for the high RMSEs. Furthermore the ensemble correlation in Chapter 6 highlighted the processes that are necessary for a successful PV streamer forecast. The focus in this chapter is on the question of the relative importance of model versus initial conditions errors in increasing RMSEs in the EPS.

7.1 Method

Different geographical boxes were used for verifying the model performances in the PV streamer cases (see Section 3.4). For the following analysis another box is defined. This box has a meridional extent of 60° (15°N - 75°N) and 150° in the zonal direction. This large box spans the whole North Atlantic including Europe and Northern Africa. It covers the area where the Rossby wave and all the processes

important for a subtropical PV streamer forecast occur (cf. Chapter 6). The eastern and western borders of the box will be varied as explained below.

The basic idea of this analysis is to look how upper-level PV errors of single EPS members are changing over lead times. Therefore every single EPS member's RMSE (averaged within the box) was calculated. The forecast RMSEs were calculated with respect to the operational analyses from the ECMWF. All 75 PV streamer cases were examined for one to seven day forecasts.

The forecast error increases over lead time for different reasons. The two main sources are the initialisation with the analysis fields and model errors. The latter comprise numerical errors in the dynamical core (advection, time stepping) and parametrisations. Numerical errors arise because interactions between scales cannot be represented and cause so-called aliasing errors. In addition it is well-known that e.g. parametrisations cause errors, because simplifications need to be made to represent the effects of small-scale processes on the coarser grid cells. Secondly, good forecasts need initial conditions as close as possible at the truth. As we know since Lorenz (1963) small deviations in initial conditions can dramatically change the final solution. This chaotic and non-linear behaviour of the atmosphere causes an increasing error over lead time. The EPS concept is developed to capture this uncertainty. To get the perturbed analysis fields for the 50 EPS members, SV calculations are performed. As explained in Section 1.3 a tangent linear model is used to find the fastest growing perturbations for an optimisation time of 48 hours.

The hypothesis to test in this analysis is: Do errors, which exist at short lead times (48 h), grow linearly so that members performing poorly in the short-range have the highest RMSEs at longer lead times as well? Or do non-linear error growth and model errors dominate the forecast? In the latter case good (bad) short-range forecasts can become poorer (better) compared to other EPS members.

Calculating RMSEs within a fixed longitude/latitude box can change the error calculations, when atmospheric features and their associated errors enter or leave this box. To take this into account, the box was designed to be following the group velocity of the Rossby wave. This way so-called Hovmoller diagrams were produced

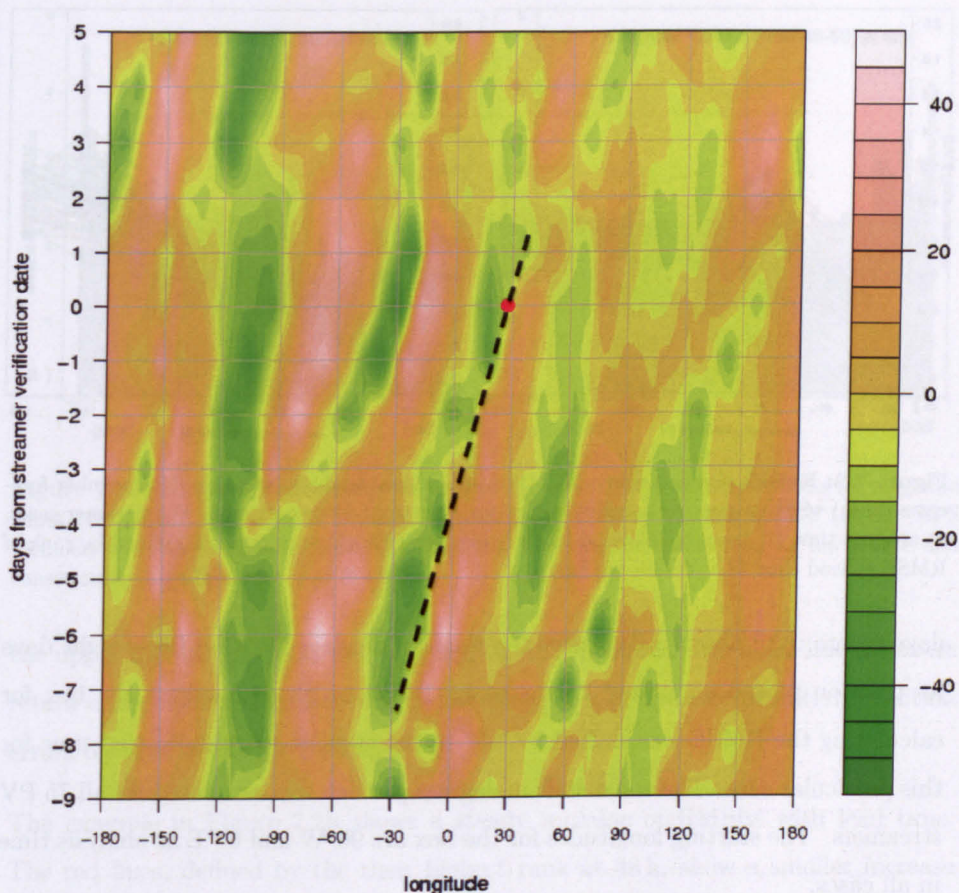


Figure 7.1: Hovmoller diagram of the meridional wind component at 300 hPa averaged between 30°N and 60°N from 1200 UTC 27 December 1998 (day: -9) to 1200 UTC 10 January 1999 (day: +5). The dashed line marks the PV streamer position and the red dot the PV streamer position at verification time.

for every single PV streamer case. One example diagram is shown in Figure 7.1. The meridional wind component at 300 hPa from the operational analysis of the ECMWF was used. The wind was averaged between 30°N and 60°N. The averaged wind value is shown for all longitudes from nine days before to five days after the PV streamer occurred. The PV streamer was located at 30°E (marked as red dot in Figure 7.1) at day zero. Based on these diagrams, troughs and ridges and Rossby waves can be detected. High (low) values in Figure 7.1 show southerly (northerly) winds, which occur at the front side (back side) of a trough. The dashed black line in Figure 7.1 marks the position of the trough under study. It is evident seven

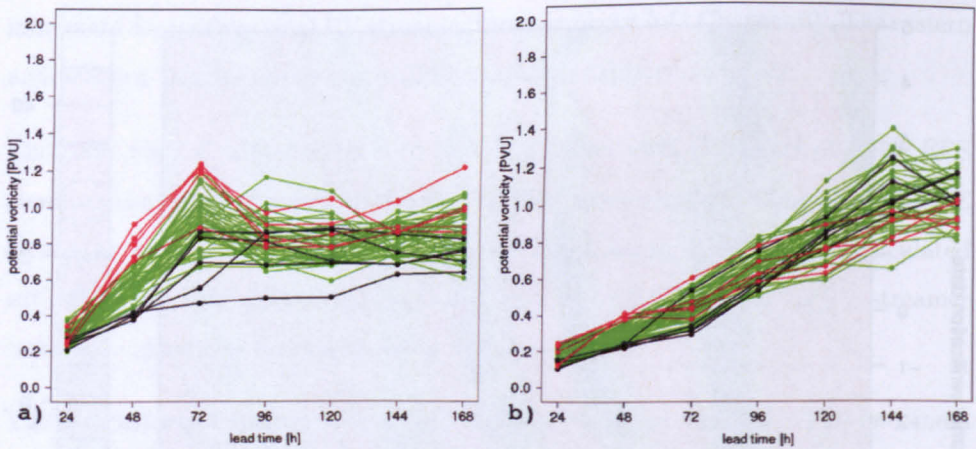


Figure 7.2: RMSEs (forecast minus ECMWF operational analysis) of single EPS member forecasts (lines) within a east-west shifted box (details see text) for two example PV streamer cases, a) analysis time 10 January 1998 and b) 19 November 1999. Line colours are defined by rank of RMSE at lead time 48 h (details see text).

days before until about a day after the verification date. Within these eight days its position moved about 60° to the east. Based on these numbers the box for calculating the RMSE was shifted by 7.5° to the east for every daily lead time for this particular case. The zonal shift in degrees per day was estimated for all 75 PV streamers. The starting longitudes for the box are 90°W and 60°E at analysis time in all cases.

7.2 Results

The RMSE calculations in the shifted box resulted in RMSE over lead time figures as displayed for two example PV streamer cases in Figure 7.2. Both figures show one line per member, which creates 50 lines in different colours in each figure. The colours are defined by the rank of the RMSE of a member at lead time 48 h. Members with the five highest RMSEs at 48 h are drawn in red and members having the five lowest RMSEs are drawn in black. The other lines are displayed in green.

Figure 7.2a shows a growth of RMSEs with lead time until 72 h. Afterwards the errors are fairly stable with increasing lead time. The members with the five highest and lowest RMSEs at 48 h follow this pattern. The red line members remain in

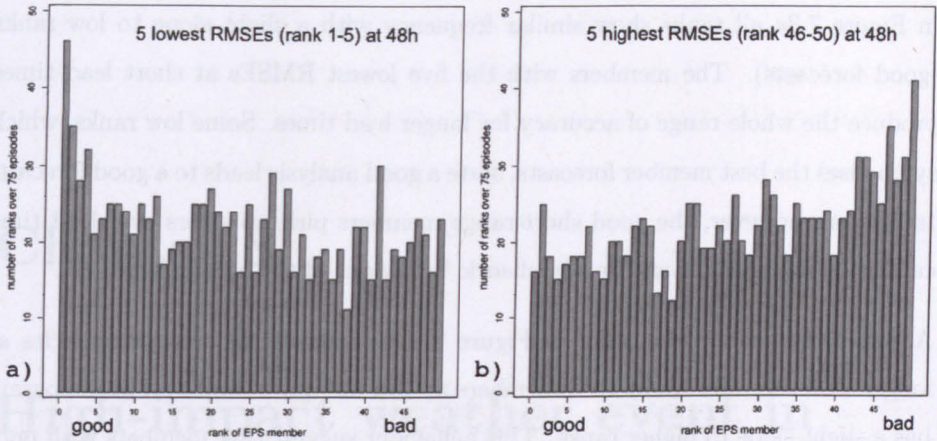


Figure 7.3: Histogram of occurrence frequencies of ranks of EPS member RMSEs for long lead times (120-168 h). Split in EPS members with the five lowest RMSEs at 48 h (a) and EPS members with the five highest RMSEs at 48 h (b). Low rank numbers stand for low RMSE and consequently high ranks for high RMSEs.

the upper half of the ensemble, with high RMSEs, whereas the black line members retain a low RMSE over lead time. This suggests a dominance of initial condition errors on the forecast performance.

The example in Figure 7.2b shows a steady increase of RMSEs with lead time. The red lines, defined by their highest rank at 48 h, show a smaller increase compared to all other lines. In contrast the RMSEs marked by black lines (five smallest RMSEs at 48 h) increase stronger compared to the rest. This is in strong contrast to Figure 7.2a and suggests a dominant influence of non-linear effects and model errors.

Figure 7.3 summarises the analysis for all 75 PV streamer cases in a rank histogram. The focus of the figure is to find out, which of the two cases shown in Figure 7.2 is dominant over all cases. The abscissa indicates the rank of the RMSE of a member relative to all EPS members. The occurrence frequency is given on the ordinate. Figure 7.3a shows the frequency of RMSE ranks at the three longest lead times (120 h, 144 h and 168 h) for the members with the five lowest RMSEs (best forecasts) at 48 h (cf. black lines in Figure 7.2). Similarly the frequency of RMSE ranks for long lead times for the members with the five highest RMSEs at 48 h are shown in Figure 7.3b.

In Figure 7.3a all ranks show similar frequency with a slight slope to low ranks (good forecasts). The members with the five lowest RMSEs at short lead times produce the whole range of accuracy for longer lead times. Some low ranks, which symbolises the best member forecasts, state a good analysis leads to a good forecast. In general, however, the good short-range members pick up errors over lead time caused by model error and/or the chaotic behaviour of the atmosphere.

A similar behaviour is evident in Figure 7.3b. It shows the rank frequencies at longer lead times for worst EPS members at 48 h are quiet similar. The histogram has a slight slope to higher ranks. This behaviour suggest that members with poor forecasts in the short-range perform least well at longer lead times compared to other members. The high RMSE at short lead times determines the bad quality of the long lead time forecasts. Even if best member forecasts are possible, worse short-range members have a smaller probability to result in good forecasts at longer lead times.

In summary, it can be said that a low (high) RMSE at short lead times create a tendency for a good (poor) long-range forecast. In general good (bad) short-range forecasts do not decide about good (bad) long-range forecasts, because of model errors and non-linear error growth increasing (decreasing) the RMSE.

Chapter 8

High-impact weather event in May 2008 - A TIGGE case study

Around 26 May 2008 a pronounced PV streamer penetrated from the North Atlantic into the western Mediterranean Sea followed by widespread dust mobilization over the Maghreb and a subsequent northward transport into central Europe. At the same time, strong southerly flow over the Mediterranean Sea caused heavy precipitation and flooding at the windward side of the European Alps. Using continuous and feature-based error measures as well as ensemble correlation techniques, this study investigates the forecast quality and predictability of synoptic and meso-scale aspects of this high-impact event in operational ensemble predictions from nine meteorological centres participating in TIGGE. TIGGE allows for an exciting new multi-model approach to investigating predictability of, e.g. high-impact weather and its dynamics.

The present study, following in this chapter, adds several new aspects to the published TIGGE research. Using novel feature-based and continuous analysis tools, it thoroughly assesses forecast performance and predictability of a pronounced RWB event and some of its impacts such as strong near-surface winds and heavy precipitation. Inter-ensemble comparisons reveal both model errors and problems with

the design of the EPS as well as the added value of a multi-model ensemble. Furthermore the study examines the dynamical linkage between the forecast qualities of upper- and lower-level features with a novel correlation approach.

8.1 Introduction

So far comparisons between ensembles from different centres are rare. Buizza et al. (2005) compared the ECMWF EPS, NCEP EPS and CMC EPS in a comprehensive study. Bourke et al. (2004) tested ECMWF and BoM predictions on their performance in the Southern Hemisphere. Both studies find a better performance of the ECMWF model and suggest a relation to the superior model and data assimilation system. Other comparisons between the NCEP EPS and the ECMWF EPS have been performed by Atger (1999), Wei and Toth (2003) and Froude et al. (2007).

In the past, comparisons between different ensemble systems were complicated by restricted data availability and the lack of a standardised format. Therefore the WMO program THORPEX established a new data archive called TIGGE that comprises ensemble predictions from different meteorological centres. Section 2.2 explained the details of the TIGGE dataset. Daily updated TIGGE forecast products and verifications are provided by Matsueda and Nakazawa (2011). First studies using the TIGGE database were published in the last three years. Pappenberger et al. (2008) proposed to use TIGGE for early flood forecasting and warning. Park et al. (2008) analysed forecast performance of the different models in the upper troposphere. Matsueda (2009) studied the predictability of atmospheric blocking events. Froude (2010) concentrated on the prediction of extratropical cyclone tracks. Johnson and Swinbank (2009) investigated a multi-model ensemble combining ECMWF, NCEP and UKMO EPS and found it to be superior to a single-model ensemble, mainly with respect to surface temperature, but also for geopotential height at 500 hPa and mean sea level pressure. These examples show the wide range of possible research activities and applications feasible with forecasts from the TIGGE database.

Hereafter, the chapter continues with a methodology section, where all methods are explained used for the case study. The following Section 8.3 describes the synoptic evolution of the PV streamer under study and its impacts. In Section 8.4 the forecast performance with respect to the large-scale evolution is presented. In Section 8.5 two types of related high-impact weather, a dust storm as well as heavy precipitation, are evaluated.

8.2 Methods

To study the forecast performance of the different models, again vertically averaged PV is considered. The TIGGE archive contains only selected pressure levels at 200, 250, 300 and 500 hPa. These are two more levels than archived for the ECMWF EPS. Therefore the calculation of the PV changes slightly to the one used in the other chapters. The vertical derivatives in Equation 3.3 have to be approximated. The PV is reformulated using finite differences. Equation 8.1 is used for calculating upper-tropospheric PV between neighbouring levels (200/250 hPa, 250/300 hPa, 300/500 hPa).

$$PV_p \cong -g \frac{\partial \Theta}{\partial p} \cdot (f + \bar{\xi}) \cong -g \frac{\Theta_{p_{lower}} - \Theta_{p_{upper}}}{\Delta p} \cdot \left(f + \frac{\xi_{p_{lower}} + \xi_{p_{upper}}}{2} \right), \quad (8.1)$$

where Δp is the pressure thickness of the layers. The final vertically averaged upper-level PV value is computed as the weighted average over the resulting PV values of the three layers. The weights are determined by the thickness of the layers in pressure coordinates. A comparison, similar to Figure 3.1 in Section 3.1, between this PV approximation and one using all ECMWF model levels shows similar structures but somewhat smaller absolute values.

Two complementary error measures were applied to the different ensemble forecasts for this case. First, PV spatially averaged within a box surrounding the PV streamer was considered. Comparisons between ensemble means and analysis fields were undertaken using RMSE and ensemble spread for the different operational centres. The differences of these two measures indicate whether the ensemble forecasts

Table 8.1: Number of EPS members that do not match the analysed PV streamer. For details of the method, see Section 8.2.

model	members	24h	48h	72h	96h	120h	144h	168h
BoM	32	0	0	0	0	12	1	2
CMA	14	0	0	0	3	3	2	3
CMC	20	1	7	7	5	7	10	12
CPTEC	14	0	0	0	0	0	1	0
ECMWF	50	5	10	5	7	4	4	22
JMA	50	0	7	2	8	14	10	12
KMA	16	0	0	6	5	5	2	4
NCEP	20	0	0	6	4	6	5	9
UKMO	23	0	1	2	2	10	8	6

are under- or overdispersive for this synoptic situation. Second, a feature-based error measure was applied to the PV streamer. The error assessment compares structural differences within the forecast and analysed streamers.

The PV streamers were identified using the method introduced in Section 3.2. Also the threshold values for the identification of $D \leq 800\text{km}$ and $L \geq 1500\text{km}$ as well as the 1.5 PVU contour line are used.

Matches between the forecast and analysis data are obtained by comparing the position of the PV streamers. If no overlapping points are found in the analysis and forecast, the closest streamer with a maximum distance of 500 km is considered as a match. In addition, if the distance between the line points, marking the connection to the main body of stratospheric air are more than 2000 km away from each other, the PV streamers are considered to be different systems. Cut-offs and larger troughs of stratospheric air are not included in the comparison, which reduces the number of ensemble members considered for this analysis for longer lead times (cf. Table 8.1). The centre of mass is used to compare the position of the PV streamer in the forecast in relation to the analysed PV streamer. For the interpretation of the result it should be borne in mind that minor changes in the shape of the stratospheric airmass can substantially change the northernmost point of an identified PV streamers, which in turn has a large impact on the centre position and the forecast error.

8.3 Synoptic overview

On 20 May 2008 a pronounced upper-level disturbance started to penetrate from the mid-latitude North Atlantic into the Mediterranean Sea. Figure 8.1 shows the time evolution of this trough between 21 and 26 May 2008 using PV. The streamer originates from a PV reservoir over the North Atlantic and northern Europe on 21 May 2008 (Figure 8.1a). A surface low pressure coincided with this PV reservoir. In the course of the following days a large-scale ridge forms to the west of the developing PV streamer (Figure 8.1b) and extends far northward between 23 and 24 May 2008 (Figure 8.1c). At the surface, high pressure builds

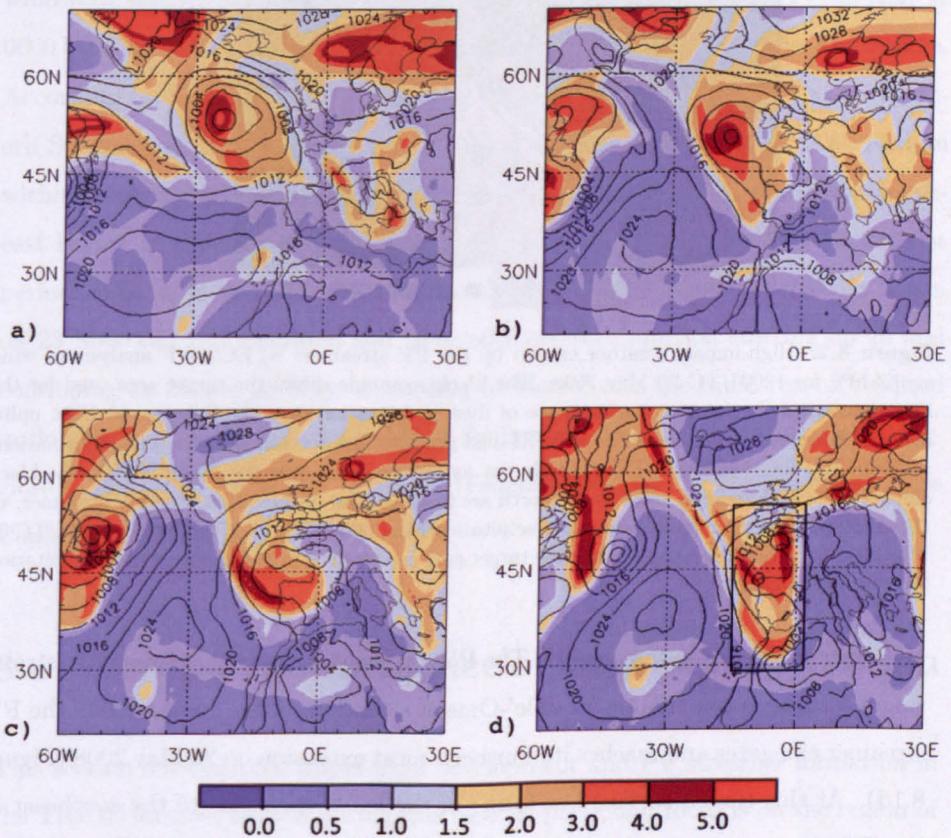


Figure 8.1: Synoptic development between 21 and 26 May 2008 as represented by PV (colours) and mean sea-level pressure (contours every 4 hPa) from ECMWF analysis fields. a) 1200 UTC 21 May 2008, b) 1200 UTC 23 May 2008, c) 1200 UTC 24 May 2008 and d) 1200 UTC 26 May 2008. The black rectangle in d) shows the area used for the investigation of the forecast performance.

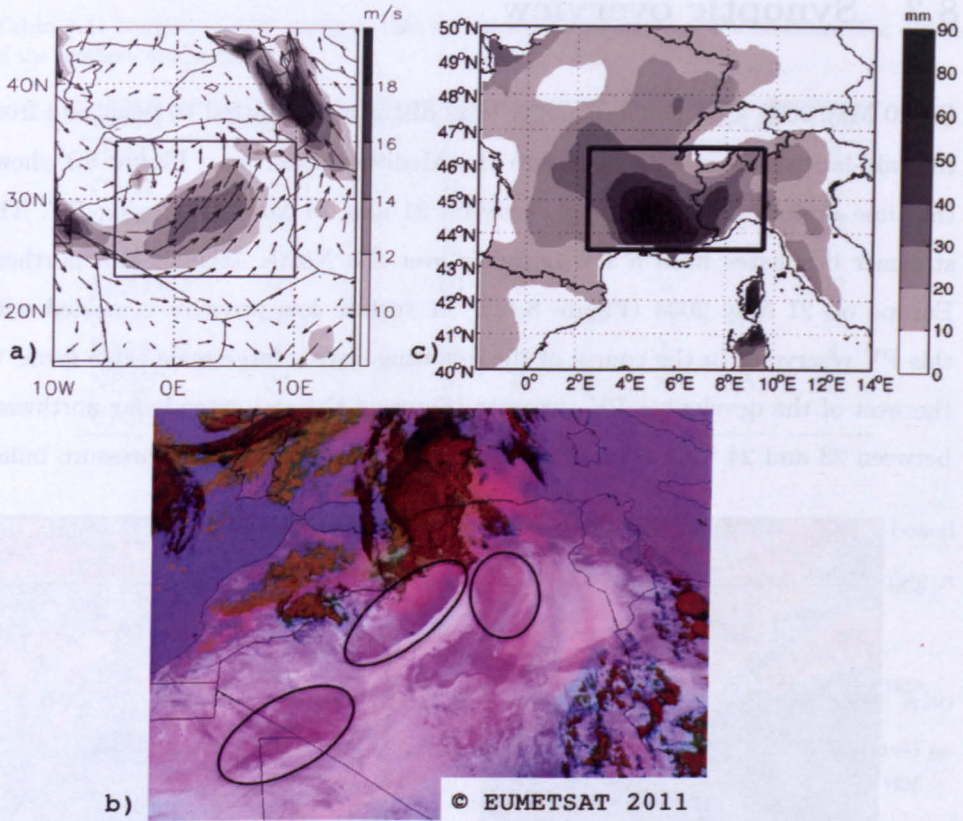


Figure 8.2: High-impact weather caused by the PV streamer: a) ECMWF analysis of wind at 925 hPa for 1200 UTC 26 May 2008. The black rectangle shows the target area used for the investigation of the forecast performance of dust mobilization over the Sahara. b) Dust uplift over the Sahara represented by the SEVIRI dust product (see Section 2.4.2 for more information) at 2000 UTC 26 May 2008. Dust stands out as purple areas over the desert within the black ellipses. The dark reddish areas to the north are clouds ahead of the upper-level PV streamer. c) Observations of accumulated four-day precipitation from 0600 UTC 26 May 2008 to 0600 UTC 30 May 2008. The black rectangle shows the target area used for the investigation of the precipitation forecast performance.

under the ridge during this period. The PV streamer is situated between two strong ridges forming a remarkable 'double'-Omega situation. After 24 May 2008 the PV streamer elongates and reaches its southern-most extension on 26 May 2008 (Figure 8.1d). At this time a surface low forms in the lee of the Atlas to the southeast of the PV streamer.

The associated strong surface winds over the northern Sahara caused widespread dust mobilization and subsequent transport across the Mediterranean Sea and Italy

into central Europe. Figure 8.2a shows the ECMWF analysis of 925 hPa winds at 1200 UTC 26 May 2008. The black box defines a region of high winds over the Saharan desert with values of up to 18 m s^{-1} . Satellite images during this time period clearly indicate substantial dust emission and transport. As an example Figure 8.2b shows the situation over the Sahara at 2000 UTC 26 May 2008. Substantial dust uplift occurred at the Algerian border to Mali and Mauritania, to the south of the Algerian and Moroccan Atlas Mountains and over NE Algeria. Some of this dust was transported northward ahead of the PV streamer and caused a significant dust episode in Germany (Klein et al., 2010). In addition, the strong southerly flow associated with the PV streamer produced heavy precipitation and flooding at the windward side of the Alps. Figure 8.2c shows the four-day (0600 UTC 26 May to 0600 UTC 30 May 2008) accumulated observed precipitation over the Alpine area. According to Meteonetwork and ARPA Piemonte (2008) some regions in southern Switzerland and northern Italy recorded daily accumulations of over 100 mm within this time period. The maximum is clearly seen within this area and south-east France in Figure 8.2c. The black rectangular box is used for TIGGE forecast performance investigations in Section 8.5.3. The heavy precipitation event began on 23 May and the saturated soil received more precipitation starting on 26 and continuing on 27 and 28 May. According to MeteoSwiss the rapid run-off resulted in flooding on the Alpine south side of Switzerland and Italy, causing Lake Maggiore to rise by 63 cm in just four days (Federal Office for the Environment, Swiss Confederation, 2010).

8.4 Forecast performance of large-scale evolution

This section discusses the upper-level development and PV streamer formation in the TIGGE forecast models during this case. A particular focus is on the region of strong southerly flow from the Sahara across the Mediterranean Sea.

8.4.1 Area-mean error measures

Figure 8.3 shows spaghetti plots of the ensemble-mean 1.5 PVU contours for seven lead times and four selected TIGGE models. In general the PV streamer shortens with increasing lead time in all models with cut-offs occurring in the BoM, ECMWF and NCEP models. Strongest deviations between lead times are found within the upstream ridge indicating limited predictability. There is some correlation between the amplitudes of the upstream ridge and the PV streamer when comparing different lead times. Former studies have shown that the western side of high-amplitude ridges over the North Atlantic is often characterised by intense latent heating (Massacand et al., 2001; Knippertz and Martin, 2007). The large spread

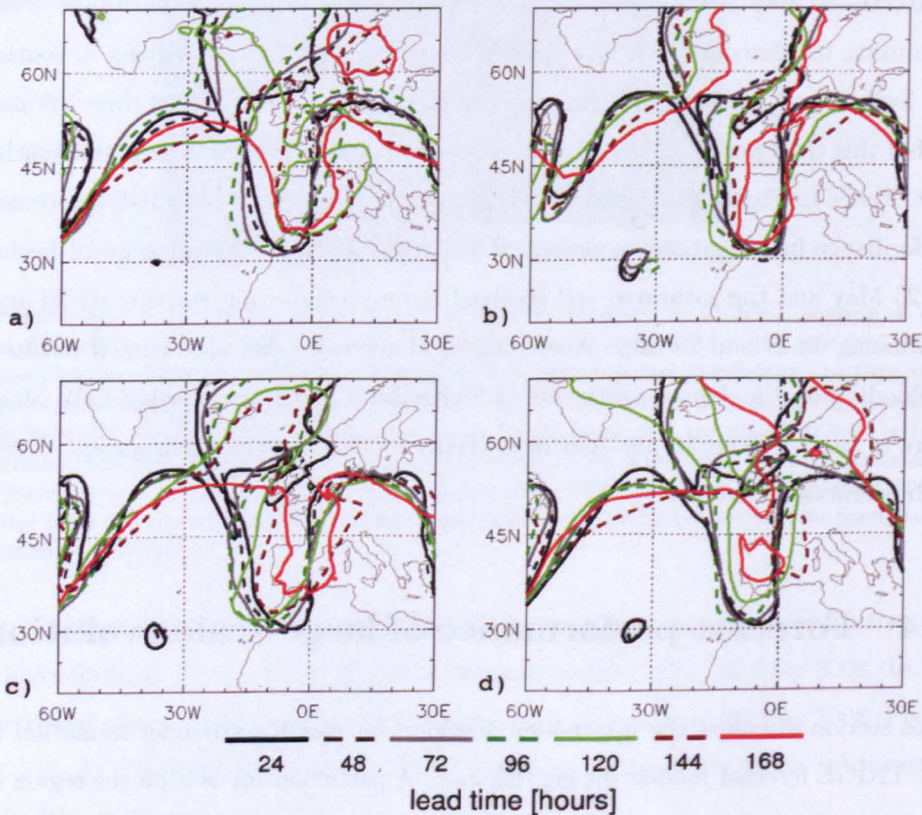


Figure 8.3: Forecast ensemble-mean 1.5 PVU contours of PV for seven lead times (see legend) and four TIGGE centres: a) BoM, b) ECMWF, c) JMA and d) NCEP. Forecasts are valid at 1200 UTC 26 May 2008 (see Figure 8.1d for comparison).

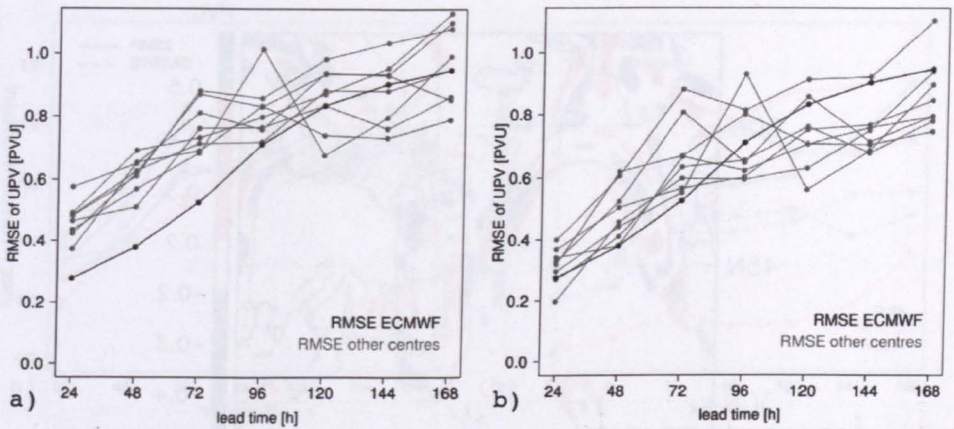


Figure 8.4: RMSE of ensemble-mean PV averaged over the target area (29°N - 55°N , 15°W - 2°E ; see Figure 8.1d) for each TIGGE centre. Forecasts are valid at 1200 UTC 26 May 2008 and have lead times between 24 h and 168 h. RMSEs are calculated with respect to a) ECMWF analyses and b) each centre's own analysis.

between models and lead times suggests that the models are sensitive to this process in this situation.

To investigate the forecast performance two complementary error measures (cf. Section 8.2) were applied to the TIGGE ensemble forecasts. For RMSE computations a target area around the PV streamer under study was defined as 29° - 55°N , 15°W - 2°E (black box in Figure 8.1d). The spatially averaged PV (grid point average) within this box amounts to 1.45 PVU in the ECMWF analysis. Figure 8.4 shows results for one to seven day forecasts of PV valid at 1200 UTC 26 May 2008 (see Figure 8.1d). RMSEs were calculated for ensemble-mean PV with respect to the ECMWF analysis and each centre's own analysis, respectively. Not surprisingly, RMSEs grow with lead time in all models irrespective of which analysis is taken. Using the ECMWF analysis as the 'truth' (Figure 8.4a), the ECMWF model clearly shows the best performance for one to four day forecasts and RMSEs of the same magnitude as the other models for longer lead times. When using each centre's own analysis instead (Fig 8.4b), a substantial decrease in RMSE is apparent for all models. The ECMWF forecast results are still slightly better than those of the other models for short lead times but for longer lead times ECMWF performs less

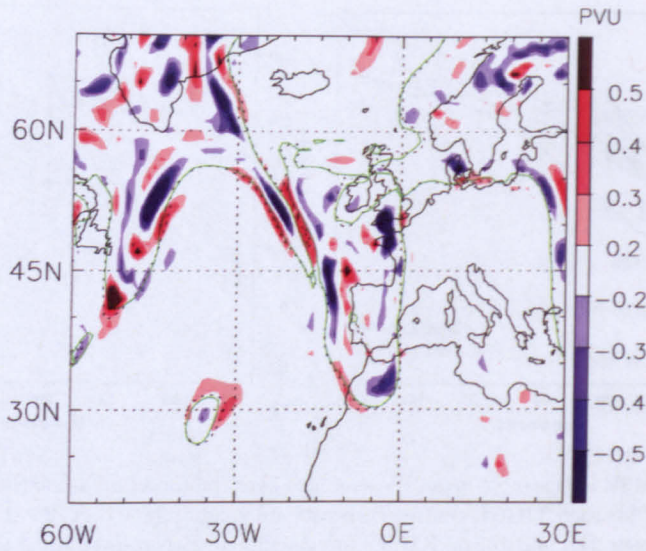


Figure 8.5: Difference between UKMO and ECMWF PV analysis fields at 1200 UTC 26 May 2008. Positive values indicate larger UKMO PV. The dotted black line defines the 1.5 PVU contour line from the ECMWF analysis and the solid green line the 1.5 PVU line of UKMO.

well. To investigate the variability of the PV fields under consideration, calculations of PV standard deviations over the box for all models and lead times have been calculated. They result in similar values for all models and a general decrease with increasing lead time. The result can be seen in Figure A.11 in Appendix A. Therefore it can be excluded that models get penalised by the RMSE calculations (which favour smooth fields) for having more structure in their forecasts.

The increase in RMSE when using ECMWF analysis instead of the centre's own analysis amounts to 40% for some models and longer lead times (72 h-168 h). In the 48 h forecast RMSEs increase between 6% (NCEP) and 60% (KMA). In the very short range forecast (24 h) the increase covers a range for 17% (NCEP) to 75% (JMA, CMA) with an outlier of 150% by the BoM model. The NCEP model shows the smallest RMSE variations between the different calculation methods, indicating that NCEP and ECMWF analyses are more alike than the others.

To explore this further, differences of every TIGGE centre's analysis with the ECMWF analysis were calculated. In Figure 8.5 the difference between UKMO and ECMWF analysis is shown as an example. The largest deviations between the

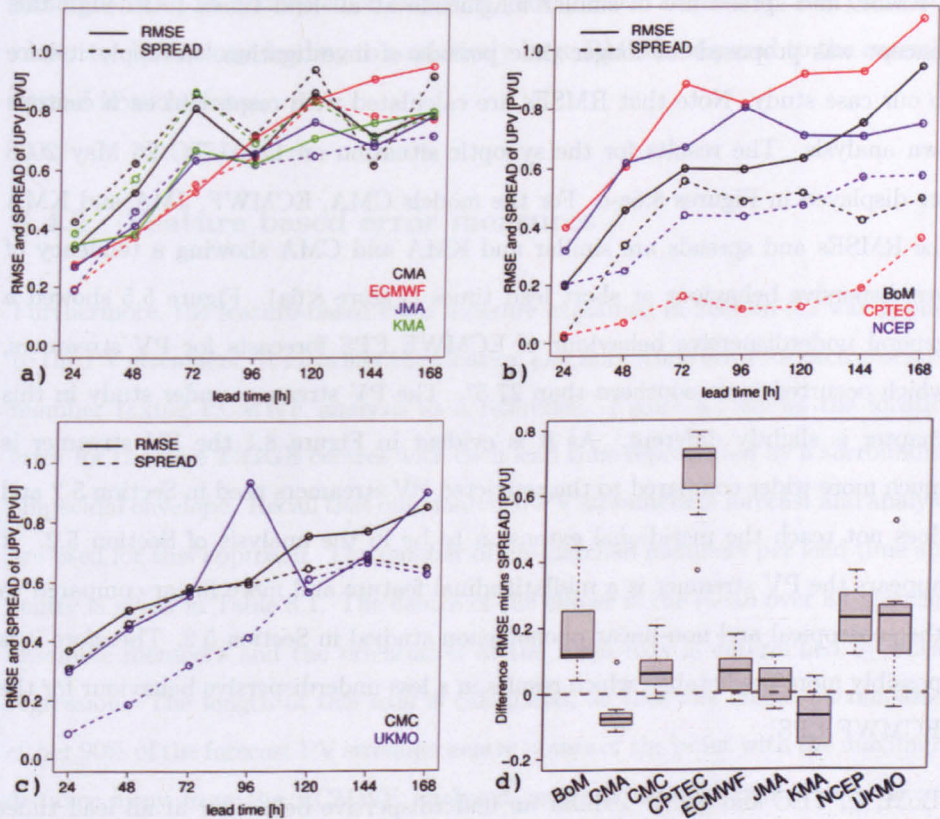


Figure 8.6: RMSE as in Figure 8.4b (solid lines) together with the corresponding ensemble SPREAD (standard deviation, dashed lines) for a) non-dispersive, b) under-dispersive, c) inconclusive (details see Section 8.4.1) behaviour of TIGGE models. d) Difference of RMSE and SPREAD accumulated over all lead times for each TIGGE centre. Forecasts are valid at 1200 UTC 26 May 2008 and have lead times between 24 h and 168 h.

two analysis fields are found in the vicinity of the strongest PV gradients (compare with Figure 8.1d) where values reach up to 1.5 PVU. This is not surprising because small displacements or amplitude errors of PV structures in areas of high gradients can lead to large differences. Comparing short-term forecasts with analysis fields, Dirren et al. (2003) found largest error growth near the jet stream (areas with strongest PV gradients) with some structural similarities to Figure 8.5.

To test whether the TIGGE systems are under- or overdispersive the ensemble-mean RMSE and the spread (standard deviation of all ensemble members) can be compared (Buizza et al., 2005). An ensemble is well designed and reliable,

if RMSE and spread are of similar magnitude at all lead times. Although this concept was proposed for longer time periods of investigation, we apply it here to our case study. Note that RMSEs are calculated with respect to each centre's own analysis. The results for the synoptic situation on 1200 UTC 26 May 2008 are displayed in Figures 8.6a-c. For the models CMA, ECMWF, JMA and KMA the RMSEs and spreads are similar and KMA and CMA showing a tendency of overdispersive behaviour at short lead times (Figure 8.6a). Figure 5.5 showed a general underdispersive behaviour of ECMWF EPS forecasts for PV streamers, which occurred more southern than 27.5° . The PV streamer under study in this chapter is slightly different. As it is evident in Figure 8.1 the PV streamer is much more wider compared to the restricted PV streamers used in Section 5.2 and does not reach the meridional extension to be in the analysis of Section 5.2. It appears the PV streamer is a midlatitudinal feature and more linear compared to the subtropical and non-linear phenomenon studied in Section 5.2. Therefore it is possibly more predictable, which results in a less underdispersive behaviour for the ECMWF EPS.

BoM, CPTEC and NCEP exhibit an underdispersive behaviour at all lead times (Figure 8.6b). The remaining models CMC and UKMO show changes with lead times (Figure 8.6c). CMC is reliable until lead time 96 h but then becomes underdispersive. UKMO is strongly underdispersive except for lead times 120 h and 144 h. A summary view of the model dispersion is presented in Figure 8.6d, where the distribution of the differences, RMSE minus spread, is displayed for all seven lead times in form of box-and-whisker plots. For a well-designed model, the mean difference should not be significantly different from zero. Although the sample size is rather small and the data are not independent, formal tests (Wilcoxon rank sum test and sign test) have been applied to get a quantitative indication of the model behaviour. These tests confirm the visual impression from Figures 8.6a-c: significant differences are found for BoM, CPTEC and NCEP in both tests. For CMC and UKMO the results of the formal tests are inconclusive, probably due to the small sample size and the large variability in the data. In the interpretation of these results the extreme nature of the investigated case has to be kept in mind. Models

generally tend to underpredict extremes (Toth, 1992; Ziehmann, 2001) and stay closer to climatology, leading to a relatively large RMSE compared to the ensemble spread in such a case.

8.4.2 Feature based error measures

Furthermore, the feature-based error measure explained in Section 8.2 was applied to the PV streamers. It identifies the location and amplitude error for each ensemble member taking ECMWF analysis as a reference. Figure 8.7 shows the location error for the nine TIGGE centres with each lead time represented by a surrounding ellipsoidal envelope. Recall that only matched PV streamers in forecast and analysis are used for this approach. The number of un-matched members per lead time and centre is given in Table 8.1. The centre of the ellipse is the mean over all matched ensemble members and the orientation of the main axis is determined by linear regression. The length of this axis is calculated, so that the ellipse encompasses either 90% of the forecast PV streamer centre points or the point with the maximum distance away from the ECMWF analysed centre is reached (which ever occurs first). In this way, the ellipses are sensitive to outliers in order to represent the range of forecasts. The standard deviation of the distance between the forecast PV streamer centre points and the centre point of the ECMWF analysis PV streamer gives the ratio of the major to the minor axis.

The results show a small spread for all centres at short lead times (light grey colours) and a slight northward shift. The spread does not increase substantially over the first four forecasting days and larger spreads are found from the 120 h forecasts onwards for all models. This coincides with the increase in the number of non-matched members in the 120 h, 144 h and 168 h forecasts (as shown in Table 8.1). The non-matched members are due to (A) cut-offs, (B) wide stratospheric troughs, which do not fulfil the PV streamer definition (see Section 8.2), or (C) no stratospheric disturbance at all. Type C applies in half of the cases for the 144 h and 168 h non-matches for CMA, CMC and NCEP, and in one third of the cases for UKMO. The BoM non-matched members all fall into group A and the lack

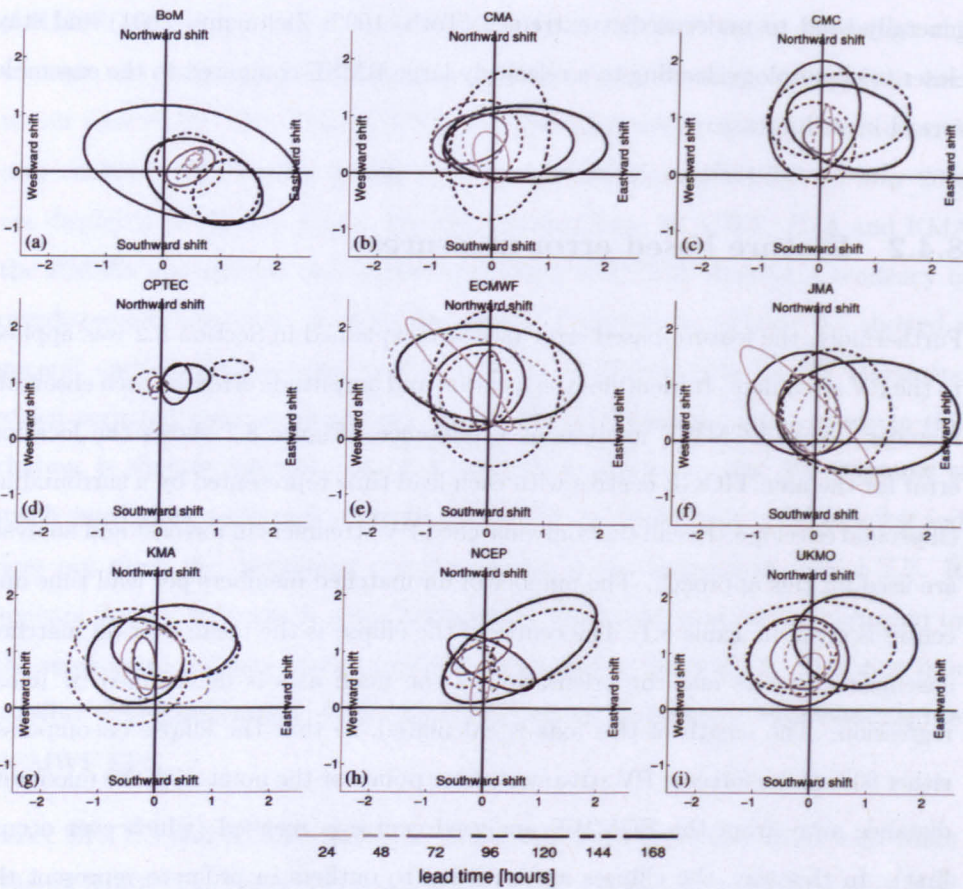


Figure 8.7: Position error (in 1000 km) of the PV streamer ensemble forecasts based on PV (see Section 8.2 for definition) from nine TIGGE forecast centres (indicated in each panel). Ellipses surround position forecasts from all members for 1200 UTC 26 May 2008 (see Figure 8.1d). Gray shading indicates lead time ranging from 24 h to 168 h (see legend). Centre of the coordinate system is the PV streamer position as analysed by ECMWF in all panels.

of spread in the CPTEC model coincides with few non-matched cases. With lead times decreasing from 96 h to 24 h, most of the members belong to group A, and the position and size of the cut-offs get closer to that of the PV streamer. This is also the case for the JMA, KMA and ECMWF models. The five non-matched members in the 24 h forecast for ECMWF coincide with cut-offs that are very similar in size and structure to the analysed PV streamer with only a thin gap to the main body of stratospheric air. The JMA, KMA and ECMWF models all show a much wider range of ensemble spread throughout all lead times. The structure of the stratosphere-troposphere interface often differs completely to that in the analysis

for the 144 h and 168 h forecasts for JMA and ECMWF. The northward shift in most models suggests that the amplitude of the Rossby wave is too small and/or the RWB too weak.

8.5 High-impact weather

Building on the results of the forecast performance for upper levels, this section investigates how TIGGE models forecast the meteorological fields that are important for high-impact weather, in this case dust mobilization and heavy precipitation. The section is divided in four parts. Starting with an analysis of the predicted potential dust uplift (PDU) based on low-level winds over the Sahara, it continues with a correlation between PDU and PV, followed by an investigation of the predicted precipitation and its relation to PV forecasts.

8.5.1 Dust mobilization

As pointed out in Section 8.3, large amounts of dust were lifted over the northern Sahara and carried into Europe in connection with the PV streamer under study. As the TIGGE models do not provide information on surface stress and soil characteristics, we will use a simple diagnostic parameter that reflects the essence of the physical dependency of dust emission on wind speed based on the widely used dust uplift parametrisation by Marticorena and Bergametti (1995). If we, for the sake of simplicity, assume a homogeneous soil with a constant emission threshold and approximate the surface stress or friction velocity by its first-order control low-level wind speed U , we can define a variable called PDU in the following way:

$$PDU = \begin{cases} U^3(1 + \frac{U_t}{U})(1 - \frac{U_t^2}{U^2}) & \text{for } U > 10 \text{ m s}^{-1} \\ 0 & \text{for } U < 10 \text{ m s}^{-1} \end{cases} \quad (8.2)$$

where U_t denotes the constant threshold velocity that is typically on the order of 8 m s^{-1} at 10 m above the ground (Chomette et al., 1999). As 10 m winds are not a

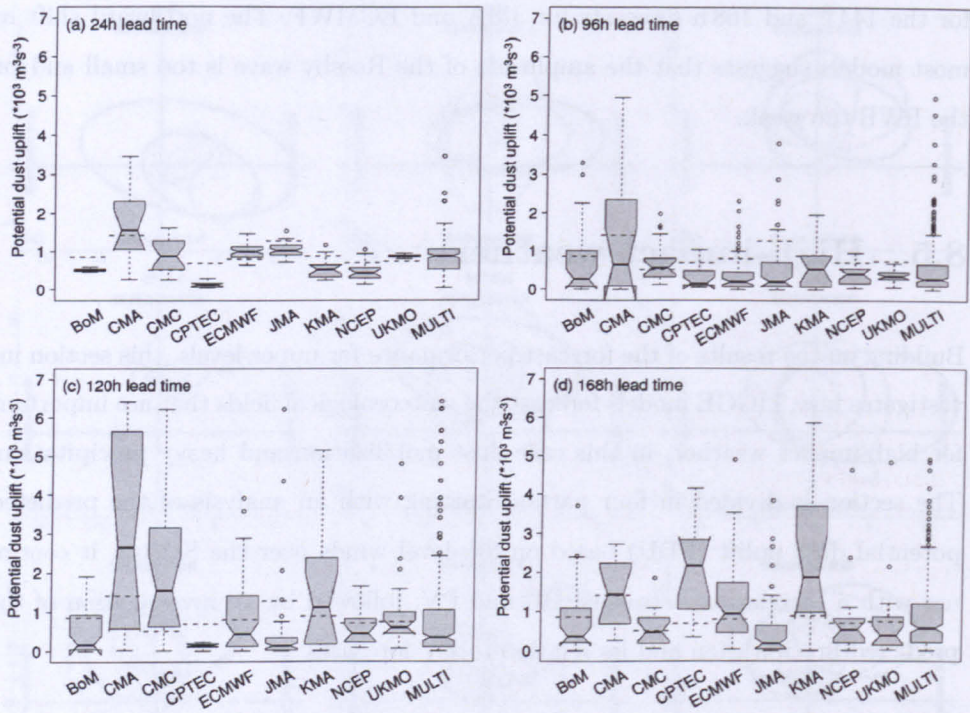


Figure 8.8: Potential dust uplift ($10^3 \text{ m}^3 \text{ s}^{-3}$ PDU, see Section 8.5.1 for definition) averaged over the box 23°N - 35°N , 5°W - 10°E from each TIGGE centre and the multi-model ensemble including all TIGGE members. a) 24 h, b) 96 h, c) 120 h and d) 168 h forecast for 1200 UTC 26 May 2008. The dashed grey lines indicate the PDU analysis from each TIGGE centre. Box-and-whisker plots are defined with the upper and lower border of the grey box as the 1st and 3rd quartile, the black line within the box is the median, the whiskers on both sides are the minimum and maximum and the blank circles are outliers. The notches on the boxes indicate that the medians of two box plots are significantly different when notches do not overlap.

prognostic variable in TIGGE models, it has to be computed through extrapolation from the lowest model level using parameters from the boundary layer scheme. The details of this procedure can lead to dramatic differences in low-level wind speeds (see e.g. Schwierz et al., 2010). To avoid that the differences between the models being dominated by the effects of parametrisations, wind speed at 925 hPa was used as a robust estimate for the flow in the boundary layer over Africa with U_t set to 10 m s^{-1} . In principle, it would be desirable to evaluate wind direction as well, but for the sake of simplicity the authors decided to concentrate on the main atmospheric control on dust emission, i.e. wind speed.

Figure 8.8 displays PDU averaged over the target box shown in Figure 2a for the

nine TIGGE ensemble systems in the form of box-and-whisker plots. The size of the boxes is indicative of the ensemble spread (see caption). The dashed lines show PDU values computed from each centre's analysis. The large range from $0.52 \cdot 10^3 \text{ m}^3 \text{ s}^{-3}$ to $1.43 \cdot 10^3 \text{ m}^3 \text{ s}^{-3}$ is a reflection of differences between the individual analyses as already discussed in Section 8.4.1 and of the highly non-linear relation between dust emission and wind speed (essentially a cubic dependence).

The 24 h forecasts (Figure 8.8a) show a number of different behaviours of the ensemble systems. CPTEC and BoM have a very low spread and clearly underpredict PDU, while UKMO shows an equally small spread with a slight overprediction. CMA stands out as the model with the largest spread and the highest median and analysed PDU. CMC has also a large spread, but the lowest analysed PDU and a median close to most of the other models. Intermediate spreads that contain the analysed values are found for ECMWF, JMA, KMA and NCEP, of which with the latter three's median clearly underpredict PDU over the Sahara. The multi-model box-and-whisker plot including all TIGGE members has a median exactly in the range of the analysed values demonstrating the added value of a multi-model approach. This also holds for 48 h and 72 h forecasts (not shown).

The 96 h PDU forecasts (Figure 8.8b) show a marked increase in spread and a general tendency to underpredict with most medians well below the analysed PDU including the multi-model one. UKMO is the only model where the analysed value is outside of the (rather small) ensemble spread. For the 120 h PDU predictions (Fig 8.8c) the spread continues to increase for most ensemble systems and comprises the analysed PDU for all models but CPTEC, which simulates hardly any wind speeds above the emission threshold. Out of the remaining eight models, five show an underprediction. CMA, CMC and KMA show the largest spreads and tend to overpredict the analysed PDU. Interestingly, several ensemble systems have members with rather extreme PDUs on the order of five times the analysis value.

For the longest lead time of 168 h (Figure 8.8d), all models contain the analysis in their ensemble spread, which does not increase much more beyond the 120 h forecasts. Compared to some of the shorter lead times, the number of members

lying within the range of analysed PDUs have increased in all models except for UKMO (decreased median) and KMA (higher PDU in total). Especially CMA and CMC show a good forecast with the median matching their own analysis exactly. Even CPTEC shows a potential to lift dust in contrast to shorter lead times. This is reflected in the multi-model box-and-whisker plot, too, which has a higher median value for 168 h than for 96 h and 120 h PDU multi-model forecast median. Given the degradation of the PV streamer forecast with lead time discussed in Section 8.4, it is conceivable that the overall satisfactory quality of the 168 h forecasts could be at least partly due to wrong physical reasons. This point will be discussed further below (see Section 8.5.2).

In conclusion, there is a general tendency of the TIGGE models to underpredict PDU for all lead times, but there are at least some members indicating possible dust mobilization in nearly every forecast. There is a non-monotonic relationship between forecast quality and lead time with overall large variations in both median and spread between the modelling systems. The multi-model approach improves the forecast at most lead times. One general problem for the verification is the surprisingly large difference between the model analyses.

8.5.2 Ensemble correlation of dust and PV

This section takes a more detailed look at the relationship between the PDU over the Sahara and the upper-level circulation using an ensemble correlation technique. The technique is introduced in Section 6.1. In Chapter 6 precursors in early forecasts in different meteorological variables are studied, which influence the medium-range PV streamer forecast. Here, in contrast to Chapter 6, the ensemble correlation is used to examine, which forecast PV streamer shape and location supports dust uplift over the Sahara in the same forecast step. Hereafter the linear

correlation coefficient r is calculated using Equation 8.3

$$r(PV_{i,j}^t, PDU^t) = \frac{\frac{1}{N-1} \sum_{n=1}^N \left({}^n PV_{i,j}^t - \overline{PV}_{i,j}^t \right) \left({}^n PDU^t - \overline{PDU}^t \right)}{\left[\frac{1}{N-1} \sum_{n=1}^N \left({}^n PV_{i,j}^t - \overline{PV}_{i,j}^t \right)^2 \right]^{\frac{1}{2}} \left[\frac{1}{N-1} \sum_{n=1}^N \left({}^n PDU^t - \overline{PDU}^t \right)^2 \right]^{\frac{1}{2}}}, \quad (8.3)$$

where PDU^t is the box average (see Figure 8.2a) of PDU as defined in Section 8.5.1 at lead time t . N is the number of EPS members (different for every centre). The PDU values are correlated with PV at every grid point (i, j) predicted for the same lead time t . Four exemplary results are shown in Figure 8.9 where shadings indicate positive (negative) correlation in dark grey (light grey). A positive (negative) value of r at point (i, j) implies that PDU in the box over the Sahara and PV values at point (i, j) tend to deviate in the same (opposite) direction from the ensemble mean. The ensemble-mean 1.5 PVU line is included for reference. The top (bottom) panels in Figure 8.9 display results from NCEP (ECMWF) forecasts. The left column shows correlations over all seven lead times ($N = 7 * \text{number of EPS members}$) and the right column shows one lead time only (48 h for NCEP and 72 h for ECMWF).

The results for all NCEP forecasts (Figure 8.9a) show a strong correlation within the ensemble-mean PV streamer and to south-east of its tip. Negative correlations are evident in the upstream and downstream ridges. This suggests that the PDU over the Sahara is closely related to the amplitude of the Rossby wave and the southward extension of the PV streamer. Together with the negative correlations over the Sahara this leads to a stronger PV gradient across the box, which induces a stronger southwesterly flow. Looking at individual members with particularly high and low PDU indicates that the former are characterised by a thinner PV streamer than analysed reaching 30° latitude with an enhanced ridge upstream, while the latter tend to show PV cut-offs and a relatively weak ridge upstream. Similar results are found for UKMO, KMA and BoM, although the negative correlations to the west of the PV streamer are smaller in these models.

An example for a single lead time is given in Figure 8.9b. Generally the correlation signals show more fine-scale structure and are somewhat more concentrated around

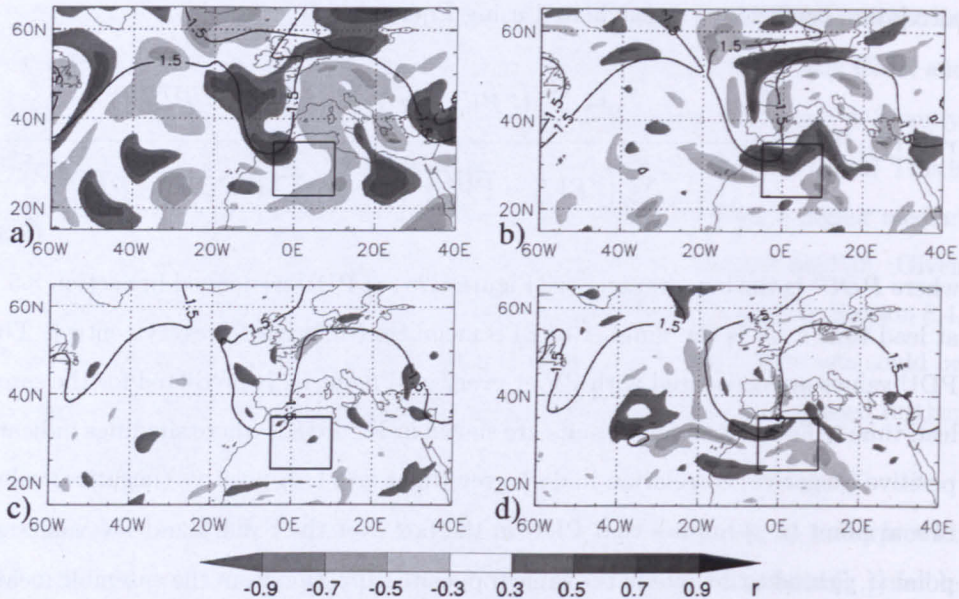


Figure 8.9: Correlation coefficients (grey shading) between the predicted PDU in a box over the Sahara (black rectangle) and predicted PV at every grid point, both valid at 1200 UTC 26 May. a) all lead time forecasts (24-168 h) from NCEP, b) 48 h forecast from NCEP, c) all lead time forecasts from ECMWF and d) 72 h forecast from ECMWF. Black lines are the ensemble mean 1.5 PVU contour line from the respective centre at the respective lead time(s).

the PV streamer than in Figure 8.9a. Indications for a thinning and southward extension are very clear for this lead time with positive values extending well across northern Algeria. This pattern together with negative values over Spain and France occurs for many models and lead times, and is indicative of a so-called treble clef structure resulting from cyclonic role-up and diabatic reduction of PV (Appenzeller et al., 1996; Martin, 2006).

Analogous analyses for other TIGGE models indicate a less clear connection between PV and PDU. For all lead times combined, correlations are generally weak for ECMWF (Figure 8.9c), while the JMA, CMA and CMC models show at least weakly positive correlations within the PV streamer, and the CPTEC model shows negative correlations in the area of the upstream ridge (not shown). For individual lead times, however, some coherent signals can be identified for the ECMWF model such as an enhanced PV gradient across the box (Figure 8.9d). Looking at individual forecasts for these TIGGE models confirms that similar PV streamer

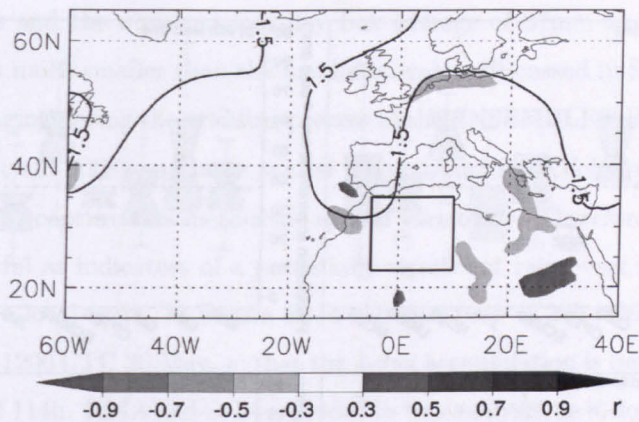


Figure 8.10: Same as Figure 8.9 but for 72 h forecasts from all TIGGE members.

forecasts can produce both low and high PDU values over the Sahara (see Figures A.12 and A.13 in Appendix A). This indicates that other processes such as vertical stability modify the physical link between the intensity of the PV streamer and the low-level winds. A detailed investigation of this interesting aspect is beyond the scope of this case study, but should be borne in mind in future application of ensemble correlation techniques.

A new research approach made possible through TIGGE is to calculate multi-model statistics, which allows distinguishing between inter- and intra-ensemble spread. Here ensemble correlation techniques are applied to all 239 TIGGE members (N in Equation 8.3) for every forecast time step. Figure 8.10 shows the 72 h-lead time correlation of PV and PDU as in Figure 8.9d but for all TIGGE forecasts. Overall correlations are much weaker than for most single-model, single-lead time calculations. This suggests that differences in model formulation have a stronger effect on the low-level wind speed than differences in PV between different members. Most likely different boundary layer formulations play an important role in generating this result.

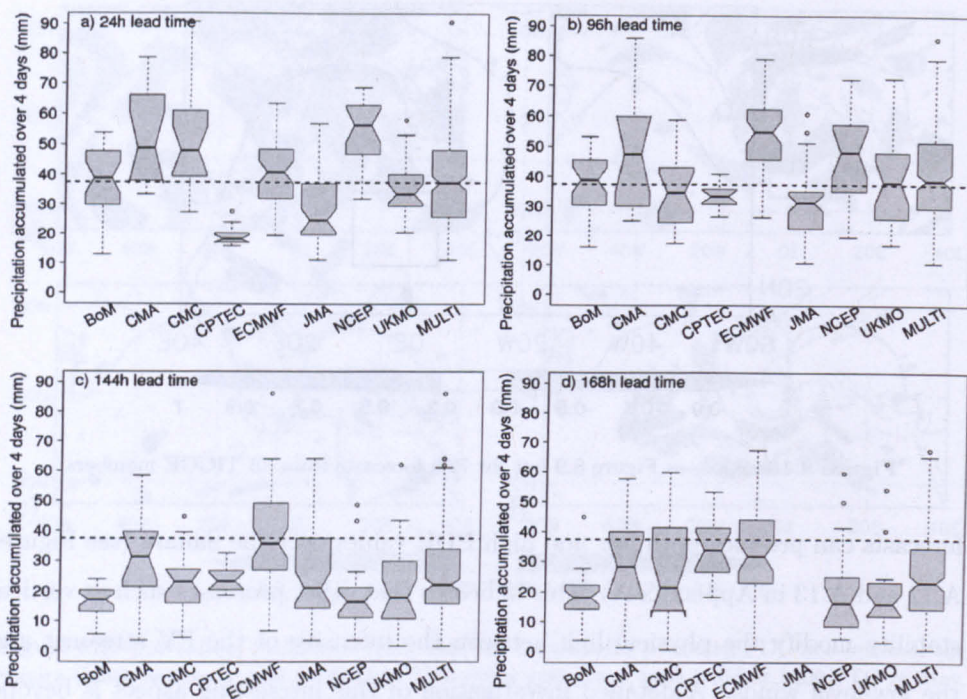


Figure 8.11: Predicted precipitation in mm accumulated over the four-day period 0600 UTC 26 to 0600 UTC 30 May 2008 and averaged over the target box (43.5° - 46.5° N and 2.5° - 9.5° E) from each TIGGE centre and the multi-model ensemble except for KMA (details see Section 8.5.3). Lead times are a) 24 h, b) 48 h, c) 96 h and d) 168 h. The dashed line is the observed value from ENSEMBLES E-OBS. Box-and-whisker plots are defined as in Figure 8.8

8.5.3 Precipitation

A similar analysis to Section 8.5.1 is conducted for the heavy rainfall at the southern side of the Alps based on precipitation accumulated over the period 0600 UTC 26 to 0600 UTC 30 May and averaged over the box from 43.5° - 46.5° N and 2.5° - 9.5° E where the maximum precipitation occurred (see Figure 8.2c). After the southernmost extension of the PV streamer at 26 May (see Figure 8.1), the PV streamer thinned and shifted eastwards until 28 May. Subsequently it rolled up cyclonically resulting in a PV cut-off over the Alps at 30 May 2008. The cut-off was then approached by a new PV streamer from the northwest, which however did not reach the large southern extension of the previous PV streamer.

In analogy to Figure 8.8, Figure 8.11 shows box-and-whisker plots of predicted

precipitation and the observed four-day box average of 37mm as a dashed line. This value is much smaller than the maximum-values discussed in Section 8.2 due to area averaging during the gridding process of the ENSEMBLES data (see details in Haylock et al., 2008) and large spatial inhomogeneities. Global models cannot be expected to capture this meso-scale spatial variability. Therefore the forecasts are more useful as indicators of a potentially significant rain event than for flood warnings on a local scale. In Figure 8.11a the lead time of 24h refers to forecasts initialised at 1200 UTC 25 May, so that the 4-day accumulation is between forecast steps 18h and 114h. KMA had to be excluded in this analysis, as it does not provide precipitation data. JMA could not be investigated for all lead times because of a lack of precipitation forecasts longer than 240 h.

The 24 h (Figure 8.11a) and 48 h forecasts (not shown, initialised at 1200 UTC 24 May, accumulated between forecast times 42 h to 138 h) are very similar and show a relatively large spread but a good scatter around the observed value. The most skillful short-range forecasts are provided by BOM, ECMWF and UKMO with the median close to the observed rainfall. CMA, CMC and NCEP slightly overpredict the average rainfall while JMA has lower rainfall averages than those observed. CPTEC has a very low spread and significantly underpredicts the rainfall. The forecasts from this model improve over time (although still underpredicting the average rainfall) up to the 96 h forecast (cf. Figure 8.11b). The multi-model box-and-whisker plot including all TIGGE member forecasts for this lead time shows a remarkably good performance with its median exactly on the observed 37 mm. The same multi-model behaviour can be seen across the whole short-range up to 96 h. The 72 h and 96 h forecasts are again similar for each model centre with several of the models showing skillful predictions. BoM and UKMO perform best with regard to the median rainfall.

A view at the longer range forecasts (120 h to 168 h) shows a small over-prediction of CPTEC and ECMWF (120 h), while the BoM model notably changes in skill and underpredicts the average rainfall considerably (120 h to 168 h). In the 144 h forecast (Figure 8.11c) the spread decreases somewhat in contrast to the increasing spread in PV (see Section 8.4.1). ECMWF performs best for this lead time but all

the centres' medians are below the observed precipitation as shown by the multi-model result. This continues for the 168 h forecast (Figure 8.11d) with all centres underpredicting the precipitation and BoM, NCEP and UKMO having the lowest and CMA, CPTEC and ECMWF the highest medians.

The most notable changes with lead time occur for the UKMO and BoM models which show good skill for forecast times up to four days and significant decreases beyond this. ECMWF has the most consistent forecasts with accurate short-range (24 h to 72 h) and medium-range prediction (144 h to 168 h). Twenty four to ninety six hour multi-mode forecasts give an overall satisfactory representation of the event and could be used for severe weather warnings. Similarly, exceptionally good predictions of heavy precipitation events on the Alpine south side in general was shown for instance in Jenkner et al. (2008) for the meso-scale model COSMO.

8.5.4 Ensemble correlation of precipitation and PV

The correlation technique explained in Section 8.5.2 has also been applied to PV and box-averaged four-day accumulated precipitation (0600 UTC 26 May 2008 to 0600 UTC 30 May 2008). Lead time for PV is defined with respect to 1200 UTC 26 May 2008. Correlations were also calculated for PV in the middle of the precipitation period, i.e. 28 May 2008, but results are quite similar with even smaller signals in some areas. Single model and single time step correlations resulted in overall lower values compared to the PDU and PV correlations shown in Figures 8.9b and 8.9d. This might be caused to some extent by the relatively long accumulation period used for precipitation. A feature evident for most models and lead times is a dipole of positive correlations at the western side of the PV streamer and negative correlations further east. This highlights the importance of high PV in the western vicinity (France and northern Spain) of the Alpine south side to produce a high amount of precipitation in the following days (cf. also Martius et al., 2006).

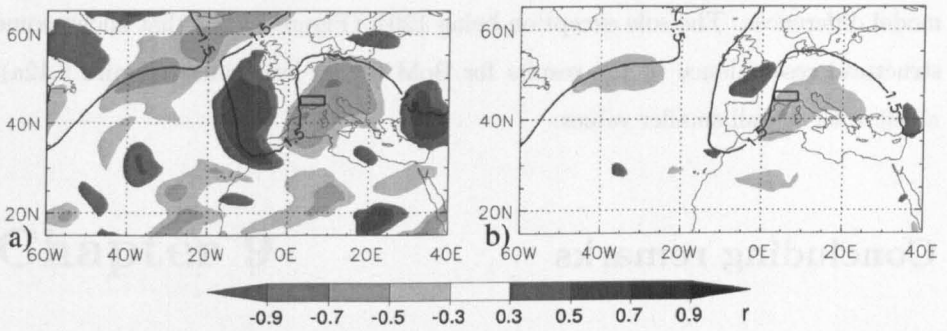


Figure 8.12: Correlation coefficients (grey shading) between the predicted four-day accumulation of precipitation valid from 0600 UTC 26 May to 0600 UTC 30 May in a box over the Alpine south side (black rectangle) and predicted PV at every grid point valid at 1200 UTC 26 May for a) all lead time forecasts (24-168 h) from BoM and b) the 120 h forecasts from all TIGGE members. Black lines are the ensemble-mean 1.5 PVU contour lines over a) all lead times and b) all TIGGE members.

As an example Figure 8.12a shows correlations over all lead times for the BoM model. The results exhibit negative correlations within the downstream and upstream ridge and positive values within the PV streamer itself, particularly on the western side. Some indications for cyclonic roll-up are evident in the shape of the correlation pattern over northwestern Africa. The dipole indicates that fast moving PV streamers (high values over Italy and Central Europe and low values over the Iberian Peninsula) are associated with too low precipitation over the Alps and vice versa. Looking at the driest and wettest individual forecasts confirms this. Dry members are also more oriented in a northeast-southwest direction. The comparison of dry and wet member forecasts can be seen in Figure A.14 in Appendix A.

Furthermore, again the negative correlations in the upstream ridge are most likely a reflection of the role of diabatic processes for the amplification of the wave and the subsequent breaking (cf. Figure 8.3), while negative values downstream indicate a more effective blocking that slows the propagation of the PV streamer.

For most other models correlation over all lead times are small, indicating the presence of different PV-precipitation relationship that cancel out when all lead times are combined. Correlations for all models at individual lead times are also rather small as found for PDU and PV in Section 8.5.2, pointing to substantial

model differences. The sole exception being 120 h (Figure 8.12b) that shows some structural resemblance to the results for BoM for all lead times (Figure 8.12a), albeit with overall smaller values.

Concluding remarks

The past chapter analysed forecasts from nine EPSs archived in the TIGGE database for the case of a pronounced PV streamer over the Mediterranean Sea that produced a combination of severe weather events including a Saharan dust storm and flooding in the southwestern European Alps. Different analysis techniques were used to investigate the forecast quality and predictability of the PV streamer. RMSE and spread comparisons showed a non-dispersive behaviour for four models, an under-dispersive behaviour for three models and two inconclusive models. Furthermore large differences between analysis fields in several model variables were recognized. A feature-based verification algorithm detected a general northward shift of the forecast PV streamer. Potential dust uplift verification showed a general tendency of underpredicting peak low-level winds. Precipitation forecasts of the TIGGE models yield good four-day accumulated precipitation forecasts at short lead times (1-4 days) with decreasing skill for longer lead times except for ECMWF. For both parameters (potential dust uplift and precipitation) a multi-model approach proves beneficial for most lead times.

Chapter 9

Conclusions

9.1 Summary

This thesis is one of the first studies to systematically explore the huge dynamical information content of long-term data from ensemble prediction systems. Specially, data from the ECMWF operational EPS for statistical analyses and the TIGGE ensembles for a case study have been evaluated.

The atmospheric focus of this study was upper-level PV streamers that penetrate into low latitudes. As these events occur most frequently over the Mediterranean Sea/Northern Africa in boreal winter, the study was limited to PV streamers in that region and at that time. These zonally narrow and meridionally elongated PV bands can cause high-impact weather in Northern Africa, such as strong precipitation events and dust outbreaks.

The statistical analysis was based on an objective algorithm to detect PV streamers. The algorithm is first applied to operational ECMWF analysis fields to identify dates when PV streamers occur. A tracking algorithm allowed the determination of 75 PV streamer episodes from 1996 to 2008. The EPS forecasts for these events at lead times from 24 h to 240 h were examined.

One objective of this study was an evaluation of the EPS forecast quality. For this, several areas and variables were considered: 1. PV in the area of the analysed streamer, 2. PV in a box around the streamer as well as 3. geopotential height at 500hPa in the same box. A comparison between ensemble spread and RMSEs of the mean forecast calculated with respect to the operational analysis was executed for all 75 PV streamer verification times. In general it was shown that forecasts for these atmospheric features are very underdispersive, especially for longer lead times. Furthermore the comparison showed similar behaviour in the slopes of the RMSE and spread curves as function of lead time, as well as a similar gap between spread and RMSE for the variables Z500 and PV.

The forecast quality increased slightly over the years with the exception of a surprising increase of RMSE for the last two years (2007, 2008). The RMSE calculations divided into periods between changes in the EPS system showed a general improvement of the EPS by most modifications. An exception is the implementation of the VAREPS in 2006, after which forecasts of this kind of atmospheric situations deteriorated.

Latitudinal displacements of the forecasts relative to the verifying analysis showed one possible reason for poor forecasts. PV streamers in the forecasts tend to be shifted to the northeast, suggesting that the simulation of Rossby wave breaking, leading to too small meridional extension of the PV streamers.

The dynamical causes of ensemble divergence are investigated with correlations between the upper-level disturbance-related PV at verification time and several meteorological fields (e.g. upper tropospheric PV, geopotential height at 500 hPa and 200 hPa, equivalent potential temperature at 850 hPa, vertical wind at 700 hPa) at various lead times. Since every ensemble member is a physically realistic realisation of a possible synoptic evolution, this correlation approach allows a direct assessment of the dynamical prerequisites for PV streamer development and propagation. The results suggest that upstream diabatic processes in early stages of the forecast lead to a stronger PV streamer. Latent heating at the east of the upstream trough, marked by relatively high equivalent potential temperatures at

850 hPa and uplift in the middle troposphere, generates a stronger ridge and consequently amplifies the Rossby wave. This mechanism leads to a more meridional extension of the PV streamer and a deeper intrusion into low latitudes. Blocking events over Europe do not appear to have a dominating influence on the strength of the PV streamer forecast.

An analysis of the relative importance of model errors versus initial conditions for RMSE growth in the EPS was carried out. This analysis showed that forecasts from members with the lowest (highest) RMSEs in the EPS for short-range forecasts (two days) create in general a tendency of lower (higher) errors in the longer lead time (five to seven days) forecast compared to all other members. In general good (bad) short-range forecasts do not decide about good (bad) long-range forecasts. Model errors together with the non-linear behaviour and therefore non-linear error growth determines the atmospheric evolution in the forecast.

Furthermore, a case study was conducted using forecasts from nine ensemble prediction systems archived in the TIGGE database. The focus was a pronounced PV streamer over the Mediterranean Sea that produced a combination of severe weather events, including a Saharan dust storm and flooding in the southwestern European Alps. Different analysis techniques including RMSE and spread comparisons, differences between analysis fields, and a feature-based verification algorithm were used to investigate the forecast quality and predictability of the PV streamer and near-surface wind as well as precipitation. The connection between upper-level features and low-level impacts was investigated with an ensemble correlation technique.

RMSE and ensemble spread calculations based on upper-level PV in the area of the streamer show increasing values with lead time with marked differences depending on the analysis used for reference. Using the ECMWF analysis instead of every centre's own analysis increased RMSEs by up to 75% (60%) in the 24 h (48 h) forecasts. Even in the long-range forecasts (72 h-168 h) RMSE differences up to 40% occur. Intercomparison of analysis fields showed differences of up to 1.5 PVU, mainly in regions of large PV gradients along the mid-latitude jet.

The comparison of RMSE and ensemble spread revealed a tendency towards under- to non-dispersive behaviour of most ensemble systems for this rather extreme case. Results from a feature-based measure that focused on PV streamer location errors indicate a general tendency for a northward shift of the PV streamer in the forecasts. This shift and the ensemble spread for every TIGGE centre are relatively small until lead time 96 h and then increase abruptly indicating a limit of predictability beyond four days for the PV streamer situation under study. The consistent behaviour of all TIGGE models suggests general problems with reproducing the intensity of the wave breaking, resulting in too small wave amplitudes and an insufficient meridional extension of the PV streamer to the south. The agreement in the north (east) shift in the forecasts for the case study and the general study over all 75 PV streamer cases in the ECMWF EPS with different analysis methods shows a strong signal for a consistent error in all NWP models.

Using a new potential dust uplift diagnostic for the Saharan dust storm showed a general tendency of underpredicting peak low-level winds, but a large spread in most ensembles gives at least some indication of a potential for dust mobilization. Ensemble spread and forecast quality are non-monotonic with lead time in contrast to the upper-level features.

Using an ensemble correlation technique the relationship between predicted upper-level PV fields and potential dust uplift was investigated. Ensemble correlations show that a high amplitude Rossby wave and a strong PV gradient over the Sahara are important conditions for low-level winds over the Sahara. Comparing different lead times for single models or different models for single lead times points to the importance of other factors, such as vertical stability and boundary layer parametrisations, modifying the relationship between PV and low-level wind.

Overall, the TIGGE models yield good four-day accumulated precipitation forecasts at short lead times (one to four days), with decreasing skill for longer lead times except for ECMWF. Correlation results showed the importance of a well-forecast PV streamer in time and east-west position to get the right amounts of precipitation at the Alpine south side. Both the upstream and downstream ridges are important

for this. For both parameters (potential dust uplift and precipitation) a multi-model approach proves beneficial for most lead times.

9.2 Discussion

The section above summarises the results found in this study, which are discussed here in the light of other scientific results.

The comparison of RMSE and spread to show the dispersive behaviour of an EPS is a well-known analysis technique. The spread in a perfect ensemble will represent the standard deviation of the ensemble mean forecast error distribution (Leutbecher and Palmer, 2008). Buizza et al. (2005) compared ECMWF, NCEP and Meteorological Society of Canada (MSC) ensembles for spring 2002 and stated that ‘for all three global systems, the spread of ensemble forecasts is insufficient to systematically capture reality, suggesting that none of them is able to simulate all sources of forecast uncertainty.’ This statement illustrates the underdispersive behaviour of these models, which are shown in RMSE and spread of Z500 forecasts averaged over the whole Northern hemisphere. A possible explanation for this lack of spread may be that in the EPS the growth of forecast errors due to model errors is not represented adequately (Leutbecher and Palmer, 2008). In contrast, Park et al. (2008) found a generally well-tuned spread for Z500 averaged in the Northern hemisphere for eight ensemble systems participating in TIGGE. However, the lack of spread in other variables and areas (e.g. THE850 in the Tropics) again leads to an underdispersive behaviour. The results for the PV streamer situations being investigated here largely agree with the studies outlined above. The general underdispersive character of the variable upper-level PV in the ECMWF EPS around the PV streamer area was discovered. In the interpretation of these results the extreme nature of the investigated cases has to be kept in mind. Models generally tend to underpredict extremes and stay closer to climatology (Toth, 1992; Ziehmann, 2001), leading to a relatively large RMSE compared to the ensemble spread.

The ensemble correlation technique performed in Chapter 6 was used for the first time for the particular dynamical situation of upper-level Rossby waves and their breaking. Hawblitzel et al. (2007) introduced this method and used it to find prerequisites in early forecasts for successful forecasts of deep convection over the American continent. Here the focus was on the statistical evaluation of the influence of diabatic heating and blocking events days before the PV streamers occurred. Several studies in the past found a connection of PV streamer development and blocking downstream as well as diabatic processes upstream.

Altenhoff et al. (2008) clearly showed a higher frequency of PV streamer development under blocking conditions. The ensemble correlation gives evidence for a ridge downstream of the PV streamer but the signal appears late in the forecast and is not stationary. According to Schwierz et al. (2004a), blocking is a vertical coherent and quasi-stationary high-pressure system, which disrupt the prevailing westerly circumpolar flow. One property of the ensemble correlation analysis is that it can only detect the influence of a blocking situation on PV streamer strength in single-member forecasts compared to the mean forecast. If the majority of members predict a blocking, which is possibly well-predicted from the EPS in general, the method cannot find any influence on the PV streamer strength. This might well be the case for the ECMWF EPS. Pelly and Hoskins (2003) showed ECMWF EPS forecasts of Euro-Atlantic sector-blocking from August 2000 to July 2001 are skilful relative to the climatology out to ten days. Furthermore, Shakina and Ivanova (2010) stated that blocking duration and decay can be predicted successfully within the medium-range ensemble forecasting system.

The ensemble correlation showed a strong influence of diabatic processes upstream several days before the PV streamer occurred. Massacand et al. (2001) suggested that upstream diabatic heating might be crucial for the development of some real-world PV streamers. Martius et al. (2008) found that upstream mid-tropospheric diabatic heating is a precursor for wave breaking events downstream. The areas of diabatic heating important for PV streamers connected to high-precipitation events at the Alpine south-side change seasonally, depending on wavelength and propagation. Different studies in the past showed that diabatic heating in an extratropical

transition of a hurricane can lead to an amplification of the Rossby wave (e.g. Jones et al., 2003). A detailed look into the correlation results at the location of hurricane occurrences in the time periods of the 75 PV streamers, however, showed no major signal from latent heating. Different seasonality of the two atmospheric phenomena led to hurricane occurrences in just two PV streamer episodes.

9.3 Résumé

This section highlights some of the remarkable, surprising and significant results of this thesis.

The restriction to a small geographic region of PV streamer occurrence (North Africa and south of 27.5°N) was expected to lead to similar atmospheric systems in origin and evolution. In reality a surprisingly large variety was found. Therefore setting statistical robust results summarising the evolution of upper-level systems turned out to be challenging. Recall that, to date, most dynamical studies of PV streamers have been case studies.

Nonetheless, the study developed some original concepts in the fairly new field of ensemble forecast verification and analysis. New techniques, such as ensemble correlation, tested throughout this study appear to be useful tools to identify prerequisites important for a successful forecast several days before the structure under study occurs. Furthermore, it was shown to be useful for the detection of upper-level influence on lower-level feature forecasts, and can therefore be used for identifying model and/or initialisation errors leading to an inaccurate forecast.

The well-known method of comparing spread and RMSE at Z500 to check the dispersive behaviour of the EPS was examined with PV here. The comparison of Z500 and PV showed a similar behaviour, though only for extreme cases and on a more localised scale than the use of whole hemispheres in past studies.

The least expected result is that model error and non-linear error growth leads to stronger medium-range RMSEs for better short-range forecasts members compared

to others. Though this approach needs some refinement, it was possible to demonstrate that such a technique could be useful for the identification of error growth in an ensemble prediction system in general.

Comparison of TIGGE analysis fields points to the importance of the reference used to verify a model or data in general. The case study presented here showed surprisingly large differences in the analyses. These need to be kept in mind when comparing different models. Furthermore it was shown that multi-model EPS approaches lead to an additional value compared to single-model EPS forecasts. The study showed that TIGGE can be a good basis for multi-model forecast studies in general and to produce a multi-model ensemble analysis.

9.4 Outlook

Though the present study has provided an abundance of new and interesting results, some interesting analyses could not be carried out and some new research questions were raised. From a methodological and verification point of view it would have been desirable to use probabilistic scores (e.g. Brier Score, Continuous Ranked Probability Skill Score, ROC curve) to verify the forecast quality of PV streamers. For these method a contingency table is needed, where hits, misses, false alarms and correct negatives are summarised. Therefore all forecasts (and not only the ones with identified PV streamers) should have been looked at, which was impossible, due to the restricted data storage space.

PV streamers are often narrow and finally form distinct vortices, named PV cut-offs. These cut-offs often form cyclones over the Mediterranean Sea and/or Northern Africa, which can cause high-impact weather (e.g. Knippertz and Martin, 2007). A case study or statistical evaluation of the forecast performance in the ECMWF EPS would be an interesting follow-up project.

The case study presented in Chapter 8 was among the first to use the exciting multi-model ensemble capabilities of TIGGE for a detailed predictability case study of a

pronounced upper-level PV streamer and its near-surface impacts. Similar studies in the past investigated forecast performance with respect to upper-level development (Park et al., 2008) and cyclone tracks (Froude, 2010) in a more climatological sense. Some of the analysis techniques presented here, such as multi-model ensemble correlation, could be applied to more PV streamer cases and other phenomena in future work.

For all possible follow-up projects it is important to keep some of the identified limitations in mind. One problem that became evident during this study is the limited availability of vertical levels, meaning that only a crude upper-level PV can be calculated. The PV differences used for forecast evaluation and comparing the TIGGE analyses can be misleading, as low PV values in the troposphere (0-2 PVU) are compared to the high stratospheric values (2-20 PVU) across the tropopause. Some first thoughts of using a rescaled-PV formulation instead are discussed in Martius et al. (2010). The surprisingly large discrepancies between different TIGGE analyses strongly suggest that uncertainties in what we regard as the 'truth' have to be taken into account much more than is currently done. Froude (2010) for example used only ECMWF analysis data in her TIGGE study and speculated that this could bias the results in ECMWF's favour. This is corroborated by the results presented here.

Ensemble forecasting and in particular TIGGE provide a great opportunity to explore the aspects outlined above further in the future. The comprehensive list of variables available in TIGGE makes it possible to investigate dynamical aspects and interaction processes, and pinpoint some of the predictability issues evident in forecasting high-impact weather events.

Blank Page

References

- Abatzoglou, J. T. and G. Magnusdottir, 2004: Nonlinear planetary wave reflection in the troposphere. *Geophysical Research Letters*, **31**, L09101.
- Altenhoff, A. M., O. Martius, M. Croci-Maspoli, C. Schwierz, and H. C. Davies, 2008: Linkage of atmospheric blocks and synoptic-scale Rossby waves: a climatological analysis. *Tellus Series A*, **60**, 1053–1063.
- Appenzeller, C., H. Davies, and W. Norton, 1996: Fragmentation of stratospheric intrusions. *Journal of Geophysical Research-Atmospheres*, **101**(D1), 1435–1456.
- Appenzeller, C. and H. C. Davies, 1992: Structure of stratospheric intrusions into the troposphere. *Nature*, **358**(6387), 570–572.
- Atger, F., 1999: The skill of ensemble prediction systems. *Monthly Weather Review*, **127**(9), 1941–1953.
- Barkan, J., P. Alpert, H. Kutiel, and P. Kishcha, 2005: Synoptics of dust transportation days from Africa toward Italy and central Europe. *Journal of Geophysical Research-Atmospheres*, **110**(D7).
- Barkmeijer, J., R. Buizza, and T. Palmer, 1999: 3D-Var Hessian singular vectors and their potential use in the ECMWF Ensemble Prediction System. *Quarterly Journal of the Royal Meteorological Society*, **125**(558, Part B), 2333–2351.
- Benedict, J. J., S. Lee, and S. B. Feldstein, 2004: Synoptic View of the North Atlantic Oscillation. *Journal of Atmospheric Sciences*, **61**, 121–144.

- Berggren, R., B. Bolin, and R. C.-G., 1949: An aerological study of zonal motion, its perturbations and break-down. *Tellus*, **1**, 14–37.
- Berrisford, P., D. Dee, K. P. Fielding K., Fuentes M., S. Kobayashi, and S. Uppala, 2009: 'The ERA-interim Archive'. *ERA Report Series No. 1*, pp. , ECMWF, Shinfield Park, Reading RG2–9AX, UK.
- Boettcher, M. and H. Wernli, 2011: Life cycle study of a Diabatic Rossby wave as a precursor to rapid cyclogenesis in the North Atlantic - dynamics and forecast performance. *Monthly Weather Review*, **139**, 1861–1878.
- Bougeault, P., Z. Toth, C. Bishop, B. Brown, D. Burridge, D. H. Chen, B. Ebert, M. Fuentes, T. M. Hamill, K. Mylne, J. Nicolau, T. Paccagnella, Y.-Y. Park, D. Parsons, B. Raoult, D. Schuster, P. S. Dias, R. Swinbank, Y. Takeuchi, W. Tennant, L. Wilson, and S. Worley, 2010: The Thorpex Interactive Grand Global Ensemble. *Bulletin of the American Meteorological Society*, **91**(8), 1059–1072.
- Bourke, W., R. Buizza, and M. Naughton, 2004: Performance of the ECMWF and the BoM Ensemble Prediction Systems in the Southern Hemisphere. *Monthly Weather Review*, **132**, 2338–2357.
- Browning, K., 1990: Organization of clouds and precipitation in extratropical cyclones. In: Newton, C.W. and Holopainen, E.O., ed., *Extratropical cyclones - The Erik Palmén Memorial Volumen*, pp. 129–153.
- Buizza, R., J.-R. Bidlot, N. Wedi, M. Fuentes, M. Hamrud, G. Holt, T. Palmer, and F. Vitart, 2006: The ECMWF Variable Resolution Ensemble Prediction Systems (VAREPS). *ECMWF Newsletter No. 108*, pp. ECMWF, Shinfield Park, Reading RG2–9AX, UK.
- Buizza, R., P. Houtekamer, Z. Toth, G. Pellerin, M. Wei, and Y. Zhu, 2005: A comparison of the ECMWF, MSC, and NCEP global ensemble prediction systems. *Monthly Weather Review*, **133**(5), 1076–1097.

- Buizza, R. and T. Palmer, 1995: The singular-vector structure of the atmospheric global circulation. *Journal of the Atmospheric Sciences*, **52**(9), 1434–1456.
- Buizza, R., T. Petrolia, T. Palmer, J. Barkmeijer, M. Hamrud, A. Hollingsworth, A. Simmons, and N. Wedi, 1998: Impact of model resolution and ensemble size on the performance of an Ensemble Prediction System. *Quarterly Journal of the Royal Meteorological Society*, **124**(550, Part B), 1935–1960.
- Carlson, T. N., 1998: *Mid-latitude weather systems*. American Meteorological Society, Boston.
- Chomette, O., M. Legrand, and B. Marticorena, 1999: Determination of the wind speed threshold for the emission of desert dust using satellite remote sensing in the thermal infrared. *Journal of Geophysical Research-Atmospheres*, **104**, 31207–31216.
- Collard, A., F. Hilton, M. Forsythe, and B. Candy, 2011: From Observations to Forecasts - Part 8: The use of satellite observations in numerical weather prediction. *Weather*, **66**(2), 31–36.
- Davies, H. C., C. Schär, and H. Wernli, 1991: The palette of fronts and cyclones within a baroclinic wave development. *Journal of Atmospheric Sciences*, **48**, 1666–1689.
- Dirren, S., M. Didone, and H. C. Davies, 2003: Diagnosis of “forecast-analysis” differences of a weather prediction system. *Geophysical Research Letters*, **30**(26), 2600.
- Eckhardt, S., A. Stohl, H. Wernli, P. James, C. Forster, and N. Spichtinger, 2004: A 15-Year climatology of Warm Conveyor Belts. *Journal of Climate*, **17**, 218–237.
- ECMWF, 2011a: Documentations. Available online at http://www.ecmwf.int/newsevents/training/rcourse_notes/NUMERICAL_METHODS/NUMERICAL_METHODS/Numerical_methods7.html, accessed on 23 July 2011.

- ECMWF, 2011b: Documentations. Available online at http://www.ecmwf.int/products/data/technical/model_id/index.html, accessed on 03 February 2011.
- Federal Office for the Environment, Swiss Confederation, 2010: Hydrological foundations and data from Lago Maggiore-Locarno. Available online at <http://www.hydrodaten.admin.ch/d/2022.htm>, accessed on 20 December 2010.
- Froehlich, L. and P. Knippertz, 2008: Identification and global climatology of upper-level troughs at low latitudes. *Meteorologische Zeitschrift*, **17**(5), 565–573.
- Froude, L. S. R., 2010: TIGGE: Comparison of the prediction of northern hemisphere extratropical cyclones by different Ensemble Prediction Systems. *Weather and Forecasting*, **25**(3), 819–836.
- Froude, L. S. R., L. Bengtsson, and K. I. Hodges, 2007: The prediction of extratropical storm tracks by the ECMWF and NCEP Ensemble Prediction Systems. *Monthly Weather Review*, **135**(7), 2545–2567.
- Gill, A. E., 1982: *Atmosphere-Ocean Dynamics, Volume 30 (International Geophysics)*. Academic Press. ISBN 9780122835223.
- Grams, C. M., H. Wernli, M. Boettcher, J. Campa, U. Corsmeier, S. C. Jones, J. H. Keller, C.-J. Lenz, and L. Wiegand, 2011: The key role of diabatic processes in modifying the upper-tropospheric wave guide: A North Atlantic case study. *Quarterly Journal of the Royal Meteorological Society*, **in press**.
- Hawblitzel, D. P., F. Zhang, Z. Meng, and C. A. Davis, 2007: Probabilistic evaluation of the dynamics and predictability of the mesoscale convective vortex of 10–13 June 2003. *Monthly Weather Review*, **135**(4), 1544–1563.
- Haylock, M. R., N. Hofstra, A. M. G. K. Tank, E. J. Klok, P. D. Jones, and M. New, 2008: A European daily high-resolution gridded data set of surface temperature and precipitation for 1950–2006. *Journal of Geophysical Research-Atmospheres*, **113**(D20).

- Holton, J. R., 2004: *An Introduction to Dynamic Meteorology, Fourth Edition (The International Geophysics Series, Vol 88)*. Academic Press, 4th edition. ISBN 9780123540157.
- Hoskins, B. J. and T. Ambrizzi, 1993: Rossby wave propagation on a realistic longitudinally varying flow. *Journal of the Atmospheric Sciences*, **50**(12), 1661–1671.
- Hoskins, B. J., M. E. McIntyre, and A. W. Robertson, 1985: On the use and significance of isentropic potential vorticity maps. *Quarterly Journal of the Royal Meteorological Society*, **111**(470), 877–946.
- Huffman, G. J., R. F. Adler, D. T. Bolvin, G. Gu, E. J. Nelkin, K. P. Bowman, Y. Hong, E. F. Stocker, and D. B. Wolff, 2007: The TRMM Multisatellite Precipitation Analysis (TMPA): Quasi-global, multiyear, combined-sensor precipitation estimates at fine scales. *Journal of Hydrometeorology*, **8**, 38–55.
- Hurrell, J. W., 1995: Decadal trends in the North Atlantic Oscillation: Regional temperatures and precipitation. *Science*, **269**, 676–679.
- International Federation of Red Cross and Red Crescent Societies, 2008: Information Bulletin, FF-2008-000178-DZA, 05 October 2008. Available online at <http://reliefweb.int/node/282766>, accessed on 15 October 2009.
- Iskenderian, H., 1995: A 10-year climatology of northern-hemisphere tropical cloud plumes and their composite flow patterns. *Journal of Climate*, **8**(6), 1630–1637.
- Jenkner, J., C. Frei, and C. Schwiertz, 2008: Quantile-based short-range QPF evaluation over Switzerland. *Meteorologische Zeitschrift*, **17**, 827–848.
- Johnson, C. and R. Swinbank, 2009: Medium-range multimodel ensemble combination and calibration. *Quarterly Journal of the Royal Meteorological Society*, **135**(640, Part A), 777–794.
- Jones, S. C., P. A. Harr, J. Abraham, L. F. Bosart, P. J. Bowyer, J. L. Evans, D. E. Hanley, B. N. Hanstrum, R. E. Hart, F. Lalaurette, M. R. Sinclair, R. K. Smith, and C. Thorncroft, 2003: The extratropical transition of tropical cyclones:

- Forecast challenges, current understanding, and future directions. *Weather and Forecasting*, **18**, 1052–1092.
- Kalnay, E., 2002: *Atmospheric Modeling, Data Assimilation and Predictability*. Cambridge University Press, 1st edition. ISBN 9780521791793.
- Kiladis, G. N. and K. M. Weickmann, 1992: Extratropical forcing of tropical Pacific convection during winter. *Monthly Weather Review*, **120**(9), 1924–1938.
- Kiladis, G. N. and K. M. Weickmann, 1997: Horizontal structure and seasonality of large-scale circulations associated with submonthly tropical convection. *Monthly Weather Review*, **125**(9), 1997–2013.
- Klein, H., S. Nickovic, W. Haunold, U. Bundke, B. Nillius, M. Ebert, S. Weinbruch, L. Schuetz, Z. Levin, L. A. Barrie, and H. Bingemer, 2010: Saharan dust and ice nuclei over central Europe. *Atmospheric Chemistry & Physics*, **10**, 10211–10221.
- Knippertz, P., 2005: Tropical-extratropical interactions associated with an Atlantic tropical plume and subtropical jet streak. *Monthly Weather Review*, **133**(9), 2759–2776.
- Knippertz, P. and A. H. Fink, 2008: Dry-season precipitation in tropical west africa and its relation to forcing from the extratropics. *Monthly Weather Review*, **136**(9), 3579–3596.
- Knippertz, P. and A. H. Fink, 2009: Prediction of dry-season precipitation in tropical west africa and its relation to forcing from the extratropics. *Weather and Forecasting*, **24**(4), 1064–1084.
- Knippertz, P. and J. E. Martin, 2005: Tropical plumes and precipitation in subtropical and tropical West Africa. *Quarterly Journal of the Royal Meteorological Society*, **131**, 2337–2365.
- Knippertz, P. and J. E. Martin, 2007: The role of dynamic and diabatic processes in the generation of cut-off lows over Northwest Africa. *Meteorology and Atmospheric Physics*, **96**(1-2), 3–19.

- Leutbecher, M. and T. N. Palmer, 2008: Ensemble forecasting. *Journal of Computational Physics*, **227**, 3515–3539.
- Lorenz, E. N., 1963: Deterministic nonperiodic flow. *Journal of the Atmospheric Sciences*, **20**(2), 130–141.
- Lorenz, E. N., 1965: A study of the predictability of a 28-variable atmospheric model. *Tellus*, **17**, 321–333.
- Lynch, A. H. and J. J. Cassano, 2006: *Applied Atmospheric Dynamics*. Wiley. ISBN 9780470861738.
- Marticorena, B. and G. Bergametti, 1995: Modeling the atmospheric dust cycle: 1. Design of a soil-derived dust emission scheme. *Journal of Geophysical Research*, **100**, 16415–16430.
- Martin, J. E., 2006: *Mid-Latitude Atmospheric Dynamics: A First Course*. Wiley. ISBN 9780470864654.
- Martius, O., C. Schwierz, and H. C. Davies, 2008: Far-upstream precursors of heavy precipitation events on the Alpine south-side. *Quarterly Journal of the Royal Meteorological Society*, **134**, 417–428.
- Martius, O., C. Schwierz, and H. C. Davies, 2010: Tropopause-level waveguides. *Journal of Atmospheric Sciences*, **67**, 866–879.
- Martius, O., E. Zenklusen, C. Schwierz, and H. C. Davies, 2006: Episodes of alpine heavy precipitation with an overlying elongated stratospheric intrusion: A climatology. *International Journal of Climatology*, **26**, 1149–1164.
- Massacand, A. C., H. Wernli, and H. C. Davies, 2001: Influence of upstream diabatic heating upon an Alpine event of heavy precipitation. *Monthly Weather Review*, **129**, 2822–2828.
- Matsueda, M., 2009: Blocking predictability in operational medium-range ensemble forecasts. *SOLA*, **5**, 113–116.

- Matsueda, M. and T. Nakazawa, 2011: Daily updated TIGGE forecast products and verifications. Available online at <http://tparc.mri-jma.go.jp/TIGGE/index.html>, accessed on 21 February 2011.
- McGuirk, J. P., A. H. Thompson, and J. R. Schaefer, 1988: An Eastern Pacific tropical plume. *Monthly Weather Review*, **116**(12), 2505–2521.
- McGuirk, J. P., A. H. Thompson, and N. R. Smith, 1987: Moisture bursts over the tropical Pacific-ocean. *Monthly Weather Review*, **115**(4), 787–798.
- McIntyre, M. E. and T. N. Palmer, 1983: Breaking planetary waves in the stratosphere. *Nature*, **305**, 593–600.
- McWilliams, J., 2006: Fundamentals of Geophysical Fluid Dynamics.
- Meteonetwork and ARPA Piemonte, 2008: Analisi dell'evento alluvionale che ha interessato il Piemonte nel maggio 2008. Available online at <http://www.meteo.it/Clima-Statistiche/Analisi-delle28099evento-alluvionale-che-ha-interessato-il-Piemonte-nel-maggio-2008/content/it/1-695-305427-57756>, accessed on 20 December 2010.
- Molteni, F., R. Buizza, T. Palmer, and T. Petroliajgis, 1996: The ECMWF Ensemble Prediction System: Methodology and validation. *Quarterly Journal of the Royal Meteorological Society*, **122**(529, Part A), 73–119.
- NASA, 2009: TRMM data. Available online at <http://daac.gsfc.nasa.gov/data/datapool/TRMM/>, accessed on 21 October 2009.
- NHC, 2010: Tropical Cyclone Reports. Available online at <http://www.nhc.noaa.gov/2008atlan.shtml>, accessed on 09 October 2010.
- NOAA Climate Prediction Center, 2011: Tropical Cyclone Reports. Available online at <http://www.cpc.ncep.noaa.gov/data/teledoc/nao.shtml>, accessed on 21 February 2011.

- Palmer, T., F. Molteni, R. Mureau, R. Buizza, P. Chapelet, and J. Tribbia, 1993: 'Ensemble Prediction' pp. 21-66 in Vol. 1 of Proceedings of the ECMWF seminar on validation of models over Europe, 7-11 September 1992. pp. , ECMWF, Shinfield Park, Reading RG2-9AX, UK.
- Palmer, T. N., 1993: Extended-range atmospheric prediction and the Lorenz model. *Bulletin of the American Meteorological Society*, **74**, 49-66.
- Pappenberger, F., J. Bartholmes, J. Thielen, H. L. Cloke, R. Buizza, and A. de Roo, 2008: New dimensions in early flood warning across the globe using grand-ensemble weather predictions. *Geophysical Research Letters*, **35**(10).
- Park, Y., R. Buizza, and M. Leutbecher, 2008: TIGGE: Preliminary results on comparing and combining ensembles. *Quarterly Journal of the Royal Meteorological Society*, **134**, 2029-2050.
- Parker, D. J. and A. J. Thorpe, 1995: Conditional convective heating in a baroclinic atmosphere: A model of convective frontogenesis. *Journal of Atmospheric Sciences*, **52**, 1699-1711.
- Pelly, J. and B. Hoskins, 2003: How well does the ECMWF Ensemble Prediction System predict blocking? *Quarterly Journal of the Royal Meteorological Society*, **129**(590, Part a), 1683-1702.
- Pelly, J. L. and B. J. Hoskins, 2003: A new perspective on blocking. *Journal of Atmospheric Sciences*, **60**, 743-755.
- Postel, G. and M. Hitchman, 1999: A climatology of Rossby wave breaking along the subtropical tropopause. *Journal of the Atmospheric Sciences*, **56**(3), 359-373.
- Richardson, D., R. Buizza, and R. Hagedorn, 2005: Final report of the 1st Workshop on the THORPEX Interactive Grand Global Ensemble (TIGGE). WMO TD No. 1273, WWRP-THORPEX No. 5 (available from WMO). p. 39pp.
- Rossby, C.-G., 1959: *The atmosphere and sea in motion*, chapter Current problems in meteorology, pp. 9-50. Rockefeller Institute Press, New York.

- Schepanski, K., I. Tegen, B. Laurent, B. Heinold, and A. Macke, 2007: A new Saharan dust source activation frequency map derived from MSG-SEVIRI IR-channels. *Geophysical Research Letter*, **34**, L18803.
- Schwierz, C., M. Croci-Maspoli, and H. C. Davies, 2004a: Perspicacious indicators of atmospheric blocking. *Geophysical Research Letter*, **31**, 6125–6128.
- Schwierz, C., S. Dirren, and H. C. Davies, 2004b: Forced waves on a zonally aligned jet stream. *Journal of Atmospheric Sciences*, **61**, 73–87.
- Schwierz, C., P. Koellner-Heck, E. Z. Mutter, D. N. Bresch, P.-L. Vidale, M. Wild, and C. Schaer, 2010: Modelling European winter wind storm losses in current and future climate. *Climate Change*, **101**(3-4), 485–514.
- Shakina, N. P. and A. R. Ivanova, 2010: The blocking anticyclones: The state of studies and forecasting. *Russian Meteorology and Hydrology*, **35**(11), 721–730.
- Simmons, A. J. and A. Hollingsworth, 2002: Some aspects of the improvement in skill of numerical weather prediction. *Quarterly Journal of the Royal Meteorological Society*, **128**, 647–677.
- Slingo, A., T. P. Ackerman, R. P. Allan, E. I. Kassianov, S. A. McFarlane, G. J. Robinson, J. C. Barnard, M. A. Miller, J. E. Harries, J. E. Russell, and S. Dewitte, 2006: Observations of the impact of a major Saharan dust storm on the atmospheric radiation balance. *Geophysical Research Letters*, **33**(24).
- Slingo, J. M., 1998: Extratropical forcing of tropical convection in a northern winter simulation with the UGAMP GCM. *Quarterly Journal of the Royal Meteorological Society*, **124**(545, Part A), 27–51.
- Sodemann, H., A. S. Palmer, C. Schwierz, M. Schwikowski, and H. Wernli, 2006: The transport history of two Saharan dust events archived in an Alpine ice core. *Atmospheric Chemistry and Physics*, **6**, 667–688.
- Stoelinga, M. T., 1996: A potential vorticity-based study of the role of diabatic heating and friction in a numerically simulated baroclinic cyclone. *Monthly Weather Review*, **124**, 849–874.

- Thorncroft, C. D., B. J. Hoskins, and M. E. McIntyre, 1993: Two paradigms of baroclinic-wave life-cycle behaviour. *Quarterly Journal of the Royal Meteorological Society*, **119**, 17–55.
- Toth, Z., 1992: Quasi-stationary and transient periods in the northern hemisphere circulation series. *Journal of Climate*, **5**, 1235–1248.
- Toth, Z. and E. Kalnay, 1993: Ensemble forecasting at NMC: The generation of perturbations. *Bulletin of the American Meteorological Society*, **74**(12), 2317–2330.
- Tracton, M. S. and E. Kalnay, 1993: Operational ensemble prediction at the national meteorological center - practical aspects. *Weather and Forecasting*, **8**(3), 379–398.
- Uppala, S. M., P. W. Kållberg, A. J. Simmons, U. Andrae, V. D. C. Bechtold, M. Fiorino, J. K. Gibson, J. Haseler, A. Hernandez, G. A. Kelly, X. Li, K. Onogi, S. Saarinen, N. Sokka, R. P. Allan, E. Andersson, K. Arpe, M. A. Balmaseda, A. C. M. Beljaars, L. V. D. Berg, J. Bidlot, N. Bormann, S. Caires, F. Chevallier, A. Dethof, M. Dragosavac, M. Fisher, M. Fuentes, S. Hagemann, E. Hólm, B. J. Hoskins, L. Isaksen, P. A. E. M. Janssen, R. Jenne, A. P. McNally, J.-F. Mahfouf, J.-J. Morcrette, N. A. Rayner, R. W. Saunders, P. Simon, A. Sterl, K. E. Trenberth, A. Untch, D. Vasiljevic, P. Viterbo, and J. Woollen, 2005: The ERA-40 re-analysis. *Quarterly Journal of the Royal Meteorological Society*, **131**, 2961–3012.
- Waugh, D. W. and L. M. Polvani, 2000: Climatology of intrusions into the tropical upper troposphere. *Geophysical Research Letters*, **27**(23), 3857–3860.
- Wei, M. and Z. Toth, 2003: A new measure of ensemble performance: Perturbation versus Error Correlation Analysis (PECA). *Monthly Weather Review*, **131**(8), 1549–1565.
- Wei, M., Z. Toth, R. Wobus, and Y. Zhu, 2008: Initial perturbations based on the ensemble transform (ET) technique in the NCEP global operational forecast system. *Tellus Series A-Dynamic Meteorology and Oceanography*, **60**(1), 62–79.

- Wernli, H., R. Fehlmann, and D. Lüthi, 1998: The effect of barotropic shear on upper-level induced cyclogenesis: Semigeostrophic and primitive equation numerical simulations. *Journal of Atmospheric Sciences*, **55**, 2080–2094.
- Wernli, H. and M. Sprenger, 2007: Identification and ERA-15 climatology of potential vorticity streamers and cutoffs near the extratropical tropopause. *Journal of the Atmospheric Sciences*, **64**(5), 1569–1586.
- Wiegand, L., 2008: Transport of stratospheric airmasses into the tropical troposphere - climatology and influence on the ozone budget, diploma thesis in German. *University of Mainz, Germany*.
- Wiegand, L., A. Twitchett, C. Schwierz, and P. Knippertz, 2011: Heavy precipitation at the Alpine south side and Saharan dust over central Europe: A predictability study using TIGGE. *Weather and Forecasting*, **in press**.
- WMO Report, August 2008: Monthly Climatic Data for the World, August 2008.
- WMO Report, October 2008: Monthly Climatic Data for the World, October 2008.
- WMO Report, September 2008: Monthly Climatic Data for the World, September 2008.
- Ziehmann, C., 2001: Skill prediction of local weather forecasts based on the ECMWF ensemble. *Nonlinear Processes in Geophysics*, **8**, 419–428.

List of Figures

1.1	The evolution of forecast skill at ECMWF from 1981 to the present. The steady improvement with time can at least partly be ascribed to the improved use of satellite data and in particular the closing of the gap between the Northern and Southern Hemisphere as more and more satellite data are used in the otherwise data-sparse southern latitudes. For each day, the top of the coloured band represents the forecast skill in the Northern Hemisphere while the bottom represents the forecast skill in the Southern Hemisphere. Courtesy of ECMWF. Taken from Collard et al. (2011), plot adapted and extended from Simmons and Hollingsworth (2002).	2
1.2	Two fields, of uniform, but different, vorticity ζ_1 and ζ_2 are displayed on an east-west boundary. A perturbation in the vorticity field and the resulting circulation is shown (taken from Holton, 2004).	4
1.3	Vortex stretching and PV conservation. If a material column is stretched to a greater thickness ($h_2 > h_1 > 0$) while conserving its volume, the PV conservation, $PV_2 = PV_1 > 0$ implies an increase in the absolute vorticity, $f(y_2) + \zeta_2 > f(y_1) + \zeta_1 > 0$ (taken from McWilliams, 2006)	5
1.4	Schematic of two types of Rossby wave breaking with a) an LC1-type life cycle and b) an LC2-type life cycle. The dashed line marks the approximate position of the mean jet stream at each stage (taken from Thorncroft et al., 1993).	6

- 1.5 Occurrence frequency [%] of PV intrusions into low latitudes 200 hPa zonal wind (contours) in boreal winter (October - March). Data: ECMWF Re-Analysis40 from 1980 to 2001 (taken from Froehlich and Knippertz, 2008, (slightly modified)). 7
- 1.6 Meteosat IR satellite images with superimposed isotachs at the 345 K isentropic level in yellow (ms^{-1}) and streamlines in blue at 00 UTC 10 January 2002 (taken from Knippertz and Martin, 2005). 8
- 1.7 Schematic of ensemble prediction, with individual trajectories drawn for forecasts starting from a representative set of perturbed initial conditions within a circle representing their uncertainty and ending within a range of possible solutions, represented by the ellipse. For the shorter range, the forecasts are close to each other and they may be considered deterministic, but beyond a certain time, the forecast is stochastic. Forecasts may cluster into groups of similar trajectories (denoted A and B), whose probability may be related to the number of forecasts in each group (taken from Tracton and Kalnay, 1993). 10
- 3.1 Comparison of two upper-level PV fields calculated in different ways from model analysis data for the same date. Left: Calculation of PV at every model level, interpolation to 200 and 500 hPa and averaging both fields. Right: Calculation of PV with potential temperature and relative vorticity at 200 and 500 hPa using Equation 3.4. 27
- 3.2 Comparison of two similar upper level PV fields calculated on different grid resolutions. Left: 1° by 1° , right: 2.5° by 2.5° 28
- 3.3 Schematic depiction of the streamer identification. The black line depicts a PV contour. The shaded area account for the identified streamer if the spherical distance d (line with arrows) between two points is smaller than the threshold D and l (black solid line) is larger then the threshold value L (taken from Wernli and Sprenger, 2007). 29

- 3.4 Winter mean (DJF) frequency in % (gray shading) of PV streamers on a) 320 K for the ERA-15 time period of 1979-1993 (taken from Wernli and Sprenger, 2007), b) 200/500 hPa-PV for the ERA-40 time period 1980-2001 and c) 200/500 hPa-PV for the operational analysis in the time period of available ensemble data 1996-2008. 29
- 3.5 Example PV streamer episode from 1200 UTC 18 (a) to 0000 UTC 20 February 1998 (d). Black lines: Identified PV streamer contours, green rectangle: PV streamer need to occur within this area (0° - 27.5° N, 30° W - 30° E) during the episode, black rectangle: verification area (0° - 40° N, 40° W - 40° E) for investigations in Chapter 5, explained in Section 3.4. 31
- 3.6 Three example of PV streamer verification dates. Coloured boxes are defined with different algorithms. For further investigations the blue rectangle is used (for details see text). 33
- 4.1 Synoptic situation on 12 September 2008: a) Upper-level PV in colours with black lines showing mean sea-level pressure. A green contour encircles the detected PV streamer. b) Precipitation amounts from ENSEMBLES E-OBS gridded rain gauge data over Europe (restricted to land) from 0600 UTC 12 to 0600 UTC 13 September 2008. c) TRMM satellite rain product over Northern Africa in mm from 0600 UTC 12 to 0600 UTC 13 September 2008. 37
- 4.2 Influence of Hurricane *Ike* on the upper-level evolution at 00 UTC a) 09, b) 12, c) 16 and d) 18 September 2008. Colours indicate the upper level potential vorticity in PVU units. Black contours show the mean sea-level pressure fields and green dashed contours mark the detected PV streamers. 39
- 4.3 Precipitation amounts from TRMM satellite rain product over Northern Africa on a) 17, b) 18, c) 19 and d) 21 September 2008. 40

- 5.1 Number of PV streamers per year identified in ECMWF operational analysis data. Identification of the PV streamers described in detail in Chapter 3. 44
- 5.2 Number of PV streamers per month identified in ECMWF operational analysis data. Identification of the PV streamers described in detail in Chapter 3. 44
- 5.3 Number of PV Streamers per longitude in 5° steps from 40°W - 40°E as identified in ECMWF operational analysis data. Identification of the PV streamers described in detail in Chapter 3. Dashed lines are the divide of the five longitudinal zones, see details in text. 45
- 5.4 Time series of PV Streamers for every January (J), February (F), March (M), April (A), November (N) and December (D) from 1997 to 2008. Colours depict the different longitude sections defined in Section 5.1 from Figure 5.3: yellow = 40°W - 20°W, red = 20°W - 5°E, green = 5°E - 15°E, blue = 15°E - 25°E, black = 25°E - 40°E. The monthly mean NAO index is shown as black line. 47
- 5.5 Comparison of RMSE (solid line) and spread (dashed line) for the 1- to 10-day ECMWF ensemble forecasts. RMSE and spread were averaged over 75 PV streamer cases and calculated for the PV in a box 40°N - 0°S, 40°W - 40°E (red lines in a and b), PV restricted to the PV streamer area within the box (black line in a) and geopotential height at 500 hPa in the whole box (blue line in b). 50
- 5.6 Comparison of RMSE (bars) and spread (yellow lines) for the 1- to 10-day ECMWF ensemble forecasts separated into yearly sections. Numbers of PV streamers per year are given in the legend. RMSE and spread were averaged over all PV streamer cases per year and calculated for PV in the box 40°N - 0°S, 40°W - 40°E. 51
- 5.7 Same as Figure 5.6. Separated into temporal sections based on EPS changes in time (details: see Table 2.1). 53

- 5.8 Comparison of RMSE (solid line) and spread (dashed line) for the 1- to 10- day ECMWF ensemble forecasts separated in longitudinal sections (details in Section 5.1). Number of PV streamers per section are given in the legend. RMSE and spread were averaged over all PV streamer cases and calculated for PV in the box $40^{\circ}\text{N} - 0^{\circ}\text{S}$, $40^{\circ}\text{W} - 40^{\circ}\text{E}$ 54
- 5.9 Difference between forecast (a) 72h and b) 168h) and analysed PV. PV values are a box average and all 75 PV streamer forecasts are included (see text for details). 55
- 5.10 Difference between box averaged PV of displaced forecast and steady spatially analysed PV for 75 PV streamer events. The figures show the results for the a) 24 h, b) 96 h, c) 144 h and d) 216 h forecasts. . . 57
- 6.1 Correlation coefficients (in colours) between different atmospheric variables in the ensemble prediction system. Every grid point of (i) geopotential height at 200 hPa (top panel), (ii) equivalent potential temperature at 850 hPa (middle panel) and (iii) vertical wind at 700 hPa (bottom panel) is correlated with upper tropospheric PV averaged in a box (red box in right panels). The PV from 168 h forecast is correlated with atmospheric fields from 48 h (left panel) to 168 h (right panel) (details described in text). Black lines are the 1.5 PVU ECMWF analysis from 0000 UTC 26 November 2005 (left) to 0000 UTC 01 December 2005 (right). 62
- 6.2 Comparison of equivalent potential temperature at 850 hPa (left) and upper-tropospheric PV (right) for selected 96 h EPS member THE850 forecasts (c and e), 168 h EPS member PV forecasts (d and f) and ECMWF operational analysis at the respective dates (a and b). 64

- 6.3 Mean over all 75 PV streamer episodes correlation coefficients (in colours). All fields are shifted with the result that the PV streamer verification boxes have their longitude centre at 0°E (technical details see text). Every grid point of (i) upper-tropospheric PV (top panel), (ii) equivalent potential temperature at 850 hPa (middle panel) and (iii) vertical wind at 700 hPa (bottom panel) is correlated with upper-tropospheric PV averaged in the verification box (12.5°W - 12.5°E and 25°N - 40°N). The PV from 168 h forecast is correlated with atmospheric fields from 96 h (left panel) to 168 h (right panel) forecasts (details described in text). 67
- 6.4 Track of Tropical Cyclone *Nicole* from 00 UTC 24 November to 12 UTC 02 December 1998 (extracted from NHC Preliminary Report - Hurricane Nicole, accessed on <http://www.nhc.noaa.gov/1998nicole.html>, 15 February 2011). 71
- 6.5 Track of Tropical Cyclone *Olga* from 00 UTC 24 November to 12 UTC 04 December 2001 (extracted from NHC Tropical Cyclone Report - Hurricane Olga, accessed on <http://www.nhc.noaa.gov/2001olga.html>, 15 February 2011). 72
- 6.6 Correlation coefficients (in colours) between equivalent potential temperature at 850 hPa (THE850) and upper tropospheric PV averaged in a box (red box in Figure 6.6d). The PV from 168 h forecast is correlated with THE850 fields from a) 96 h, b) 120 h, c) 144 h and d) 168 h forecasts (details described in section 6.1). Black lines are the 1.5 PVU and 2.0 PVU ECMWF analysis from a) 1200 UTC 28 November 2001 to d) 1200 UTC 01 December 2001. The black spiral symbols mark the hurricane position. 73

- 7.1 Hovmoller diagram of the meridional wind component at 300 hPa averaged between 30°N and 60°N from 1200 UTC 27 December 1998 (day: -9) to 1200 UTC 10 January 1999 (day: +5). The dashed line marks the PV streamer position and the red dot the PV streamer position at verification time. 77
- 7.2 RMSEs (forecast minus ECMWF operational analysis) of single EPS member forecasts (lines) within a east-west shifted box (details see text) for two example PV streamer cases, a) analysis time 10 January 1998 and b) 19 November 1999. Line colours are defined by rank of RMSE at lead time 48 h (details see text). 78
- 7.3 Histogram of occurrence frequencies of ranks of EPS member RMSEs for long lead times (120-168 h). Split in EPS members with the five lowest RMSEs at 48 h (a) and EPS members with the five highest RMSEs at 48 h (b). Low rank numbers stand for low RMSE and consequently high ranks for high RMSEs. 79
- 8.1 Synoptic development between 21 and 26 May 2008 as represented by PV (colours) and mean sea-level pressure (contours every 4 hPa) from ECMWF analysis fields. a) 1200 UTC 21 May 2008, b) 1200 UTC 23 May 2008, c) 1200 UTC 24 May 2008 and d) 1200 UTC 26 May 2008. The black rectangle in d) shows the area used for the investigation of the forecast performance. 85

- 8.2 High-impact weather caused by the PV streamer: a) ECMWF analysis of wind at 925 hPa for 1200 UTC 26 May 2008. The black rectangle shows the target area used for the investigation of the forecast performance of dust mobilization over the Sahara. b) Dust uplift over the Sahara represented by the SEVIRI dust product (see Section 2.4.2 for more information) at 2000 UTC 26 May 2008. Dust stands out as purple areas over the desert within the black ellipses. The dark reddish areas to the north are clouds ahead of the upper-level PV streamer. c) Observations of accumulated four-day precipitation from 0600 UTC 26 May 2008 to 0600 UTC 30 May 2008. The black rectangle shows the target area used for the investigation of the precipitation forecast performance. 86
- 8.3 Forecast ensemble-mean 1.5 PVU contours of PV for seven lead times (see legend) and four TIGGE centres: a) BoM, b) ECMWF, c) JMA and d) NCEP. Forecasts are valid at 1200 UTC 26 May 2008 (see Figure 8.1d for comparison). 88
- 8.4 RMSE of ensemble-mean PV averaged over the target area (29°N-55°N, 15°W-2°E; see Figure 8.1d) for each TIGGE centre. Forecasts are valid at 1200 UTC 26 May 2008 and have lead times between 24 h and 168 h. RMSEs are calculated with respect to a) ECMWF analyses and b) each centre's own analysis. 89
- 8.5 Difference between UKMO and ECMWF PV analysis fields at 1200 UTC 26 May 2008. Positive values indicate larger UKMO PV. The dotted black line defines the 1.5 PVU contour line from the ECMWF analysis and the solid green line the 1.5 PVU line of UKMO. 90

- 8.6 RMSE as in Figure 8.4b (solid lines) together with the corresponding ensemble SPREAD (standard deviation, dashed lines) for a) non-dispersive, b) under-dispersive, c) inconclusive (details see Section 8.4.1) behaviour of TIGGE models. d) Difference of RMSE and SPREAD accumulated over all lead times for each TIGGE centre. Forecasts are valid at 1200 UTC 26 May 2008 and have lead times between 24 h and 168 h. 91
- 8.7 Position error (in 1000 km) of the PV streamer ensemble forecasts based on PV (see Section 8.2 for definition) from nine TIGGE forecast centres (indicated in each panel). Ellipses surround position forecasts from all members for 1200 UTC 26 May 2008 (see Figure 8.1d). Gray shading indicates lead time ranging from 24 h to 168 h (see legend). Centre of the coordinate system is the PV streamer position as analysed by ECMWF in all panels. 94
- 8.8 Potential dust uplift ($10^3 m^3 s^{-3}$ PDU, see Section 8.5.1 for definition) averaged over the box 23°N-35°N, 5°W-10°E from each TIGGE centre and the multi-model ensemble including all TIGGE members. a) 24 h, b) 96 h, c) 120 h and d) 168 h forecast for 1200 UTC 26 May 2008. The dashed grey lines indicate the PDU analysis from each TIGGE centre. Box-and-whisker plots are defined with the upper and lower border of the grey box as the 1st and 3rd quartile, the black line within the box is the median, the whiskers on both sides are the minimum and maximum and the blank circles are outliers. The notches on the boxes indicate that the medians of two box plots are significantly different when notches do not overlap. 96

- 8.9 Correlation coefficients (grey shading) between the predicted PDU in a box over the Sahara (black rectangle) and predicted PV at every grid point, both valid at 1200 UTC 26 May. a) all lead time forecasts (24-168 h) from NCEP, b) 48 h forecast from NCEP, c) all lead time forecasts from ECMWF and d) 72 h forecast from ECMWF. Black lines are the ensemble mean 1.5 PVU contour line from the respective centre at the respective lead time(s). 100
- 8.10 Same as Figure 8.9 but for 72 h forecasts from all TIGGE members. 101
- 8.11 Predicted precipitation in mm accumulated over the four-day period 0600 UTC 26 to 0600 UTC 30 May 2008 and averaged over the target box (43.5°-46.5°N and 2.5°-9.5°E) from each TIGGE centre and the multi-model ensemble except for KMA (details see Section 8.5.3). Lead times are a) 24 h, b) 48 h, c) 96 h and d) 168 h. The dashed line is the observed value from ENSEMBLES E-OBS. Box-and-whisker plots are defined as in Figure 8.8 102
- 8.12 Correlation coefficients (grey shading) between the predicted four-day accumulation of precipitation valid from 0600 UTC 26 May to 0600 UTC 30 May in a box over the Alpine south side (black rectangle) and predicted PV at every grid point valid at 1200 UTC 26 May for a) all lead time forecasts (24-168 h) from BoM and b) the 120 h forecasts from all TIGGE members. Black lines are the ensemble-mean 1.5 PVU contour lines over a) all lead times and b) all TIGGE members. 105
- A.1 Difference between box averaged PV of displaced forecast and steady spatially analysed PV for two PV streamers between 40°W - 20°W. The figures show the results for the a) 24 h and b) 192 h forecasts. . 146
- A.2 Difference between box averaged PV of displaced forecast and steady spatially analysed PV for 14 PV streamers between 20°W - 5°E. The figures show the results for the a) 24 h and b) 120 h forecasts. 146

- A.3 Difference between box averaged PV of displaced forecast and steady spatially analysed PV for 17 PV streamers between 5°E-15°E. The figures show the results for the a) 72 h and b) 144 h forecasts. 146
- A.4 Difference between box averaged PV of displaced forecast and steady spatially analysed PV for 22 PV streamers between 15°W-25°W. The figures show the results for the a) 144 h and b) 216 h forecasts. 147
- A.5 Difference between box averaged PV of displaced forecast and steady spatially analysed PV for 20 PV streamers between 25°W-40°W. The figures show the results for the a) 24 h and b) 168 h forecasts. . 147
- A.6 Mean over two PV streamer episodes correlation coefficients (in colours). PV streamer happened between 40°W and 20°W (defined in section 5.1). Every grid point of (i) upper-tropospheric PV (top panel) and (ii) equivalent potential temperature at 850 hPa (bottom panel) is correlated with upper tropospheric PV averaged in a box around each PV streamer. The PV from 168 h forecast is correlated with atmospheric fields from 120 h (left panel) to 168 h (right panel) forecasts (details described in section 6.1). 148
- A.7 Mean over 14 PV streamer episodes correlation coefficients (in colours). PV streamer happened between 20°W and 5°E (defined in section 5.1). Every grid point of (i) upper-tropospheric PV (top panel) and (ii) equivalent potential temperature at 850 hPa (bottom panel) is correlated with upper tropospheric PV averaged in a box around each PV streamer. The PV from 168 h forecast is correlated with atmospheric fields from 72 h (left panel) to 168 h (right panel) forecasts (details described in section 6.1). 149

- A.8 Mean over 17 PV streamer episodes correlation coefficients (in colours).
 PV streamer happened between 5°E and 15°E (defined in section 5.1). Every grid point of (i) upper-tropospheric PV (top panel) and (ii) equivalent potential temperature at 850 hPa (bottom panel) is correlated with upper tropospheric PV averaged in a box around each PV streamer. The PV from 168 h forecast is correlated with atmospheric fields from 120 h (left panel) to 168 h (right panel) forecasts (details described in section 6.1). 150
- A.9 Mean over 22 PV streamer episodes correlation coefficients (in colours).
 PV streamer happened between 15°E and 25°E (defined in section 5.1). Every grid point of (i) upper-tropospheric PV (top panel), (ii) equivalent potential temperature at 850 hPa (middle panel) and (iii) vertical wind at 700 hPa (bottom panel) is correlated with upper tropospheric PV averaged in a box around each PV streamer. The PV from 168 h forecast is correlated with atmospheric fields from 120 h (left panel) to 168 h (right panel) forecasts (details described in section 6.1). 150
- A.10 Mean over 20 PV streamer episodes correlation coefficients (in colours).
 PV streamer happened between 25°E and 40°E (defined in section 5.1). Every grid point of (i) upper-tropospheric PV (top panel), (ii) equivalent potential temperature at 850 hPa (middle panel) and (iii) vertical wind at 700 hPa (bottom panel) is correlated with upper tropospheric PV averaged in a box around each PV streamer. The PV from 168 h forecast is correlated with atmospheric fields from 120 h (left panel) to 168 h (right panel) forecasts (details described in section 6.1). 151
- A.11 Standard deviation of ensemble-mean PV within the target area (29°N-55°N, 15°W-2°E; see Figure 8.1d in Chapter 8) for each TIGGE centre. Forecasts are valid at 1200 UTC 26 May 2008 and have lead times between 24 h and 168 h. 152

- A.12 168 h ECMWF EPS member forecasts of upper-level PV. EPS members are chosen by their amount of potential dust uplift (PDU, numbers in each panel in m^3s^{-3} , see Section 8.5.1 for definition) averaged over the box 23°N-35°N, 5°W-10°E. Top panel shows the EPS member with lowest PDU forecast, middle panel the EPS member PDU forecast nearest at the analysis and the bottom panel the member forecast predicting the largest amount of PDU. 153
- A.13 168 h NCEP EPS member forecasts of upper-level PV. EPS members are chosen by their amount of potential dust uplift (PDU, numbers in each panel in m^3s^{-3} , see Section 8.5.1 for definition) averaged over the box 23°N-35°N, 5°W-10°E. Top panel shows the EPS member with lowest PDU forecast and the bottom panel the member forecast predicting the largest amount of PDU. 154
- A.14 144 h ECMWF EPS member forecasts of upper-level PV. EPS members are chosen by their amount of predicted precipitation (number in each panel in mm) accumulated over the four-day period 0600 UTC 26 0600 UTC 30 May 2008 and averaged over the target box (43.5°-46.5°N and 2.5°-9.5°E) at the Alpine south side. Top panel shows the EPS member with lowest precipitation forecast, middle panel the EPS member precipitation forecast nearest at the observation and the bottom panel the member forecast predicting the highest amount of rain. 155

Blank Page

List of Tables

- 2.1 Changes in the Ensemble Prediction System at the ECMWF from the implementation in 1992 to 2007. The abbreviations used in the table are as follows: SV: singular vector; NH: Northern Hemisphere; SH: Southern Hemisphere; TR: Tropics; Tx: spectral triangular truncation at total wavenumber x ; and TLx: spectral triangular truncation at total wavenumber x with linear reduced Gaussian grid; HRes: Horizontal Resolution; VRes: Vertical Resolution; #: Number of EPS members including the control forecast; Stochastic Physics; d: days; h: hours. 16
- 2.2 Characteristics of the nine EPSs participation in TIGGE in May 2008. The abbreviations used in the table are as follows: SV: singular vector; BV: bred vector; ET: ensemble transform; EnKF: ensemble Kalman filter; ETKF: ensemble transform Kalman filter; EOF: empirical orthogonal function; NH: Northern Hemisphere; SH: Southern Hemisphere; TR: tropics; GenSI: generalised multivariate statistical interpolation; 3-/4DVar: 3-/4-dimensional variational data assimilation; GSI: gridded statistical interpolation; Tx: spectral triangular truncation at total wavenumber x ; and TLx: spectral triangular truncation at total wavenumber x with linear reduced Gaussian grid. Abbreviations of the centres' names are found in the text. 19
- 8.1 Number of EPS members that do not match the analysed PV streamer. For details of the method, see Section 8.2. 84

Blank Page

Appendix A

Supplementary Figures

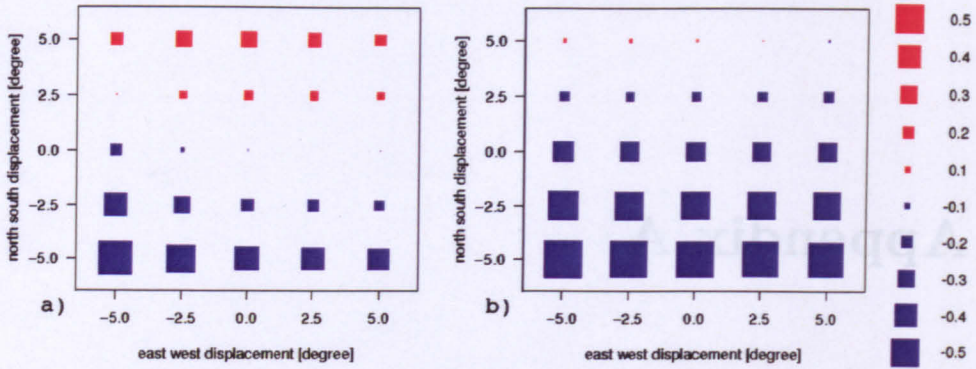


Figure A.1: Difference between box averaged PV of displaced forecast and steady spatially analysed PV for two PV streamers between 40°W - 20°W. The figures show the results for the a) 24 h and b) 192 h forecasts.

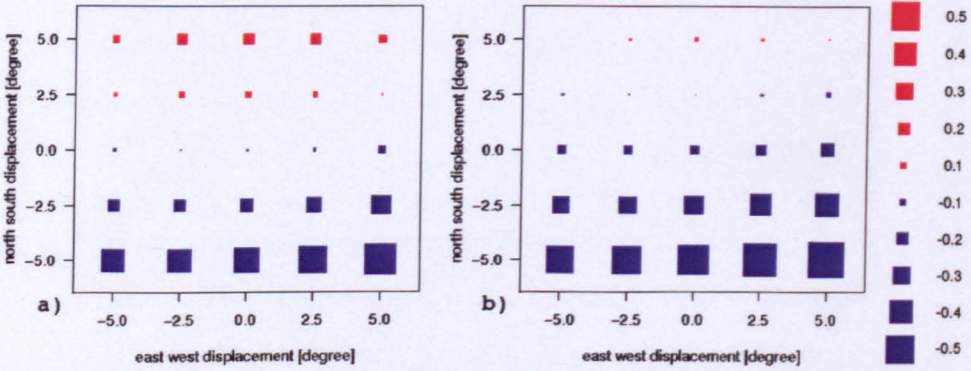


Figure A.2: Difference between box averaged PV of displaced forecast and steady spatially analysed PV for 14 PV streamers between 20°W - 5°E. The figures show the results for the a) 24 h and b) 120 h forecasts.

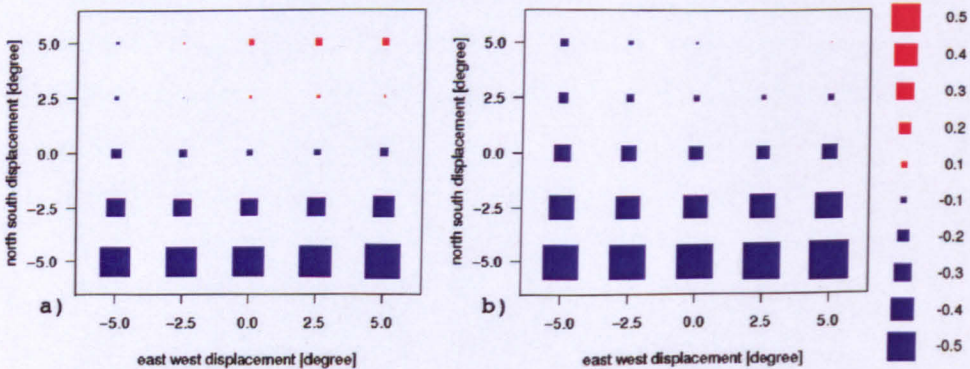


Figure A.3: Difference between box averaged PV of displaced forecast and steady spatially analysed PV for 17 PV streamers between 5°E - 15°E. The figures show the results for the a) 72 h and b) 144 h forecasts.

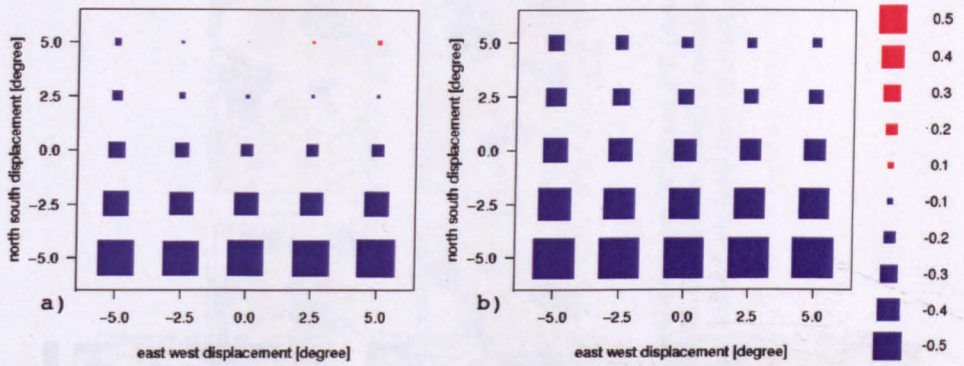


Figure A.4: Difference between box averaged PV of displaced forecast and steady spatially analysed PV for 22 PV streamers between $15^{\circ}\text{W} - 25^{\circ}\text{W}$. The figures show the results for the a) 144 h and b) 216 h forecasts.

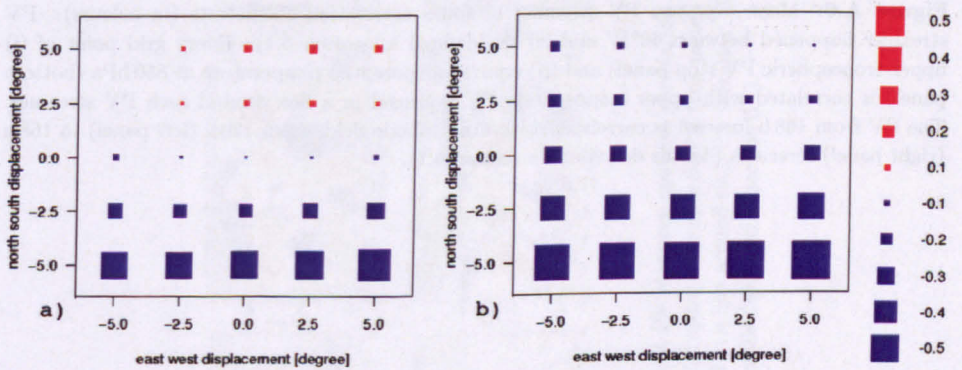


Figure A.5: Difference between box averaged PV of displaced forecast and steady spatially analysed PV for 20 PV streamers between $25^{\circ}\text{W} - 40^{\circ}\text{W}$. The figures show the results for the a) 24 h and b) 168 h forecasts.

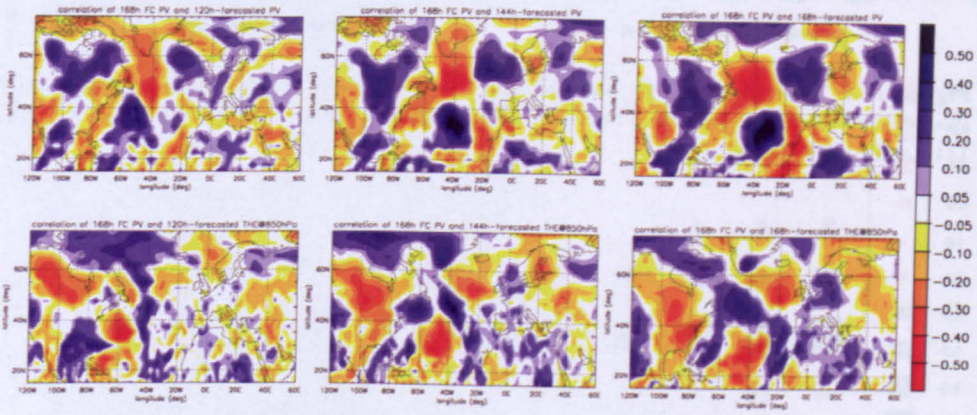


Figure A.6: Mean over two PV streamer episodes correlation coefficients (in colours). PV streamer happened between 40°W and 20°W (defined in section 5.1). Every grid point of (i) upper-tropospheric PV (top panel) and (ii) equivalent potential temperature at 850 hPa (bottom panel) is correlated with upper tropospheric PV averaged in a box around each PV streamer. The PV from 168 h forecast is correlated with atmospheric fields from 120 h (left panel) to 168 h (right panel) forecasts (details described in section 6.1).

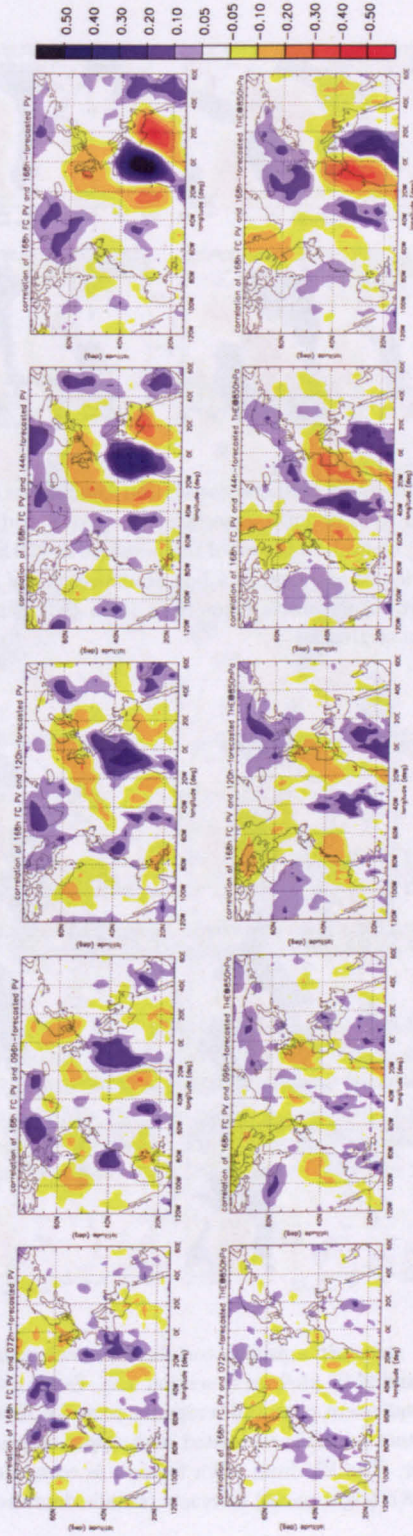


Figure A.7: Mean over 14 PV streamer episodes correlation coefficients (in colours). PV streamer happened between 20°W and 5°E (defined in section 5.1). Every grid point of (i) upper-tropospheric PV (top panel) and (ii) equivalent potential temperature at 850 hPa (bottom panel) is correlated with upper tropospheric PV averaged in a box around each PV streamer. The PV from 168 h forecast is correlated with atmospheric fields from 72 h (left panel) to 168 h (right panel) forecasts (details described in section 6.1).

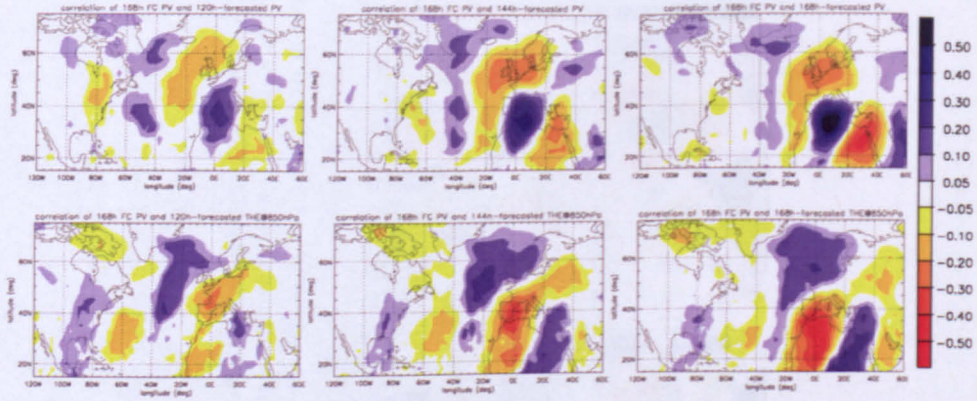


Figure A.8: Mean over 17 PV streamer episodes correlation coefficients (in colours). PV streamer happened between 5°E and 15°E (defined in section 5.1). Every grid point of (i) upper-tropospheric PV (top panel) and (ii) equivalent potential temperature at 850 hPa (bottom panel) is correlated with upper tropospheric PV averaged in a box around each PV streamer. The PV from 168 h forecast is correlated with atmospheric fields from 120 h (left panel) to 168 h (right panel) forecasts (details described in section 6.1).

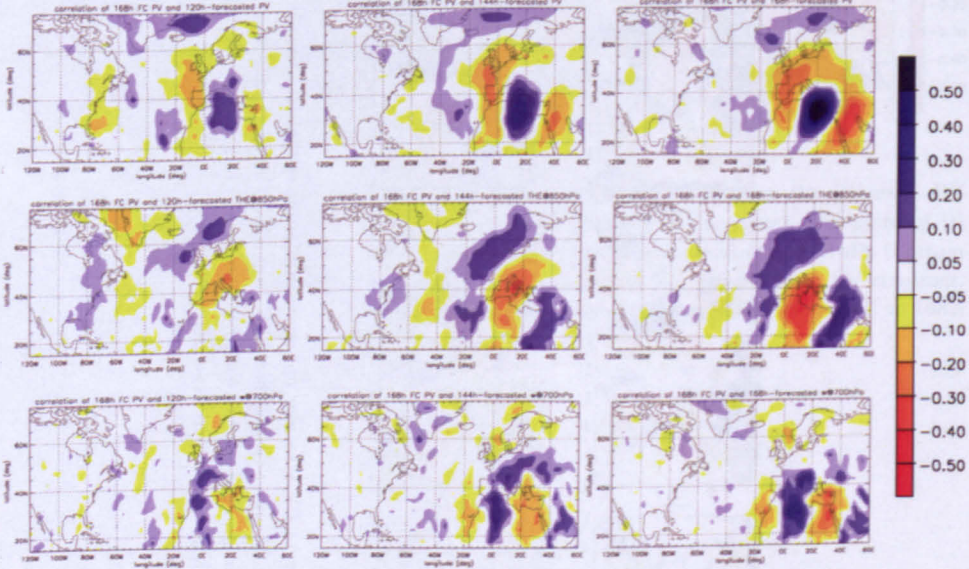


Figure A.9: Mean over 22 PV streamer episodes correlation coefficients (in colours). PV streamer happened between 15°E and 25°E (defined in section 5.1). Every grid point of (i) upper-tropospheric PV (top panel), (ii) equivalent potential temperature at 850 hPa (middle panel) and (iii) vertical wind at 700 hPa (bottom panel) is correlated with upper tropospheric PV averaged in a box around each PV streamer. The PV from 168 h forecast is correlated with atmospheric fields from 120 h (left panel) to 168 h (right panel) forecasts (details described in section 6.1).

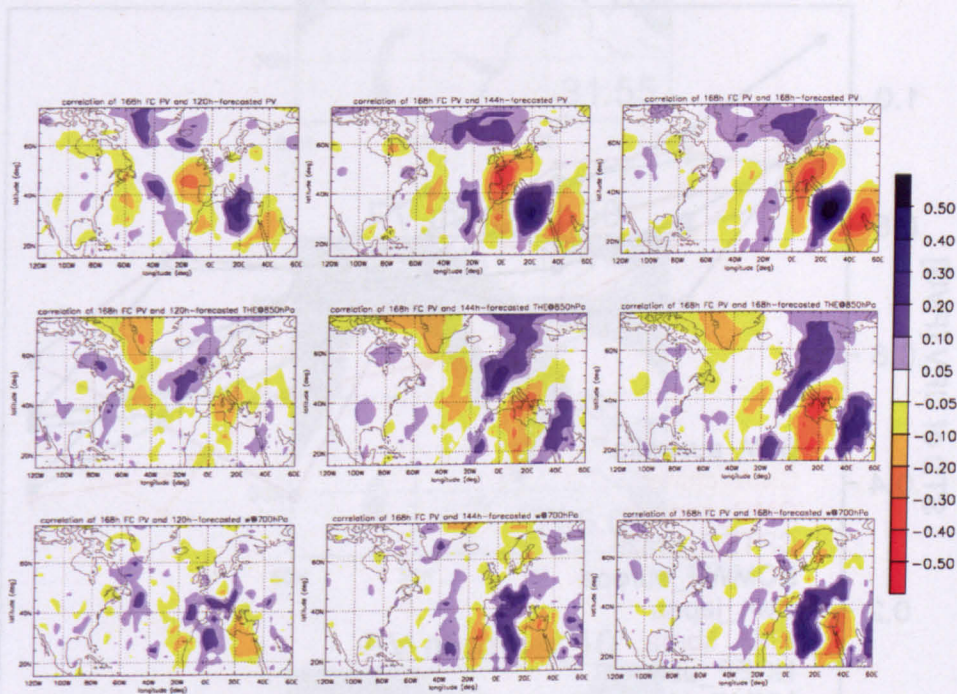


Figure A.10: Mean over 20 PV streamer episodes correlation coefficients (in colours). PV streamer happened between 25°E and 40°E (defined in section 5.1). Every grid point of (i) upper-tropospheric PV (top panel), (ii) equivalent potential temperature at 850 hPa (middle panel) and (iii) vertical wind at 700 hPa (bottom panel) is correlated with upper tropospheric PV averaged in a box around each PV streamer. The PV from 168 h forecast is correlated with atmospheric fields from 120 h (left panel) to 168 h (right panel) forecasts (details described in section 6.1).

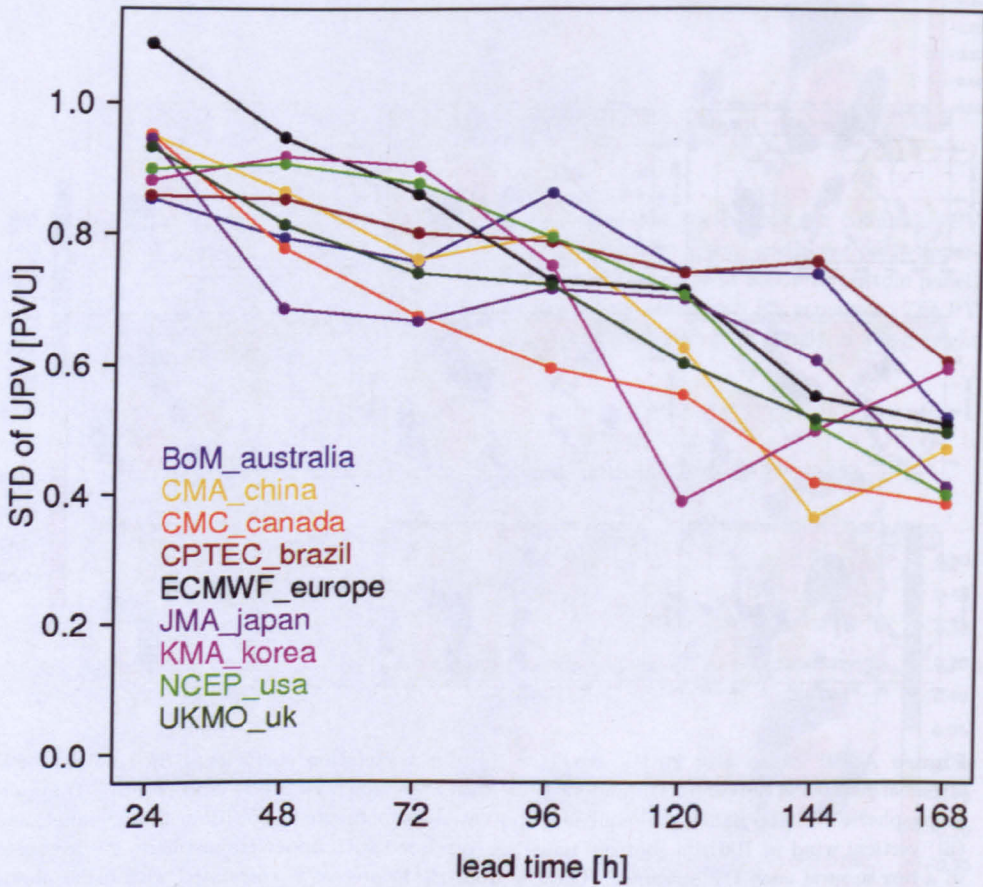


Figure A.11: Standard deviation of ensemble-mean PV within the target area (29°N - 55°N , 15°W - 2°E ; see Figure 8.1d in Chapter 8) for each TIGGE centre. Forecasts are valid at 1200 UTC 26 May 2008 and have lead times between 24 h and 168 h.

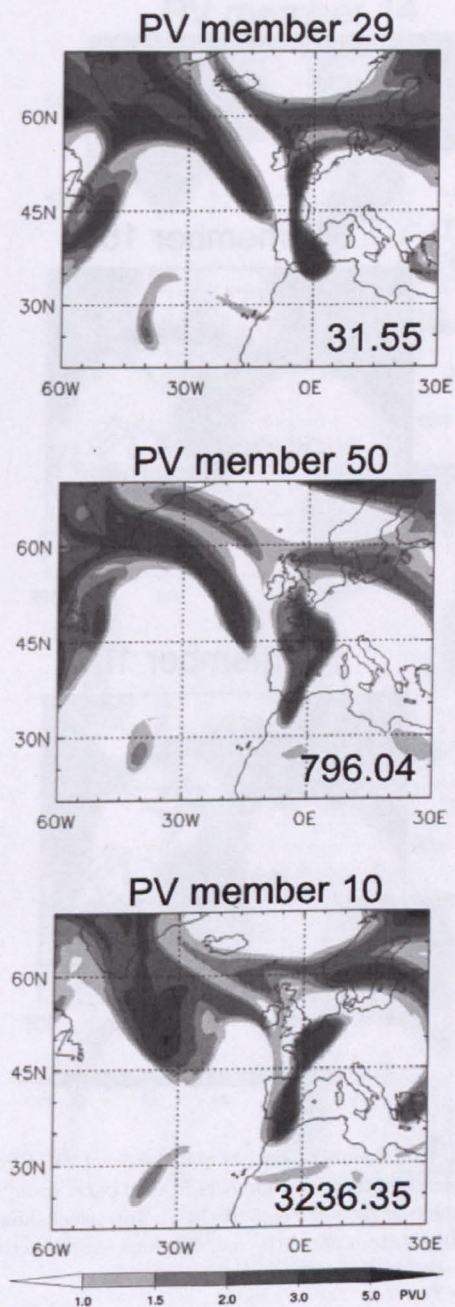


Figure A.12: 168 h ECMWF EPS member forecasts of upper-level PV. EPS members are chosen by their amount of potential dust uplift (PDU, numbers in each panel in $m^3 s^{-3}$, see Section 8.5.1 for definition) averaged over the box $23^\circ N$ - $35^\circ N$, $5^\circ W$ - $10^\circ E$. Top panel shows the EPS member with lowest PDU forecast, middle panel the EPS member PDU forecast nearest at the analysis and the bottom panel the member forecast predicting the largest amount of PDU.

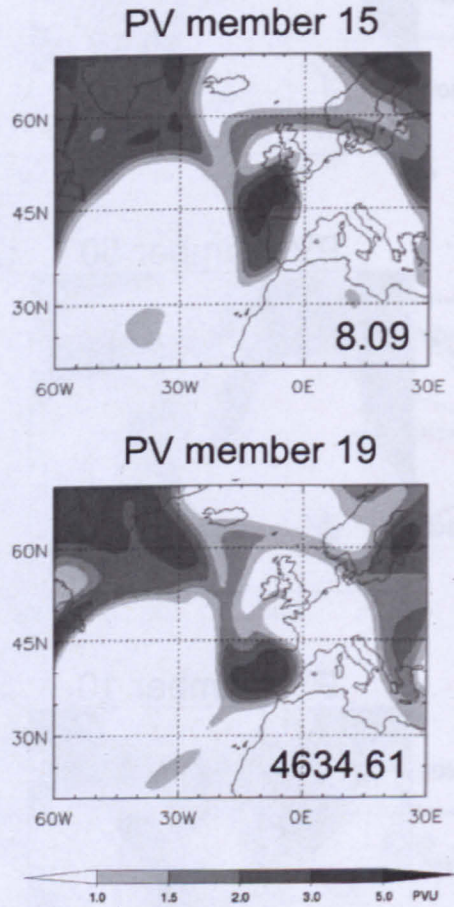


Figure A.13: 168 h NCEP EPS member forecasts of upper-level PV. EPS members are chosen by their amount of potential dust uplift (PDU, numbers in each panel in m^3s^{-3} , see Section 8.5.1 for definition) averaged over the box $23^\circ N$ - $35^\circ N$, $5^\circ W$ - $10^\circ E$. Top panel shows the EPS member with lowest PDU forecast and the bottom panel the member forecast predicting the largest amount of PDU.

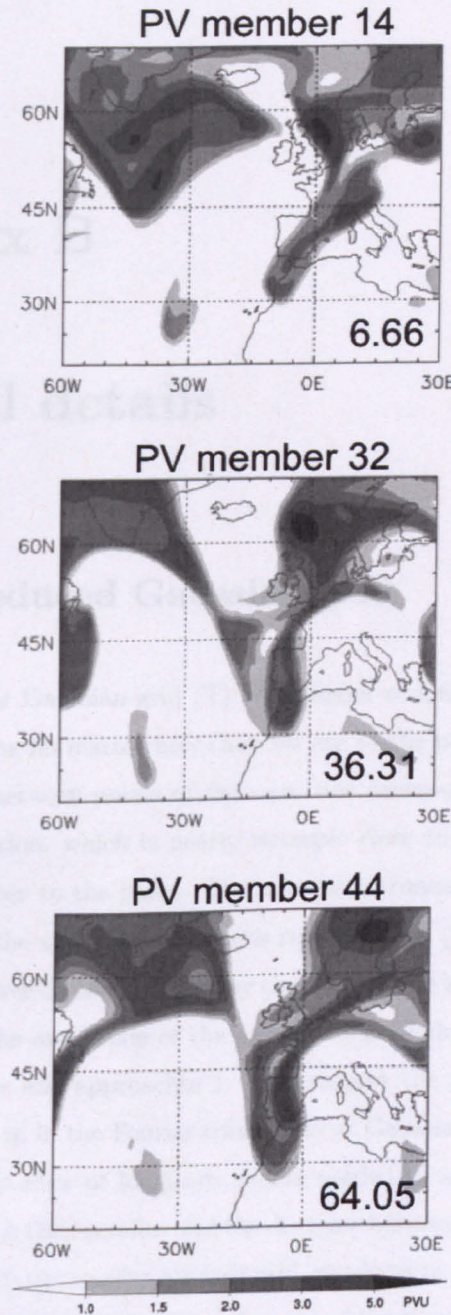


Figure A.14: 144 h ECMWF EPS member forecasts of upper-level PV. EPS members are chosen by their amount of predicted precipitation (number in each panel in mm) accumulated over the four-day period 0600 UTC 26–0600 UTC 30 May 2008 and averaged over the target box (43.5° – 46.5° N and 2.5° – 9.5° E) at the Alpine south side. Top panel shows the EPS member with lowest precipitation forecast, middle panel the EPS member precipitation forecast nearest at the observation and the bottom panel the member forecast predicting the highest amount of rain.

Blank Page

Appendix B

Technical details

Details on reduced Gaussian grid

When using a regular Gaussian grid (T) the number of longitude points per row of latitude is the same no matter how close we are to the pole. Therefore the geographical distance between points of the same row decreases as we approach the poles and the resolution, which is nearly isotropic close to the equator becomes highly anisotropic close to the poles. The triangular truncation in spectral space is isotropic because the shortest wavelength representable (wavenumber $n=M$) is independent of the wave direction (given by the value of the zonal wavenumber m). On the other hand the amplitude of the associated Legendre polynomials is very small when m is large and approaches 1. This suggests the possibility of ignoring some of the values of m in the Fourier transforms at Gaussian latitudes approaching the poles. The number of longitude points needed to represent properly the retained wavelengths is then smaller and the distance between points decreases less dramatically than with the regular (or full) grid, resulting in a more isotropic resolution. The Gaussian grid resulting from these considerations is called the reduced Gaussian grid TL. (ECMWF, 2011a)